Phase-Field Modelling of Crack Propagation

by

Zhuo Li

A THESIS SUBMITTED IN PARTIAL FULFILLMENT OF
THE REQUIREMENTS FOR THE DEGREE OF

MASTER OF APPLIED SCIENCE

in

The Faculty of Graduate and Postdoctoral Studies

(Materials Engineering)

THE UNIVERSITY OF BRITISH COLUMBIA

(Vancouver)

June 2021

© Zhuo Li 2021

The following individuals certify that they have read, and recommend to the Faculty of Graduate and Postdoctoral Studies for acceptance, the thesis entitled:

Phase-Field Modelling of Crack Propagation

submitted by **Zhuo Li** in partial fulfillment of the requirements for the degree of **Master of Applied Science** in **Materials Engineering**.

Examining Committee:

Matthias Militzer, Professor, Materials Engineering Department, UBC
Supervisor

Warren J. Poole, Professor, Materials Engineering Department, UBC
Supervisory Committee Member

Chadwick Sinclair, Professor, Materials Engineering Department, UBC
Supervisory Committee Member

Abstract

Brittle fracture has been investigated for more than a century. Various models managed to capture the fracture phenomena, among which the phase-field models gained popularity in the mechanics and the physics community in the past two decades. However, due to distinct backgrounds, detailed comparisons between the phase-field models in the two communities are missing. Therefore, to understand the strengths and limitations of these models, this study aims to compare them in the same settings. Quasi-static and dynamic brittle fractures are investigated in the current work, of which the main difference is the loading speed.

Since numerous phase-field models have been developed in both communities, in the present work, only the most representative models are selected, i.e., Miehe et al.'s model [1] and the Karma-Kessler-Levine (KKL) model [2]. Through comparisons with the Griffith theory [3], in quasi-static simulations, the unphysical dependence of the energy release rate on the load in the KKL model was observed. Meanwhile, in dynamic fracture, both models showed good agreement with the theories by Eshelby [4] and Adda-Bedia [5] in some aspects while deviations in others.

The results suggest that for quasi-static fracture, Miehe et al.'s model is a reasonable option. While for dynamic fracture, comparisons with experiments are necessary to evaluate the accuracy of the models.

Lay Summary

A seemingly unimportant crack can lead to disasters like airplane crashes, pipeline explosions, etc. Millions of dollars are lost each year because of structural failures. Fracture mechanics, as a subject dealing with crack evolution is, therefore, extremely important in engineering designs. However, after several decades of development, there are still challenges in understanding fracture mechanisms. As a reliable and inexpensive alternative for experiments, computational modelling quickly becomes an indispensable part of fracture mechanics. In recent years, phase-field models stood out among fracture models and gained popularity in the mechanics and the physics community. In detail, both communities use different formulations of these models to capture fracture phenomena, but the comparison between them is missing in the literature. Therefore, the present work aims to compare these models so that researchers who are new to the field can decide which model to use.

Preface

The purpose of the Master's thesis is to have detailed comparisons between two popular phase-field fracture models by the mechanics and the physics community. The thesis was written to fulfill the graduation requirements of the Master of Applied Science Program at the Department of Materials Engineering, The University of British Columbia, Point Grey campus. I was responsible for developing the computer programs, implementing the simulations, analyzing the data, and writing the thesis.

The research question was brought out by my supervisor, Prof. Matthias Militzer, who also provided assistance and guidance throughout every stage of the research. This thesis is written by the author with discussions and editing assistance from Prof. Matthias Militzer.

In Chapter 2, Figures 2.7 and 2.9 have been taken with permission from the cited resources.

Table of Contents

Appendices

List of Tables

List of Figures

List of Symbols

Latin Letters

A	Cross-sectional area of an elastic band
a	Crack extension length
$\mathbb{C}$	Stiffness tensor
C	Young's modulus in 1D and shear modulus in 2D
C_r	Rayleigh wave speed
C_s	Shear wave speed
d	Interpolation function for the energy related to strain hardening
dx	Mesh size
dt	Time step size
E	Young's modulus
$E_{surface}$	Surface energy
$E_{elastic}$	Elastic energy
E'	Parameter that is related to Young's modulus and Poisson's ratio
E_{in}	Elastic energy input in the system
$\mathcal{E}_c$	Critical elastic energy density to break the material
$\mathcal{F}$	Free energy functional
$f_{interfacial}$	Density functional of the interfacial energy
$f_{elastic}$	Density functional of the elastic energy
$f_{plastic}$	Density functional of the energy related to strain hardening
$f_{dissipation}$	Density functional of the dissipated energy because of plasticity
G	Energy release rate
G^M	Energy release rate in the mechanical model
G^K	Energy release rate in the KKL model
G_c	Critical energy release rate
G_c^M	Critical energy release rate in the mechanical model
G_c^K	Critical energy release rate in the KKL model

$G^{1.5}$	Energy release rate when $E_{in} = 1.5G_c$.
$G^{2.0}$	Energy release rate when $E_{in} = 2.0G_c$.
$G_c^{1.5}$	Critical energy release rate when $E_{in} = 1.5G_c$.
$G_c^{2.0}$	Critical energy release rate when $E_{in} = 2.0G_c$.
G_c^{bulk}	Critical energy release rate in the bulk
G_c^{int}	Critical energy release rate in the grain boundary
G_c^{d}	Critical energy release rate in dynamic fracture
G_θ	Energy release rate as a function of kinking angle θ
g	Degradation function
h	Geometrical function
K	Stress intensity factor
K_c	Fracture toughness
K_I	Stress intensity factor for mode I fracture
K_{II}	Stress intensity factor for mode II fracture
K_{III}	Stress intensity factor for mode III fracture
L	Length of an elastic band
L_x	Length of the 2D sheet
L_y	Width of the 2D sheet
l	Internal length scale
l_c	Initial crack length
M	Mobility
m	Factor in the double-well function
n	Normal vector
p	Interpolation function for the dissipated energy because of plasticity
r	Distance from the crack tip
r_{tip}	Crack tip radius
S	Strain-energy density factor
t	Time
U	Elastic energy
u	Displacement field
V	Double-well function
x	Position

Greek Letters

Γ_l	Numerical crack surface area
Δ	Boundary displacement
δ	Crack interface thickness
ε	Strain tensor
ε_c	Critical strain for crack initiation
η	Residual stiffness
θ	Kinking angle
κ	Coefficient before the gradient term in the KKL model
κ_{curv}	Crack tip curvature
λ	Branching angle
μ	Shear modulus
ν	Poisson's ratio
ρ	Material density
σ	Stress tensor
$\sigma_{i,j}$	Stress at (i, j) in the polar coordinate system
$\sigma_{tensile}$	Tensile stress
σ_c	Failure stress
ϕ	Phase-field parameter
ϕ_{front}	Definition of the crack front position
φ_{int}	Grain boundary angle

List of Abbreviations

BCL	Battelle Columbus Laboratories
FDM	Finite difference method
GDP	Gross national product
KKL	Karma-Kessler-Levin
LEFM	Linear elastic fracture mechanics
MD	Molecular dynamics

Acknowledgements

I cannot begin to express my gratitude to my supervisor Prof. Matthias Militzer for giving me this exciting project and providing me the encouragement and guidance throughout the project. I would also like to extend my sincere thanks to Dr. Michael Greenwood from CanmetMATERIALS for his constructive advice and invaluable discussions. I am always grateful to have such a group of supportive co-workers in the microstructure group. Dr. Hocine Lebed never wavered in his support whenever I have problems in the research. Ayush Suhane and Hariharan Umashankar are always willing to have discussions with me to clear my doubts. I am also thankful to Tianbi Zhang who taught me to use the departmental cluster, MICRESS, Thermo-calc, and kindly provided me the template for this thesis. Special thanks to Sabyasachi Roy who gave me valuable suggestions about thesis writing.

Finally, I am deeply indebted to my parents for their love and support.

Chapter 1

Introduction

According to a 1983 report by the Battelle Columbus Laboratories (BCL) [6], the annual cost related to fracture in the US is $119 billion, which is about 4% of the GDP (gross national product). A tremendous amount of money is spent each year on safety inspection, maintenance, repair, and replacement of the structures. Apart from the economic impact, fracture also leads to numerous catastrophes, e.g., the breakage of the liberty ships in the North Atlantic, the crashes of the first commercial jet airliner (de Havilland Comet), the failure of the Aloha Airlines Flight 243, etc, which result in the loss of human lives. These events of failure happen due to various reasons, e.g., overloading, defects in materials, lack of maintenance, deficiencies in structural design, and environmental effects. Thanks to the efforts of engineers and researchers, people nowadays have a much deeper understanding of fracture mechanisms, which enables safer designs with fewer failures. Meanwhile, fracture mechanics becomes one of the most important subjects in mechanics with billions of dollars put into research each year [6]. However, there are still challenges in fracture mechanics, which require collaboration between researchers in multiple fields, i.e., physics, mechanics, and materials.

Understanding the fracture mechanism has always been a challenge as different materials often exhibit distinct fracture phenomena. Depending on whether the material goes through plastic deformation, fracture can be categorized into brittle fracture with little or no plastic deformation and ductile fracture with plastic deformation. Brittle fracture is often observed in ceramics. Meanwhile, ductile fracture can be found in most metals. Compared with ductile fracture, brittle fracture is relatively well-understood, although the crack nucleation in brittle fracture is still a challenging topic. The existing theories can predict some important fracture phenomena, e.g., critical condition for propagation, crack path, and velocity. However, these theories often utilize assumptions that may not be applicable in reality. Moreover, the simplified settings adopted in theories lead to difficulty in predicting fracture phenomena in practice, as the settings are normally more complex. As a result, computational modelling as an alternative way to study fractures has gained popularity in recent years. Since some

of the computational models are based on theories, they are the perfect tools to verify theories and understand the fracture mechanisms. Besides, the flexibility of applying the models to arbitrary settings enables comparisons with experiments and the predictions of fracture phenomena.

The phase-field model as a popular model for simulating phase transformation has been applied to solve fracture problems for two decades in both the mechanics and the physics community. In both communities, the phase-field models were successfully applied to brittle fracture and showed some promising results. Since these models appear to be similar with only slight differences in formulations, it would be interesting to know the differences between them. However, there have not been any detailed comparisons between these models in the literature. Therefore, the main objective of the work is to compare phase-field fracture models in the mechanics and the physics community to understand their strengths and limitations, so that researchers who are new to the field can have a better idea of which model to use.

This thesis is organized as follows: Chapter 2 provides a literature review, in which the basics of the fracture theories and some fracture models are briefly covered, along with a detailed review of the phase-field fracture models in the mechanics and the physics community. Chapter 3 presents the scope and the objectives of the work. In Chapter 4, the methodology including the equations and simulation settings is given. To derive the proper ranges of the model parameters, sensitivity analyses are presented in Chapter 5. Chapters 6 and 7 focus on the model applications, in which the results are compared with fracture theories. In Chapter 8, a summary and an outlook into future work are presented.

Chapter 2

Literature Review

2.1 Introduction

In this chapter, some relevant fracture theories and models are reviewed. The first part of the chapter introduces the fracture theories for both quasi-static and dynamic fracture. Then, some of the popular fracture models are briefly overviewed. The latter part of the chapter is dedicated to an extensive review of the phase-field fracture models in two communities: the mechanics and the physics community. Although the chapter focuses on brittle fracture, phase-field fracture models with plasticity are also reviewed as pure brittle fracture is hardly seen in engineering materials.

2.2 Crack Propagation in Quasi-static Brittle Fracture

Crack propagation is a complex phenomenon that exhibits distinct patterns under different loading conditions. In general, the loading direction can be arbitrary and induces complex stress states in the body, i.e., tensile and compressive stress and in-plane and out-of-plane shear stress, which are difficult to analyze. Therefore, to simplify the analysis, fracture is normally identified by three modes depending on the loading direction:

- Mode I or the opening mode where the load is normal to the crack plane (Figure 2.1a).
- Mode II or the sliding mode where the load is parallel to the crack plane and normal to the crack front (Figure 2.1b).
- Mode III or the tearing mode where the load is parallel to the crack plane and the crack front (Figure 2.1c).

From the definitions of fracture mode, it is obvious that fracture is a 3D problem. However, because of the complexity in 3D stress analysis, most fracture theories and simulations are based on simplified 2D scenarios with some assumptions. Among these assumptions, three of them are most popular:

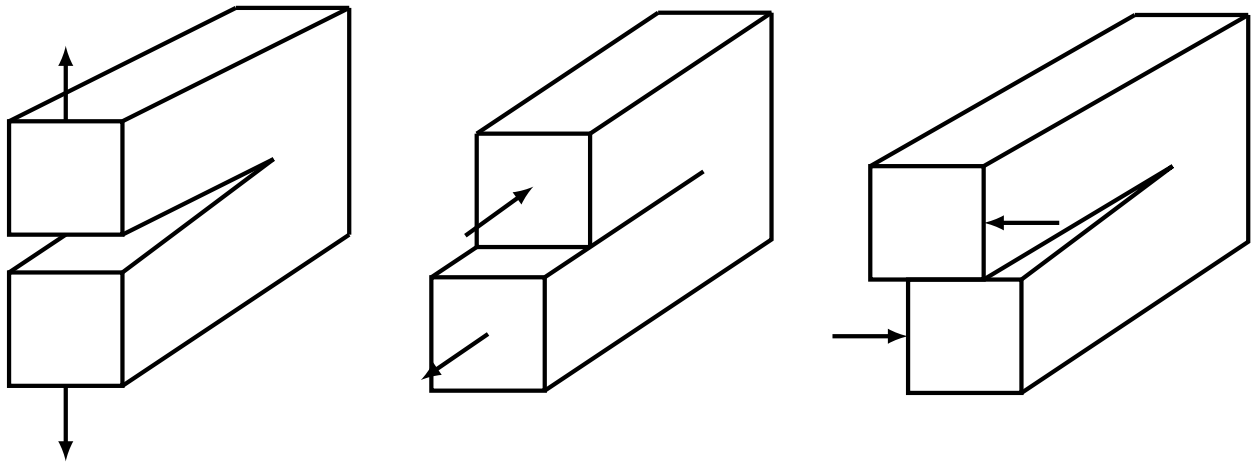

Figure 2.1: Schematics of three fracture modes: (a) mode I, (b) mode II and (c) mode III. The black arrow indicates the loading direction.

- Plane strain condition where the plate is thick such that the strain is assumed to be zero in the thickness direction.
- Plane stress condition where the plate is thin such that the stress is assumed to be zero in the thickness direction.
- Antiplane shear condition where only the displacement in the thickness direction is non-zero and does not vary within the thickness direction.

Although distinct from other conditions, the antiplane shear condition is rarely observed in reality, it was originally designed and widely used to study the 2D mode III fracture in theories.

Apart from the loading direction, fracture can also be categorized based on the loading speed, i.e., quasi-static and dynamic fracture. In quasi-static fracture, the loading rate is extremely slow such that the stress is assumed to be in equilibrium. Meanwhile, the crack front moves slowly, and the velocity is assumed to be zero. When the actual loading rate and crack velocity are zero instead of being close to zero as in the quasi-static case, it becomes the static fracture. Although these two types of fracture are different in experiments, they are treated the same way in theories and simulations, as they are all governed by the mechanical equilibrium equation. Therefore, quasi-static and static fractures are not distinguished in this thesis. In dynamic fracture, however, stress waves are utilized to characterize the rapid loading, and the inertia effect due to the fast crack movement is taken into consideration [7].

The fundamental theories for quasi-static brittle fracture can be dated back to the seminal studies by Griffith [3] and Irwin [8], which are considered as the foundations of the linear elastic fracture mechanics (LEFM). Griffith assumed that the elastic energy release balances the surface energy increment at the crack tip. To identify the amount of elastic energy release per unit area of the newly created crack surface, the energy release rate (G) was introduced and is given as [3]:

$$G = -\frac{\partial U}{\partial a} \tag{2.1}$$

where U is the elastic energy, and a is the crack surface area which is the crack length in 2D. The unit of G is J/m^2. When G is larger than the critical value (G_c) known as the critical energy release rate, the crack will propagate. To enable more thorough investigations into brittle fracture, Irwin derived the asymptotic stress solution near the crack tip. In the polar coordinate, the near-tip stress reads [9]:

$$\sigma_{ij} = \frac{K}{\sqrt{2\pi r}} f_{ij}(\theta) \tag{2.2}$$

where σ_{ij} is the stress, K is the stress intensity factor, r is the distance from the crack tip, $f_{ij}(\theta)$ is a dimensionless quantity related to the load and geometry. The unit of K is $Pa\sqrt{m}$. Based on the stress solution, Irwin suggested that the crack propagates when K reaches the critical value (K_c) known as the fracture toughness. Although the Griffith theory is an energetic approach, while the stress intensity factor is related to the near-tip stress field, they are equivalent. The relation of G and K in 2D is given by [9]:

$$G = \frac{K_I^2}{E'} + \frac{K_{II}^2}{E'} + \frac{K_{III}^2}{2\mu} \tag{2.3}$$

with:

$$E' = \begin{cases} E & \text{plane stress} \\ \frac{E}{1-\nu^2} & \text{plane strain} \end{cases} \tag{2.4}$$

where K_I, K_{II} and K_{III} are the stress intensity factors in three fracture modes, E' is related to Young's modulus (E) and Poisson's ratio (ν), and μ is the shear modulus.

Both the Griffith theory and Irwin's formulations are powerful tools in terms of predicting the start of crack propagation. However, they are unable to describe the crack path. Therefore, many theories [10–12] were developed to predict the crack propagation direction by extending either the Griffith theory or Irwin's formulations. These criteria can be divided into two categories: the local criterion [10, 11] in which the propagation is determined by

the crack tip fields, and the global criterion [12] which is based on the energy balance of the system.

As for the local criterion, either the stress or elastic energy field at the crack tip region is evaluated. By comparing the stress at the crack tip, Erdogan and Sih [10] introduced the maximum tensile stress criterion in which they stated that the crack propagates into the direction normal to the maximum tensile stress. Due to its simplicity, this criterion was widely used in the mechanics community [13–15]. In numerical applications, the tensile stress is evaluated along a circle centred at the crack tip with a radius r (Figure 2.2) [16]. Since the accuracy of the kinking angle depends on the number of points along the circle, this method is sensitive to the mesh size at the crack tip. Besides, to deal with the stress singularity at the crack tip, great efforts have been made in the past few decades to develop numerical tools, e.g., the re-meshing technique [15], the extended finite element method [13, 14], etc.

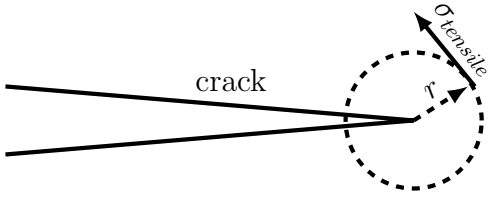

Figure 2.2: The schematic description of the maximum tensile stress criterion. The solid arrow indicates the direction of the maximum tensile stress ($\sigma_{tensile}$) along the circle. The dashed arrow indicates the crack propagation direction which is perpendicular to the direction of the maximum tensile stress.

Arguing that the maximum tensile stress criterion becomes invalid when $r = 0$, as the singular stresses cannot be compared, Sih and Macdonald [11] introduced the minimum strain energy density criterion. They defined a term called the strain-energy density factor (S), which is the elastic energy density multiplied by the distance to the crack tip (r). Since the stress has $1/\sqrt{r}$ singularity (Equation (2.2)) and the energy density has $1/r$ singularity, by multiplying the energy density with r, S does not have a singularity even at the crack tip. Then they claimed that the crack should propagate in the direction with the minimum strain energy density factor. However, since the criterion is implemented in the same way as the maximum tensile stress criterion and the stress singularity still exists, it also requires using complicated numerical methods.

The mesh dependency is the main problem in the models utilizing the local criteria. The maximum strain energy release rate criterion as a global approach, however, does not have

such a problem. With this criterion, the crack is supposed to propagate in the direction with the maximum strain energy release rate. Simple as it may seem, the numerical implementation is complicated. The most straightforward approach is the real crack extension method [13]. In this method, the crack is manually extended into different directions with small distances, after which the energy release rates in those directions are evaluated. Although this method is easy to implement, it suffers from low computational efficiency as the mechanical equations are calculated many times in different directions for each small crack extension [16]. To address this problem, several methods have been developed, e.g., the virtual crack extension method and the G_θ method. In the virtual crack extension method [17–19], the analytical solutions for the energy release rate in different directions are approximated with the finite element method. Therefore, instead of numerically solving the mechanical equations in all directions, the direction with the maximum energy release rate can be determined from the analytical solutions. Similarly, in the G_θ method [20], the energy release rate is formulated as a function of the kinking angle (θ) with certain assumptions, and θ is derived by minimizing the function G_θ. Although these methods are much more efficient, they are conceptually more complicated than the real crack extension method. Besides, the analytical relations between the energy release rate and the kinking angle may not be accurate.

2.3 Basic Phenomena in Dynamic Brittle Fracture

Distinct from quasi-static fracture, the crack velocity is an important feature in dynamic fracture. The first calculation of the crack velocity based on continuum mechanics was given by Freund [21] who studied the propagation of a semi-infinite crack in an infinitely large domain. The result suggested that the limiting velocity for dynamic crack propagation is the Rayleigh wave speed (C_r). However, various experiments showed that the limiting velocity is around $0.5C_r$, and the value depends on the materials and the loading condition [7]. The discrepancy in the limiting velocity may come from the straight crack path assumption made in Freund's analysis, as the crack branching can be observed in dynamic fracture in many materials. Therefore, one possible reason for the low limiting velocity observed in the experiments is the breakdown of Freund's theory. However, even today, a satisfying explanation for the branching behaviour is still lacking.

Yoffe [22] was the first to perform the continuum mechanics analysis on the branching phenomenon. In the study, Yoffe analyzed the stress distribution of a crack translating with a constant velocity in an infinitely large medium and adopted the maximum tensile stress

criterion. From the analytical solution, it was observed that when the crack speed reaches $0.6C_r$, the rearrangement of the stress at the crack front leads to the crack bifurcation with the branching angle equal to 60°. Eshelby [4] then argued that since the surface energy doubles after crack bifurcation, to maintain the total energy of the system, the speed after branching should decrease. Thus, Eshelby assumed that the velocity is zero after branching. Then, from the energy balance between the energy flux into the crack tip and the surface energy, the critical branching velocity was found to be around $0.6C_r$ in the limiting case, where the branching angle is zero. However, Eshelby's result was considered as a rough estimate as no solution was provided for arbitrary branching angles [5]. By adopting Eshelby's approach, Adda-Bedia [5] then studied the bifurcation of a semi-infinite crack in an infinitely long strip under the antiplane shear condition. The branching angle and critical branching velocity were shown to be 79.2° and $0.39C_s$, where C_s is the shear wave speed.

The branching angle and velocity by Adda-Bedia [5] agree qualitatively well with experiments. However, Ravi-Chandar [7] argued that the crack speed after branching does not decrease significantly from experimental observations, which suggests that the zero-velocity assumption by Adda-Bedia and Eshelby is inappropriate. From the micrographs of the crack fronts, Ravi-Chandar suggested that the crack branching is a result of the interaction of microcracks in a small zone ahead of the crack tip (process zone), which cannot be explained properly from the continuum mechanics scale. Since the LEFM is the foundation of the theories and models in this project, the continuum mechanics theories are the focuses of the current work. A detailed explanation of other possible branching mechanisms can be found in [7]. Although understanding the branching mechanism remains a challenge, experimental and simulation investigations will continuously help unveil the mystery behind it.

2.4 Brief Overview of the Fracture Models

Experiments play a critical role in understanding fracture mechanisms. However, the dynamics of the fracture process is challenging to investigate experimentally, since the crack propagates very fast, i.e., several thousands of meters per second [23]. Therefore, theories and models are required to have a thorough understanding of the fracture mechanisms. Since the macrocrack originates from the coalescence of microcracks, or the separation of atoms at an even smaller scale, the atomic-scale models that can deal with the motion of atoms seem to be ideal to study the mechanisms. Molecular dynamics (MD), as one of the most popular atomistic models, utilizes Newton's equations of motion to describe the motion of atoms and

has successfully been used to reproduce many fracture phenomena, e.g., interaction of the crack with dislocation, atom configuration, void, etc. Even though with the cheaper and more powerful computational resources nowadays, MD simulations can deal with systems of up to several million atoms, they are still too small to have enough complexity in the structure [23].

Therefore, atomistic models have to be coupled with models in larger scales, i.e., mesoscale ($100nm$ to $100\mu m$) and macroscale ($> 0.5mm$). Depending on the treatment of the crack interface, these models can be divided into two categories: sharp-interface model where the properties, e.g., mass, density, etc, go through an abrupt transition at the crack interface (Figure 2.3a) and diffuse-interface model where the properties vary smoothly at the interface (Figure 2.3b). Most of the sharp-interface models rely on various propagation criteria discussed in Section 2.2. Because of the stress singularity at the crack tip, they suffer from the mesh sensitivity issue. As for the diffuse-interface models, the smooth interface removes the singularity at the crack tip. As a result, they are relatively insensitive to the mesh size. Although the diffuse-interface crack description and the non-singular crack tip stress deviate from the LEFM, the diffuse-interface models have great advantages in capturing complex crack patterns, especially in 3D.

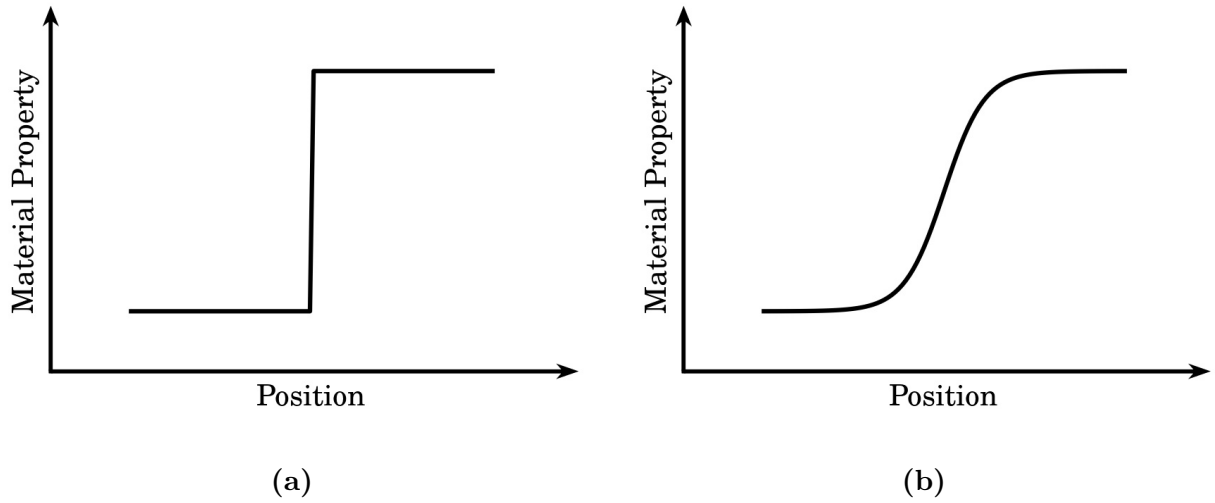

Figure 2.3: Schematic profiles for (a) the sharp-interface model and (b) the diffuse-interface model.

Among the diffuse-interface models, the phase-field fracture models have gained popularity in both the mechanics and the physics community over the past two decades. The phase-field model was originally designed to describe solidification. The first successful ap-

plication of the phase-field concept was made by Kobayashi [24] who studied dendrite growth in solidification. The ability to reproduce the complex morphology of dendrites with simple formulations and low computational cost, then made the phase-field model emerge to be a popular computational tool to solve problems in different fields, i.e., solidification [24–27], recrystallization [28–30], solid-state phase transition [31–34], crack propagation [2, 35–37], etc.

The beauty of the phase-field model lies within its simple and elegant formulations. In the model, a phase-field variable (ϕ) is related to physical properties, e.g., density, concentration, grain, phase, etc, which vary smoothly at the interface. Then, the interface migration is governed by the partial differential equations referred to as the phase-field equations. For non-conserved variables, e.g., grain, phase, etc, the phase-field equation is described by the Allen-Cahn equation as [38]:

$$\frac{\partial \phi}{\partial t} = -M \frac{\delta \mathcal{F}}{\delta \phi} \tag{2.5}$$

where M is the mobility related to the interface migration speed, and $\mathcal{F}$ is the free energy functional which contains the interfacial energy, bulk free energy, elastic energy, etc. As for the conserved variables, e.g., concentration, density, etc, the phase-field equation is described by the Cahn-Hilliard equation as [38]:

$$\frac{\partial \phi}{\partial t} = \nabla \cdot M \nabla \frac{\delta \mathcal{F}}{\delta \phi} \tag{2.6}$$

By coupling different fields and adding the corresponding energy terms into the free energy functional, the phase-field model can be applied to a wide variety of problems.

To describe brittle fracture, the phase-field parameter is used to identify the state of the material, i.e., intact body or crack. Depending on the models, ϕ can either be conserved or non-conserved. Therefore, both the Allen-Cahn and the Cahn-Hilliard equation were used in the literature.

2.5 The Phase-Field Fracture Models in the Mechanics Community

2.5.1 Basics of the Mechanical Models

Various criteria presented in Section 2.2 were developed to predict the crack path, and they were widely used in finite element simulations. However, most of them need to be applied repetitively at every small crack increment, and the accuracy largely depends on the mesh size.

With the global energy minimization assumption, Francfort and Marigo [39] proposed the variational formulation for quasi-static crack propagation in brittle materials. They showed that by minimizing the potential of the system, the crack path can be determined without additional criteria. Besides, compared with the damage models [40–42], the crack initiation can be captured by the model without having empirical relations. As demonstrated by various numerical examples [39], the model can predict crack initiation and propagation. However, it cannot simulate crack propagation under arbitrary loadings [39]. Besides, the definition of the crack as a discontinuity adds complexity to the numerical implementation.

In the image segmentation model, Ambrosio and Tortorelli [43] approximated the original discrete functional by Mumford and Shah [44] with a continuous energy functional. Since the variational formulation closely resembles the Mumford-Shah energy functional, inspired by Ambrosio and Tortorelli [43], Bourdin et al. [45] replaced the discontinuous crack with the diffuse-interface crack in the variational formulation. In the approximated formulation, an order parameter ϕ was introduced to represent the crack with $\phi = 0$ inside the crack and $\phi = 1$ in the bulk. With the Γ-convergence technique developed by Ambrosio and Tortorelli [43], the continuous energy functional was shown to converge to the variational formulation when the diffuse-interface crack converges to the discontinuous crack with a vanishing interface thickness. The continuous energy functional by Bourdin et al. is given by:

$$\mathcal{F} = \int_{\Omega} \left(f_{interfacial} + f_{elastic} \right) \, d\Omega \tag{2.7}$$

where $f_{interfacial}$ and $f_{elastic}$ are the density functionals of the interfacial energy and the elastic energy. The interfacial energy density is given as [45]:

$$f_{interfacial} = G_c \left(l(\nabla\phi)^2 + \frac{h(\phi)}{l} \right) \tag{2.8}$$

with [45]:

$$h(\phi) = \frac{(1-\phi)^2}{4} \tag{2.9}$$

where l is the internal length scale that controls the crack interface thickness, and $h(\phi)$ is the geometrical function that determines the shape of the crack interface. The whole term next to G_c in Equation (2.8) is called the crack surface density function. With this form of the crack surface density function, the 1D crack interface profile is given by [46]:

$$\phi = 1 - e^{-\frac{|x|}{2l}} \tag{2.10}$$

As shown in Figure 2.4, with l approaching 0, the diffuse-interface crack converges to the discontinuous crack. The elastic energy density reads [45]:

$$f_{elastic} = (g(\phi) + \eta)\,\frac{1}{2}\varepsilon(u) : [\mathbb{C}\varepsilon(u)] \tag{2.11}$$

where u is the displacement field, $\mathbb{C}$ is the stiffness tensor, and $\varepsilon(u)$ is the infinitesimal strain tensor given by:

$$\varepsilon(u) = \frac{1}{2}\left(\nabla u + (\nabla u)^T\right) \tag{2.12}$$

where T denotes the transpose of a tensor. $\frac{1}{2}\varepsilon(u) : [\mathbb{C}\varepsilon(u)]$ is the elastic energy density in the intact body, and $g(\phi)$ is the degradation function interpolating the elastic energy density in the crack ($\phi = 0$) and the bulk ($\phi = 1$). The degradation function $g(\phi)$ based on the Ambrosio-Tortorelli functional is defined as [45]:

$$g(\phi) = \phi^2 \tag{2.13}$$

η next to the degradation function in Equation (2.11) is the residual stiffness, which is a non-zero constant to ensure numerical stability [45]. To avoid the overestimation of the elastic energy, the value of it should be sufficiently small, e.g., less than 10^{-6}. Through optimizing the displacement field and the crack field to minimize the energy functional in Equation (2.7), both the stress distribution and the crack path are determined. The optimization was achieved utilizing the alternative minimization algorithm [45] in which at each time, one parameter is optimized while the other parameter is fixed. To prevent the unphysical self-healing behaviour of the crack, ϕ was not allowed to evolve once it becomes 0 [45]. Compared with the variational formulation, Bourdin et al.'s model [45] is easier to implement and has higher computational efficiency.

Kuhn and Müller [36, 47] then adopted the energy functional by Bourdin et al. [45]. Instead of using the alternative minimization algorithm, the crack field was governed by the

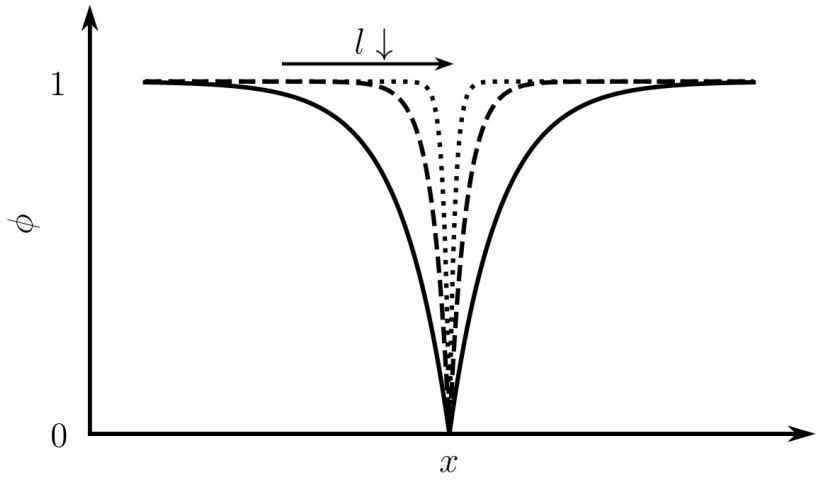

Figure 2.4: 1D analytical crack (ϕ) profiles with different values of the internal length scale (l) generated from Equation (2.10).

Ginzburg-Landau evolution equation. Combining Equations (2.7), (2.8), (2.11), the phase-field equation reads [36]:

$$\frac{1}{M}\frac{\partial \phi}{\partial t} = -\frac{\delta \mathcal{F}}{\delta \phi} = 2G_c l \nabla^2 \phi + \frac{G_c}{2l}(1-\phi) - \phi\varepsilon : [\mathbb{C}\varepsilon] \tag{2.14}$$

Since the stress is assumed to be in the equilibrium state in quasi-static fracture, the displacement field is governed by the mechanical equilibrium equation. By ignoring the body force, which is the force acting on the volume of the body, e.g., gravitational force, electromagnetic force, etc, the equation reads:

$$\nabla \cdot \sigma = 0 \tag{2.15}$$

where σ is the stress derived from the elastic energy density in Equation (2.11) given as [36]:

$$\sigma = \frac{\partial f_{elastic}}{\partial \varepsilon} = (\phi^2 + \eta)\mathbb{C}\varepsilon \tag{2.16}$$

Then for the first time, the model was called a phase-field model for its close resemblance to the phase-field models used to describe phase transformation. The order parameter for the crack, therefore, was referred to as the phase-field parameter. However, since the energy dissipation is assumed to happen instantaneously in brittle fracture, the time-dependent term $1/Md\phi/dt$ could delay the dissipation process and lead to the deviation from the Griffith theory. Kuhn and Müller [36] then showed that when the mobility is sufficiently large, the solutions are in good agreement with the Griffith theory. The non-conserved governing

equation for the phase-field parameter (Equation (2.14)) also makes it clear that the crack was treated as a non-conserved field in the models by Kuhn and Müller [36] and Bourdin et al. [45]. As a result, the volume of the body decreases during crack evolution. However, since the crack volume is much smaller than the domain size in simulations, the volume loss during crack evolution remains negligible.

Based on continuum mechanics and thermodynamics, Miehe et al. [1, 48] proposed an alternative continuous model in which the energy functional and the displacement equation are the same as Equations (2.7) and (2.15). Two types of governing equations for the phase-field parameter were introduced: the rate-dependent equation identical to Equation (2.14) and the rate-independent equation by setting M to infinity such that [1]:

$$2G_c l\nabla^2\phi + \frac{G_c}{2l}(1-\phi) - \phi\varepsilon : [\mathbb{C}\varepsilon] = 0 \tag{2.17}$$

Their model in essence is the same as those by Kuhn and Müller [36] and Bourdin et al. [45]. However, the phase-field variable was viewed as a damage variable with $\phi = 0$ as the fully damaged state or the crack state and with $\phi < 1$ as the partially damaged state containing microcracks. Therefore, instead of only constraining the evolution of $\phi = 0$, the phase-field parameter is forced to decrease ($d\phi/dt \leq 0$) so that both the crack and the partially damaged area cannot heal [1].

Different irreversibility criteria, i.e., $\phi = 0$ and $d\phi/dt \leq 0$, could potentially lead to different model responses. Therefore, Linse et al. [49] compared these two criteria by studying the uniaxial tension of a 1D elastic band. The accuracy of the results was evaluated by comparing the crack surface area with the analytical value derived from the surface density function in Equation (2.8). With $\phi \leq 0$, the crack surface area agrees well with the analytical value when the internal length scale (l) to domain size ratio is less than 0.05. With $d\phi/dt \leq 0$, however, the error surprisingly increases to over 100% with the decrease of the l to domain size ratio. They pointed out that the difference occurs only after the peak load since the partially damaged area recovers to the intact state ($\phi = 1$) when only constraining $\phi = 0$, while with the other criterion, ϕ keeps decreasing. The different predictions of the surface area also result in a slightly different load-displacement response after peak load [49]. Based on the accuracy of the surface area predictions, they then suggested that Miehe et al.'s irreversibility criterion, i.e., $d\phi/dt \leq 0$, could only be used before the peak load. However, the accuracy of the model cannot simply be determined from the 1D crack profile, since it is only a numerical feature. The influence of the irreversibility criteria should be investigated with 2D simulations in which the energy release rate and the crack pattern can be evaluated.

2.5.2 Interpretations of the Internal Length Scale (l)

Internal Length Scale as a Regularization Parameter

The internal length scale (l) was interpreted by Bourdin et al. [45] as a regularization parameter, which controls the convergence of the diffuse-interface crack to the discontinuous crack. Therefore, theoretically, l should be zero such that the energy functional can converge to the variational formulation. However, the smaller l requires a finer mesh to solve the equation, which leads to a higher computational cost.

Internal Length Scale as a Fitting Parameter

Ever since Amor et al. [50] illustrated that l can be related to the failure strength of the material, it has been more accepted as a fitting parameter rather than a regularization parameter. Amor et al. [50], Borden [51], and Pham and Marigo [52] studied the 1D uniaxial tension of an elastic band and provided the analytical stress-strain relation by assuming the homogeneous damage ($\nabla\phi = 0$) in the band. Combining Equations (2.15) and (2.17), the homogeneous solutions for the phase-field parameter and the stress read [51]:

$$\phi = \left(\frac{2lE}{G_c}\varepsilon^2 + 1\right)^{-1} \tag{2.18}$$

$$\sigma = \left(\frac{2lE}{G_c}\varepsilon^2 + 1\right)^{-2} E\varepsilon \tag{2.19}$$

The phase-field parameter and the stress with respect to the strain are shown in Figure 2.5. The peak stress and the corresponding strain in Figure 2.5b are the failure strain and stress, which are given by [51]:

$$\varepsilon_c = \sqrt{\frac{G_c}{6lE}} \quad , \quad \sigma_c = \frac{9}{16}\sqrt{\frac{EG_c}{6l}} \tag{2.20}$$

The homogeneous solutions are stable only before the critical load as the damaged area localizes, and $\nabla\phi = 0$ is no longer valid. Since σ_c agrees perfectly well with the failure strength obtained from both 1D and 2D uniaxial tension simulations [52–54], it can be used to determine the value of l. Besides, Equation (2.20) shows that σ_c becomes infinite when l approaches zero, which is consistent with the infinite strength predicted by the Griffith theory in the defect-less material. Various studies [55–58] have shown that the interpretation of l as a fitting parameter enables the accurate representation of the crack path and the load-displacement response. For example, Nguyen et al. [55] performed 3D three-point

bending simulations with l calculated from the failure strength reported from experiments, and good agreement in the load-displacement curve was obtained compared with experiments. However, even viewing l as a fitting parameter, the l to domain size ratio should still be sufficiently small to maintain accuracy. Zhang et al. [56] showed that although the load-displacement curve is accurate using a small domain size, the crack path deviates from experiments. Good accuracy of both the load-displacement curve and the crack path can be achieved only with a small internal length scale to domain size ratio.

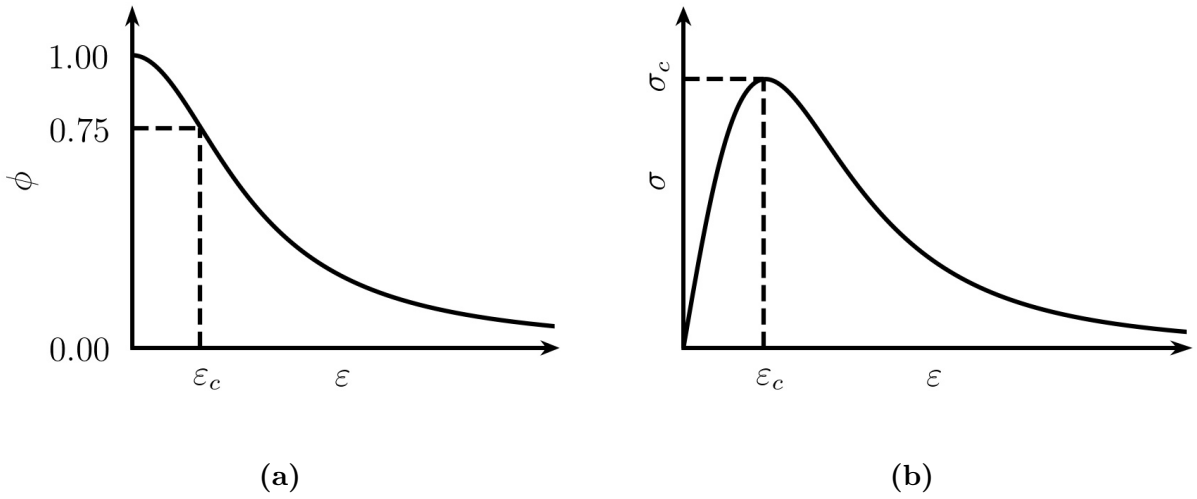

Figure 2.5: 1D homogeneous solutions for (a) the phase-field parameter (ϕ) and (b) the stress (σ) generated from Equations (2.18) and (2.19). ε_c and σ_c are the critical strain and stress for the breakage of the 1D band.

Until now, the interpretation of l as a fitting parameter is more popular, as it does not have to be arbitrarily small to converge to the discontinuous crack and can be related to experimental results. However, the connection of l with both the interface thickness and the failure strength leads to the dependence of the failure strength on the interface thickness. As pointed out by Zhang et al. [56], the l to domain size ratio still has to be very small to converge to the variational formulation, regardless of whether l is interpreted as a regularization parameter or a fitting parameter. Therefore, Wu [59] developed a model in which the failure strength is separated from l. Although the model has a similar energy functional as those proposed by Bourdin et al. [45] and Miehe et al. [1], the geometrical function ($h(\phi)$) and the degradation function ($g(\phi)$) are completely different. The model removes the dependence of the failure strength on l. As a result, the failure strength does not have to change, while the numerical convergence to the discontinuous crack can still be

guaranteed [59]. However, the model has not been evaluated extensively, and the limitation of the model is still unknown.

2.5.3 Model Variations

The models by Miehe et al. [1] and Bourdin et al. [45] share the same energy functional with only minor differences in the way they implement the model, e.g., different governing equations and irreversibility criteria. However, the models utilizing that energy functional all showed the same problems. For example, the stress-strain response before the peak load is nonlinear as shown in Figure 2.5b. Therefore, alternative forms of the energy functional were developed.

Alternative Forms of the Geometrical Function ($h(\phi)$)

The nonlinear stress-strain response is caused by the decrease of ϕ with the non-zero strain shown in Figure 2.5a, which is referred to as the damage accumulation in the literature. This unphysical phenomenon can also lead to strain energy release far from the crack [51]. Instead of adopting the quadratic function (Equation (2.9)), Pham et al. [52] suggested using the linear function, i.e., $9(1-\phi)/64$, as the geometrical function. They showed that the stress-strain relation becomes perfectly linear, and $\phi = 1$ before the failure stress. Besides, the crack interface profile is described by the quadratic function, which does not spread to the entire domain like the exponential function in Equation (2.10). Therefore, the boundary effect can be less significant. However, the linear function leads to the numerical issue as ϕ can exceed the 0 to 1 interval [60]. As a result, ϕ has to be bounded manually. Borden [51] then suggested using the cubic function, which results in the similar linear elastic behaviour before the failure stress and the bounded phase-field parameter. However, since an additional parameter is introduced in the cubic function, the failure stress becomes dependent on that parameter [51].

Alternative Forms of the Degradation Function ($g(\phi)$)

An alternative way to improve the linear elastic behaviour is to modify the degradation function since it also enters in the homogeneous solution. The degradation function should be constructed in a way such that $g(0) = 0$ and $g(1) = 1$. Meanwhile, the derivative of $g(\phi)$ with ϕ should be zero at $\phi = 0$ to avoid the elastic driving term inside the crack as shown in Equation (2.14) or (2.17) [61]. Kuhn et al. [61] then compared three degradation functions

that satisfy these requirements: the quadratic function, the cubic function, and the quartic function.

Homogeneous solutions with quartic and cubic function were given (Figure 2.6) in which the perfectly linear elastic behaviour and $\phi = 1$ were observed before the failure stress. However, with the cubic and the quartic function, they found that the crack nucleation happens only when the numerical perturbation is applied on the phase-field parameter. This is because there are two solutions: $\phi = 1$ and the homogeneous solution, and for both solutions, ϕ and the gradient of E with ϕ at the critical strain (ε_c^c or ε_c^q) are the same as shown in Figure 2.6 [61]. Therefore, the system will stay in $\phi = 1$ without perturbation. However, the influence of the perturbation was not evaluated.

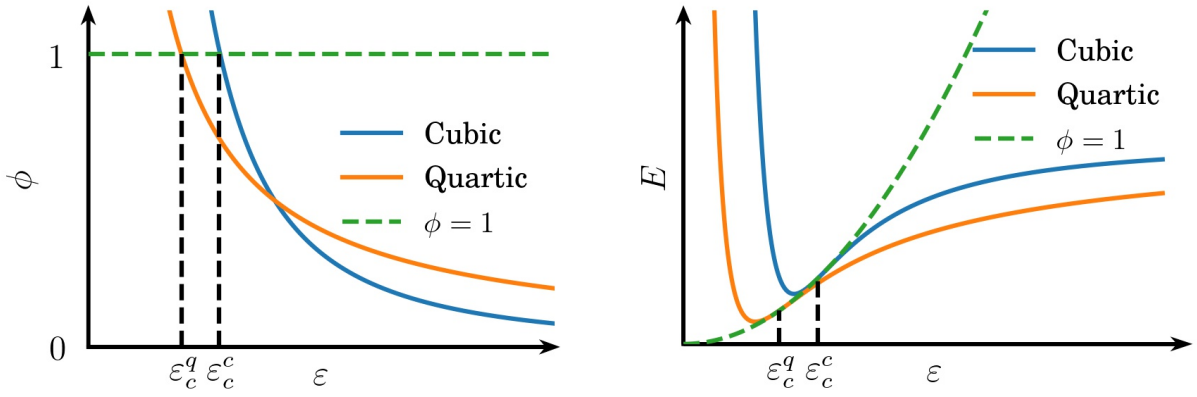

(a) **(b)**

Figure 2.6: 1D homogeneous solutions for (a) the phase-field parameter (ϕ), and (b) the corresponding energy density (E) with cubic and quartic degradation function. ε_c^c and ε_c^q are the critical strains for the breakage of the 1D band with the cubic and the quartic degradation function. Adapted from [61].

Higher-order Gradient Term of Phase-Field Parameter

To improve the convergence rate of the diffuse interface crack to the discontinuous crack, Borden [51] introduced the fourth-order phase-field term into the surface density function. The interfacial energy density then becomes [51]:

$$f_{interfacial} = G_c \left(\frac{l^3}{4} (\Delta\phi)^2 + \frac{l}{2} (\nabla\phi)^2 + \frac{(1-\phi)^2}{4l} \right) \tag{2.21}$$

At the same time, the 1D crack interface profile reads [51]:

$$\phi = 1 - \left(1 + \frac{|x|}{l}\right) e^{-\frac{|x|}{l}} \tag{2.22}$$

Compared with the original equation with the second-order phase-field term, the faster convergence rate of the interfacial energy to the analytical value (G_c) with the decrease of l was observed in 1D simulations. Besides, the high-order model gets rid of the residual stiffness [51]. However, the interface profile is still described by an exponential function that spreads to the entire domain. As a result, although the convergence rate to the analytical value is faster, the accuracy of the interfacial energy is still prone to the boundary effect. Besides, the Γ-convergence of the model was not available [51].

2.5.4 Model Applications

Crack Initiation and Quasi-static Crack Propagation

Although the interpretations of the parameters and the forms of the model can be different, these models are the same in essence and are capable of describing fracture phenomena. Among various fracture phenomena, crack nucleation has long been a difficult problem in the mechanics community. Same as the variational formulation, the phase-field model is also capable of simulating nucleation. The 1D homogeneous solution suggests that the crack nucleates when reaching the failure stress (Figure 2.5b). Meanwhile, ϕ decreases to 0.75 during the nucleation (Figure 2.5a). Kuhn and Müller [54] studied the crack nucleation from a circular notch in a 2D sample. Compared with the homogeneous solution, they found that ϕ decreases to 0.8 during nucleation, which is quite close to 0.75. Besides, the critical applied load for crack nucleation observed in 2D simulations is consistent with the failure stress in the homogeneous solutions. Therefore, the critical condition for crack nucleation in 2D phase-field simulations, i.e., critical load and decrease in ϕ, can be correctly described by the 1D homogeneous solutions. This finding was further proved by Tanné et al. [62] with more common experimental setups in which the crack nucleates from U and V-notches. However, they also found that the damage accumulation far from the crack could potentially lead to deviations of the critical load from experiments, which can be avoided by using the linear geometrical function.

Because of the simplified elastic energy expression in Equation (2.11), as pointed out by Amor et al. [50], the model is unable to distinguish between compression and tension. Therefore, Amor et al. [50] developed a so-called 'anisotropic' model [63] which accounts for

the asymmetric behaviour in tension and compression by decomposing the strain into the tensile strain, the compressive strain, and the shear strain, of which only the tensile strain and the shear strain contribute to crack propagation. Later on, similar 'anisotropic' models [64, 65] were proposed, of which the main difference is the way they decompose the strain.

However, anisotropy normally refers to the direction-dependent mechanical and material properties. Since the anisotropic elasticity is often less significant than the anisotropic failure strength [66], and it can be incorporated into the stiffness tensor in the constitutive equation, the anisotropic surface energy is worth more attention. By making the crack interfacial energy direction-dependent, Li et al. [67, 68], Teichtmeister et al. [69], and Nguyen et al. [66] proposed anisotropic models where interesting crack patterns, i.e., zigzag crack path [66–69], and good agreement with experiments [66] were observed.

Dynamic Crack Propagation

All those models were originally designed to study quasi-static crack propagation. However, with only a few changes, they can be extended to the dynamic case. In dynamic fracture, the release of elastic energy also leads to an increase in kinetic energy. The energy functional, therefore, becomes [70]:

$$\mathcal{F} = \int_{\Omega} \left(\frac{1}{2}\rho \left(\frac{\partial u}{\partial t} \right)^2 + G_c \left(l(\nabla\phi)^2 + \frac{h(\phi)}{l} \right) + \left(g(\phi) + \eta \right) \frac{1}{2}\varepsilon : [\mathbb{C}\varepsilon] \right) \, d\Omega \tag{2.23}$$

where ρ is the material density, and the first term is the kinetic energy. Since ρ is the same in the bulk and the crack, similar to the non-conversed volume discussed in Section 2.5.1, it also deviates from the reality. From the conservation of the linear momentum, the displacement-field equation reads [70]:

$$\rho \frac{\partial^2 u}{\partial t^2} = \nabla \cdot \sigma = \nabla \cdot \left((\phi^2 + \eta)\mathbb{C}\varepsilon \right) \tag{2.24}$$

As discussed in Section 2.3, the mechanisms behind the limiting velocity, branching velocity, and branching angle are still not well-understood. Therefore, to gain insights into the mechanisms, many researchers tried to reproduce the experimental results with phase-field simulations. For the limiting velocity, various phase-field studies [70–72] have reported it to be around $0.6C_r$, which agrees well with the commonly observed experimental results. Bleyer et al. [73] then showed that the crack accelerates to $0.9C_r$ when suppressing the branching with a tough material surrounding the crack path or with circular holes in the crack path. This finding suggests that the limiting velocity is the Rayleigh wave speed and is influenced

by the branching behaviour. The branching velocity from phase-field simulations, however, has not been reported in the mechanics community. Instead of focusing on the branching velocity, Bleyer et al. [73] showed that the crack starts branching when the energy release rate reaches $2G_c$, which is consistent with Eshelby's energetic theory [4]. As for the branching angle, Borden et al. [70] and Hofacker and Miehe [74] adopted the setting of the dynamic shear loading experiment by Kalthoff and Winkler [75]. Utilizing the phase-field model, they successfully reproduced the crack path observed in the Kalthoff-Winkler experiment.

Crack Propagation in Heterogeneous Materials

Most applications of the phase-field fracture models were in the macroscale, in which the materials are often assumed to be homogeneous with the same material properties across the domain. In the mesoscale, however, the material properties can vary within the domain because of the complex microstructures. Therefore, to study the interaction between crack propagation and microstructures, the critical energy release rate and the stiffness can no longer be homogeneous.

Hossain et al. [76] were the first to study crack propagation in a heterogeneous material. The model is the same as the homogeneous one, but the critical energy release rate and the stiffness become the functions of the position. Toughening of the material was observed with either heterogeneous elasticity or critical energy release rate in their simulations with simple laminar structures. Using the idea of Hossain et al. [76], Nguyen et al. [77, 78] then applied the model to more complex microstructures derived from experiments. In the simulations, different elastic properties were assigned to different phases. However, the critical energy release rate is assumed to be homogeneous in the domain. Through 2D and 3D simulations, they observed the inter-granular and trans-granular crack propagation behaviours.

Schneider et al. [79] extended the multi-phase-field model by Nestler et al. [80] for phase transformation to brittle fracture. In the energy functional, additional terms were added to account for the interfacial energy of the phase boundaries. Since there is no phase transformation in the process, only the crack interface was allowed to evolve [79]. For the first time, heterogeneous critical energy release rate, elasticity, and grain boundary weakening effect were all taken into account.

However, all these simulations lack quantitative comparisons with either experiments or fracture theories. The first quantitative comparison was made by Hansen-Dörr et al. [81] who compared the results with the crack deflection theory by He and Hutchinson [82]. In

the theory, the crack deflects or penetrates the boundary depending on the grain boundary angle and the interface toughness (G_c^{int}) to the bulk toughness (G_c^{bulk}) ratio as shown in Figure 2.7a. In Hansen-Dörr et al.'s model [81], the grain boundary toughness is lower than the bulk toughness and kept constant across the grain boundary. However, they pointed out that the energy release rate at the grain boundary is not equal to the grain boundary toughness because of the interaction between the crack interface and the grain boundary. As shown in Figure 2.7b, since the crack interface spreads to the bulk, the bulk toughness also contributes to the energy release rate. Therefore, with a wider grain boundary or a narrower crack interface, the influence of the bulk toughness can be reduced. The model by Schneider et al. [79] can also capture the grain boundary effect. However, the grain boundary energy is implicitly incorporated into the model through the interfacial energy term for the phase boundary. As a result, the actual critical energy release rate at the grain boundary is unknown. Therefore, the comparison with the crack deflection theory becomes much more tricky to do. Chen et al. [83] also developed a phase-field model accounting for the grain boundary effect, which showed good agreement with the crack deflection theory. However, instead of having a constant critical energy release rate at the grain boundary, the grain boundary toughness was defined as the lowest value in the middle of the boundary, which varies smoothly to the bulk. As a result, the actual energy release rate at the grain boundary is not the grain boundary toughness they claimed. Besides, the results seem questionable as the dynamic simulation was compared with the crack deflection theory, which is for the quasi-static case.

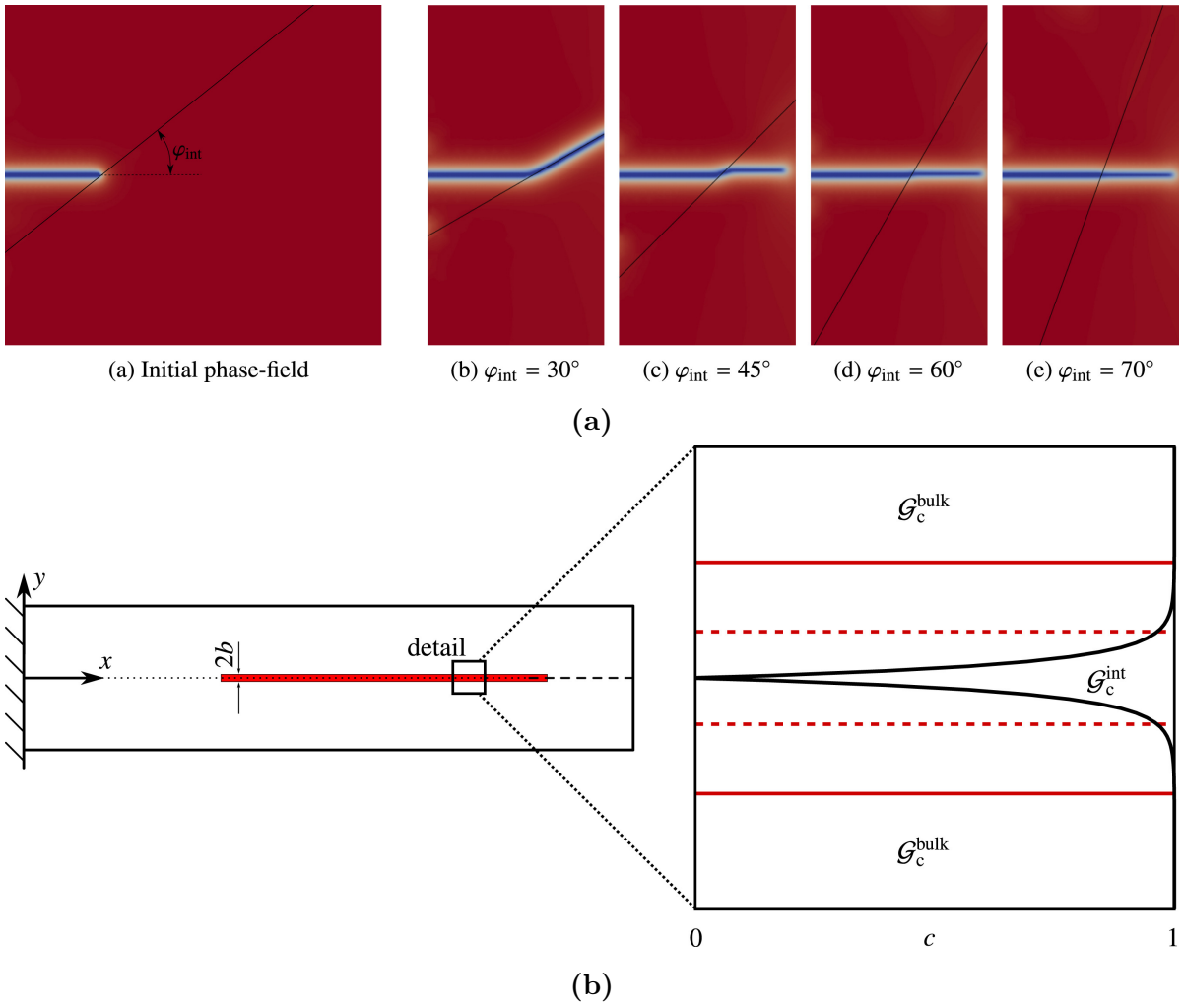

Figure 2.7: (a) Crack deflection and penetration behaviours at the grain boundary (black line) with different grain boundary angles (φ_{int}). (b) Schematics of the influence of the bulk toughness (G_c^{bulk}) on the interface toughness (G_c^{int}). In (b), the black solid curve is the crack surface profile, the red solid line indicates the width of the crack interface, and the red dotted line indicates the thickness of the grain boundary. Adapted from [81]. Reprinted with permission from Elsevier.

Crack Propagation with Plastic Deformation

The phase-field fracture model is very sophisticated in terms of describing perfect brittle fracture. However, for most materials, plastic deformation accompanies fracture. Unlike the linear stress-strain relation for brittle materials, beyond the yield stress, the stress becomes either constant in a perfect plastic material or increases linearly or nonlinearly with strain because of strain hardening. Upon unloading, not all the strain is recovered due to the permanent plastic deformation. Therefore, the strain can be decomposed into the recoverable elastic strain and the unrecoverable plastic strain. The potential of the system with plastic deformation then reads [84]:

$$\mathcal{F} = \int_{\Omega} \left(f_{elastic} + f_{plastic} + f_{dissipation} \right) \, d\Omega \tag{2.25}$$

where $f_{plastic}$ is the plastic free energy, and $f_{dissipation}$ is the dissipated energy caused by plasticity. Combining the energy functionals for fracture (Equation (2.7)) and plastic deformation (Equation (2.25)), several researchers [85–92] then proposed the phase-field models for ductile fracture. The energy functionals used in these models can be generalized as [84]:

$$\mathcal{F} = \int_{\Omega} \left(f_{interfacial} + f_{elastic} + p(\phi) f_{plastic} + d(\phi) f_{dissipation} \right) \, d\Omega \tag{2.26}$$

where $p(\phi)$ and $d(\phi)$ are the coupling functions between fracture and plastic deformation.

Most of the models considered a linear hardening behaviour, while Miehe et al. [91] gave a more general formulation for both linear hardening and nonlinear hardening. However, the main difference is how they couple plasticity.

Distinct from all the other models, there is no coupling between the plastic deformation and crack propagation in the model by Duda et al. [86], which means that $p(\phi)$ and $d(\phi)$ are both equal to one. As a result, crack propagation is only driven by the elastic energy, which leads to the same crack propagation behaviour like that in brittle fracture.

Similar to the model by Duda et al. [86], another unique model was proposed by Ambati et al. [87] in which $p(\phi)$ and $d(\phi)$ are equal to one. However, instead of employing the original degradation function ($g(\phi)$) for brittle fracture like Duda et al. [86], $g(\phi)$ is modified to couple plasticity. In the degradation function, they introduced a threshold value identifying the critical plastic deformation, and fracture is triggered when plastic deformation exceeds the critical value.

All the other models coupled the plastic deformation through $p(\phi)$ and $d(\phi)$ while $g(\phi)$ was kept the same as that in brittle fracture. Borden et al. [89], Kuhn et al. [92], and Miehe

et al. [91] suggested using the same quadratic function for $g(\phi)$, $p(\phi)$, and $d(\phi)$, while various forms of the coupling functions were used in other studies [85–88, 90].

The different choices of the degradation function lead to different responses of the model, e.g., plastic strain evolution, stress-strain diagram, etc [84]. In general, the coupling of crack propagation with plasticity remains a challenge, and most of the models are in the theoretical stage with no comparison with experiments. The only exception is the work by Ambati et al. [90], in which the necking behaviour was captured, and the load-displacement curves were in good agreement with experiments.

2.6 The Phase-Field Fracture Models in the Physics Community

2.6.1 General Overview of the Phase-Field Fracture Models in the Physics Community

To understand dynamic fracture phenomena, phase-field models have also become popular in the physics community. Although the models share the same name as those in the mechanics community, they are different in many aspects.

The first phase-field fracture model in the physics community was developed by Aranson et al. [93], where the crack was identified as the normalized mass density of the material with 0 in the crack and 1 in the bulk. The displacement equation is similar to Equation (2.24) except that the density is replaced by the normalized mass density. Besides, to interpolate the stiffness in the crack interface, the stiffness was assumed to be linearly dependent on the normalized density. The evolution of the normalized density is governed by the Ginzburg-Landau type evolution equation with a very simple energy functional only consisting of the gradient energy term and the double-well term. Utilizing the model, they then captured the branching behaviour and the velocity oscillation phenomenon. However, the oversimplified energy functional leads to the unphysical logarithmic dependence of the crack thickness on the domain size [93].

To address this problem, Karma et al. [2] proposed a phase-field model later on known as the Karma-Kessler-Levine (KKL) model. Although the energy functional in the KKL model is unique, the governing equations are the same as those in the mechanical models.

Based on the well-defined sharp-interface equations for the interface migration in the phase

transformation problem, Brener and Spatschek [94] and Spatschek et al. [95] developed a phase-field fracture model. In the model, they assumed that the crack interface migration can be described by the same set of sharp-interface equations. Utilizing the model, they then observed the branching instability and showed that the critical energy for crack propagation agrees well with the Griffith theory. More importantly, instead of ignoring the crack tip shape like all the other phase-field fracture models, the crack tip curvature can be chosen freely. However, the sharp-interface equations describing phase transformation may not be applicable for crack propagation. Therefore, quantitative comparisons with experiments and theories are required to verify the model.

Almost all the phase-field fracture models are non-conversed. The only exception is the model by Eastgate et al. [96] in which the phase-field parameter is defined as the normalized mass density and governed by the diffusion equation. Unfortunately, the phase-field parameter inside the crack cannot go to 0, and the value is proportional to the strain in the crack [97].

Although many models showed promising results, most of them lack quantitative comparisons with experiments or theories. The KKL model, as an exception, is the most well-developed model, and has reproduced various dynamic fracture phenomena, e.g., dynamic crack branching [35, 98, 99], crack path oscillation [100], lance-shaped structure [101], etc. Therefore, only the KKL will be discussed in this context.

2.6.2 Basics of the KKL Model

As in other phase-field fracture models, the crack is identified with an order parameter ϕ in the KKL model. With the phase-field parameter, the energy functional reads [98]:

$$\mathcal{F} = \int_{\Omega} \left(\frac{1}{2}\rho \left(\frac{\partial u}{\partial t} \right)^2 + \frac{\kappa}{2}(\nabla\phi)^2 + V(\phi) + g(\phi) \left(\frac{1}{2}\varepsilon : [\mathbb{C}\varepsilon] - \mathcal{E}_c \right) \right) \, d\Omega \tag{2.27}$$

where κ is the coefficient related to the surface energy, $\mathcal{E}_c$ is the critical elastic energy density to break the material, and $V(\phi)$ is the double-well function given as [2]:

$$V(\phi) = m\phi^2(1-\phi)^2 \tag{2.28}$$

where m determines the height of the double-well barrier. As demonstrated by Karma and Lobkovsky [35], in mode III fracture, when m equals 0, the critical branching velocity is the closest to the theoretical prediction by Adda-Bedia [5]. However, in other fracture modes, the proper range of m was not given. The first term in Equation (2.27) is the kinetic energy,

and the rest of the terms are the interfacial and elastic energy. The elastic energy expression, i.e., $g(\phi)\frac{1}{2}\varepsilon : [\mathbb{C}\varepsilon]$, is almost the same as those in the mechanical models, except that the degradation function is different. According to Karma et al. [2], the order of the function should be greater than 3 so that the strain can be released through the crack. Therefore, the degradation function was defined as [2]:

$$g(\phi) = 4\phi^3 - 3\phi^4 \tag{2.29}$$

The interfacial energy density, however, is different from those in the mechanical models and is given as [2]:

$$f_{interfacial} = \frac{\kappa}{2}(\nabla\phi)^2 + V(\phi) + (1 - g(\phi))\,\mathcal{E}_c \tag{2.30}$$

As in the models by Kuhn and Müller [36], and Miehe et al. [48], the phase-field parameter is governed by the Ginzburg-Landau evolution equation given as [2]:

$$\frac{1}{M}\frac{\partial\phi}{\partial t} = -\frac{\delta\mathcal{F}}{\delta\phi} = \kappa\nabla^2\phi - 2m\phi(1-\phi)(1-2\phi) - 12(\phi^2-\phi^3)\left(\frac{1}{2}\varepsilon : [\mathbb{C}\varepsilon] - \mathcal{E}_c\right) \tag{2.31}$$

The mobility (M), similar to that in the mechanical models, delays the energy dissipation, and therefore should be sufficiently large to obtain good agreement with the Griffith theory [35]. As in the mechanical models, to prevent the unphysical recovery of the crack, two kinds of irreversibility criteria were introduced, i.e., $\phi = 0$ [35] and $d\phi/dt \leq 0$ [98]. The comparison between two irreversibility criteria, however, is missing in the literature. Based on the conservation of the linear momentum, the displacement equation is given by:

$$\rho\frac{\partial^2 u}{\partial t^2} = \nabla\cdot\left((4\phi^3 - 3\phi^4)\mathbb{C}\varepsilon\right) \tag{2.32}$$

By solving Equation (2.31) with the displacement set to 0, the crack interface profile in 1D (Figure 2.8) reads [102]:

$$\frac{\partial\phi}{\partial x} = \sqrt{\frac{2\mathcal{E}_c}{\kappa}\left(1 - g(\phi) + \frac{V(\phi)}{\mathcal{E}_c}\right)} \tag{2.33}$$

Combining Equations (2.30) and (2.33), the critical energy release rate reads [35]:

$$G_c = 2\sqrt{2\kappa\mathcal{E}_c}\int_0^1 \sqrt{1 - g(\phi) + \frac{V(\phi)}{\mathcal{E}_c}}\; d\phi \tag{2.34}$$

As in the mechanical models, the diffuse-interface approximation of the crack leads to the deviation from the LEFM. Therefore, the interface thickness to domain size ratio has to be sufficiently small. As demonstrated by Karma and Lobkovsky [35], the critical branching velocity showed good agreement with the fracture theory when the interface thickness to domain size ratio approaches 0.

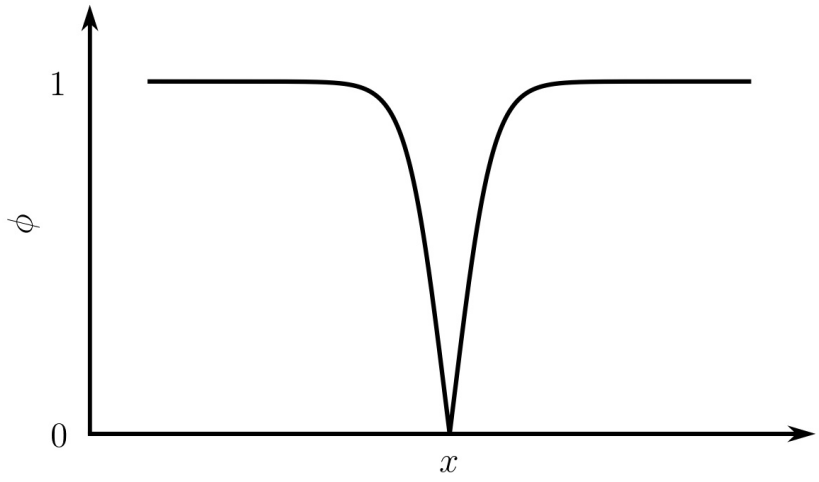

Figure 2.8: The 1D analytical phase-field profile in the KKL model generated from Equation (2.33).

2.6.3 Applications of the KKL Model

Dynamic Crack Propagation

Distinct from the mechanical models, all the applications of the KKL model are limited to dynamic brittle fracture with no application for quasi-static fracture. However, compared with the mechanical models, the KKL model reproduced broader dynamic fracture phenomena and enables deeper insight into the dynamic fracture mechanisms.

Utilizing the basic KKL model, Karma and Lobkovsky [35] studied 2D branching phenomena in mode III fracture and found that the critical branching velocity is $0.41C_s$ and the branching angle is 70° which are close to Adda-Bedia's predictions, i.e., $0.39C_s$ and 79.2°. However, the model cannot distinguish between compression and tension because of the simplified elastic energy expression, which limits its application to more general loading conditions. Henry and Levine [100], then decomposed the elastic energy to guarantee that the material cannot break under compression. Utilizing the 'anisotropic' model, they observed the oscillated crack path under biaxial strain, which agrees well with the experiments.

Henry [98] then studied the 2D branching phenomena in mode I fracture. Although the branching velocity is in good agreement with the theoretical prediction, it is much higher than the experimental observations. Henry then suggested that the discrepancy comes from the 2D simplification of 3D experiments. To demonstrate that point, they did a series of 3D

simulations. Starting with the 3D straight crack propagation under mode I loading, Henry [103] observed that the crack front in the thickness direction is elliptical rather than straight as assumed in 2D. Then Henry and Adda-Bedia [99] studied the 3D branching phenomena under the same loading condition. They found that with a thin plate, the branch starts locally and spreads to the whole thickness of the plate, and eventually looks like the pattern observed in 2D simulations. However, the crack pattern becomes very complex with a thick plate, which agrees well with the experiments. Meanwhile, the crack velocity is lower in the thick plate because more elastic energy is consumed to create the complex crack pattern leaving less energy for the kinetic energy [99]. Therefore, this finding gives one plausible explanation for the higher branching velocity predictions in 2D simulations compared with experiments. To understand the lance-shaped structure under mixed-mode (I and III) loading condition observed in experiments, Pons and Karma [101] managed to reproduce the phenomenon with 3D simulations and provided insights into the possible mechanisms of the formation of the structure.

The anisotropic model with the direction-dependent fracture energy was proposed by Hakim and Karma [104], in which the anisotropy was added through the gradient term $(\kappa/2(\nabla\phi)^2)$ in the interfacial energy in Equation (2.30). Mesgarnejad et al. [105] then applied the model to study crack propagation in orientationally ordered composites, and the crack path was in good agreement with experiments.

Crack Propagation in Two-Phase Materials

Apart from the numerous applications in isotropic and anisotropic fracture, Henry [106] also applied the model to study crack propagation in two-phase materials. In the study, only the heterogeneous critical energy release rate was considered and was by modifying G_c in Equation (2.34). With the model, Henry studied crack propagation in a two-phase system, in which a titled boundary separates the materials with different values of G_c (Figure 2.9a). An initial crack was then placed in the weak material. By applying the load less than the amount allowing crack propagation in the strong material but higher than that for crack propagation in the weak material, the crack was supposed to either propagate along the boundary or stop at the boundary. The critical energy for the continuous crack propagation along the boundary at various grain boundary angles was compared with the theory. With G_c in the strong material much larger than that of the weak material, the results agreed qualitatively well with the theory (Figure 2.9b). However, when G_c for the strong material becomes twice

that of the weak material, the unphysical penetration of the grain boundary was observed. Therefore, Henry suggested that the material heterogeneity cannot be incorporated simply by modifying G_c as the interaction between the crack interface and the heterogeneous critical energy release rate leads to the unphysical crack penetration behaviour. However, more investigations into the unphysical behaviour are required as the interaction between the crack interface and the heterogeneity also exists in the mechanical models, while the mechanical models showed good agreement with theories.

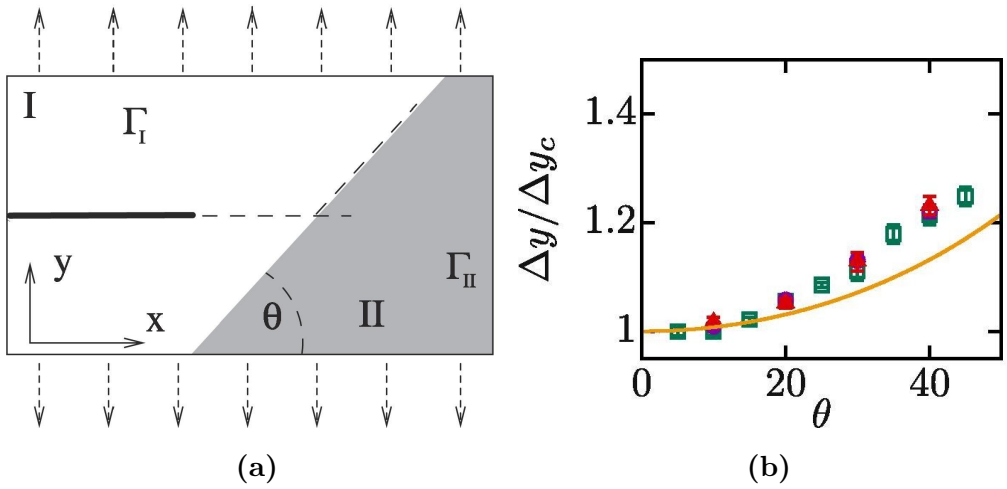

Figure 2.9: (a) The simulation setup in which a boundary with an angle θ separating two materials with I being the weak material with toughness Γ_I and II being the tough material with toughness Γ_{II}. (b) Comparison between the critical load (Δ_y/Δ_{yc}) for continuous crack propagation at the boundary from phase-field simulations and that from the theoretical predictions with different boundary angles. Green and red markers are from phase-field simulations with different domain sizes. Adapted from [106]. Reprinted with permission from Elsevier.

Chapter 3

Scope and Objectives

The work aims to compare phase-field fracture models developed by the mechanics and the physics community. In particular, two fracture models are examined: the phase-field fracture model by Miehe et al. [1] shortened as the mechanical model and the KKL model, which is the most well-developed model in the physics community. Since the standard mechanical model and the KKL model are for brittle fracture in isotropic materials, most simulations are based on that setting. The overall goal can be achieved through a sequence of objectives given below:

- The mechanical model and the KKL model will be implemented in the quasi-static setting. For the KKL model, it will be the first time in the literature to have quasi-static applications. First, parameter analysis will be carried out to derive the proper ranges of the model parameters. Then, simulation results will be compared with the Griffith theory to evaluate their abilities in capturing the quasi-static fracture phenomena. The fracture phenomena in heterogeneous materials will also be briefly covered by investigating crack propagation in a bi-grain system.

- The dynamic fracture phenomena will be studied utilizing the mechanical model and the KKL model. First, parameter analysis will be performed to determine the proper ranges of the parameters. Then, the theories by Eshelby [4] and Adda-Bedia [5] will be utilized to evaluate the accuracy of the models.

Chapter 4

Methodology

4.1 Introduction

Two types of phase-field fracture models, i.e., the mechanical model and the KKL model, were employed in this study to assess their abilities in capturing quasi-static and dynamic fracture phenomena. In the present work, two scenarios were studied, i.e., the snap-back of a 1D elastic band (Figure 4.1a) and crack propagation in a 2D rectangular sheet (Figure 4.1b). Because this project does not intend to study crack initiation, in both scenarios, an initial crack with $\phi = 0$ is manually placed in the domain. Since the computational cost in 2D is much higher than that in 1D, the 1D simulations are to determine the ranges of the numerical parameters. Distinct from the 1D case where the loading direction is constrained to the x-axis, there are multiple loading directions in 2D. Among all the fracture modes, the mode III fracture was investigated in 2D as other loading conditions, e.g., mode I, II, and mixed-mode, would require the use of the 'anisotropic' models to distinguish between compression and tension. Besides, in both communities, there are different types of 'anisotropic' models, which would add extra complexity to the analysis. Therefore, although the mode III fracture is of little practical relevance, it is still investigated in this project. Meanwhile, the energy functionals and governing equations are briefly reviewed, since they are more specific rather than generic as those in Chapter 2. Then along with the initial and boundary conditions defined based on the simulation setting, various numerical techniques were utilized to translate the models into computer programs. Since this work does not intend to compare results with experiments, the parameters used in the simulations are dimensionless.

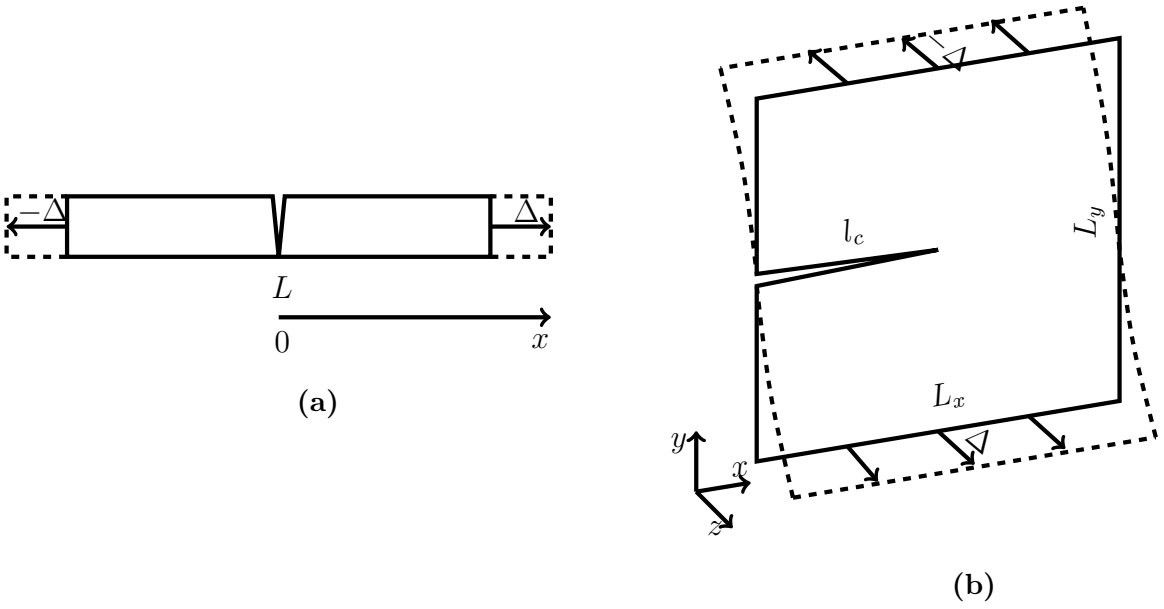

Figure 4.1: Simulation setups for (a) the snap-back of a 1D elastic band and (b) crack propagation in a 2D rectangular sheet.

4.2 Energy Functional and Governing Equations

4.2.1 The Mechanical Model

Although numerous attempts have been made to replace the energy functional proposed by Bourdin et al. [45], and some showed promising results, serious drawbacks of these models make them less popular. Therefore, Bourdin et al.'s energy functional [45], as the most popular one in the mechanics community, was adopted in this project. In the 1D setting, the stiffness tensor ($\mathbb{C}$) is reduced to Young's modulus (E), and the 1D strain tensor (ε) can be simplified to ∇u. Similarly, in 2D mode III fracture, with the antiplane shear condition, $\mathbb{C}$ is reduced to shear modulus (μ). Meanwhile, the displacement field becomes a scalar field with non-zero values only in the thickness direction (z-direction). Therefore, the energy functional in Equation (2.12) is simplified to:

$$\mathcal{F} = \int_{\Omega} \left(G_c \left(l(\nabla\phi)^2 + \frac{(1-\phi)^2}{4l} \right) + \left(\phi^2 + \eta\right) \frac{1}{2} C(\nabla u)^2 \right) \, d\Omega \tag{4.1}$$

where C represents Young's modulus (E) in 1D and the shear modulus (μ) in 2D. Instead of deriving the phase-field and displacement field solution by alternative minimization method, the rate-independent phase-field equation and the displacement equations proposed by Miehe et al. [1] were implemented since they are much more popular in the mechanics community.

Later on, the mechanical model would refer to Miehe et al.'s model. Based on Equation (4.1), the governing equations read:

$$2G_c l\nabla^2\phi + \frac{G_c}{2l}(1-\phi) - C\phi\left(\nabla u\right)^2 = 0 \tag{4.2}$$

$$\nabla\cdot\sigma = C\nabla\cdot\left(\left(\phi^2+\eta\right)\nabla u\right) = \begin{cases} 0 & \text{quasi-static} \\ \rho\frac{\partial^2 u}{\partial t^2} & \text{dynamic} \end{cases} \tag{4.3}$$

Distinct from the displacement equations, extra constraints are required when solving the phase-field equation such that the crack ($\phi = 0$) cannot recover to the intact state ($\phi = 1$). Unless explicitly mentioned, $d\phi/dt \leq 0$ was employed in the simulations.

4.2.2 The KKL Model

As for the KKL model, since the branching velocity in mode III fracture agrees well with Adda-Bedia's theory [5] when neglecting the double-well function according to Karma and Lobkovsky [35], the double-well term was removed in the simulations as well. Therefore, the energy functional can be simplified to:

$$\mathcal{F} = \int_\Omega \left(\frac{\kappa}{2}(\nabla\phi)^2 + \left(4\phi^3 - 3\phi^4\right)\left(\frac{1}{2}C(\nabla u)^2 - \mathcal{E}_c\right)\right)\, d\Omega \tag{4.4}$$

Compared with the rate-dependent phase-field equation used in the literature, the rate-independent equation has higher accuracy. Therefore, to be consistent with the mechanical model, the rate-independent equation was adopted for the KKL model. By setting M to infinity in Equation (2.31), the phase-field equation becomes:

$$\kappa\nabla^2\phi - 12\left(\phi^2-\phi^3\right)\left(\frac{1}{2}C\left(\nabla u\right)^2 - \mathcal{E}_c\right) = 0 \tag{4.5}$$

As in the mechanical model, $d\phi/dt \leq 0$ was enforced to prevent the recovery of the crack. By substituting the simplified energy functional (Equation (4.4)) into the mechanical equilibrium equation ($\nabla\cdot\sigma = 0$) and Equation (2.32), the displacement equations in quasi-static and dynamic fracture read:

$$\nabla\cdot\sigma = C\nabla\cdot\left(\left(4\phi^3-3\phi^4\right)\nabla u\right) = \begin{cases} 0 & \text{quasi-static} \\ \rho\frac{\partial^2 u}{\partial t^2} & \text{dynamic} \end{cases} \tag{4.6}$$

4.3 Numerical Techniques

Since the phase-field equations and the displacement equations are non-linear partial differential equations, they were discretized by the explicit finite difference method (FDM). With FDM, the computational domain was first discretized into linear grids in 1D or square Cartesian grids in 2D. Then, the space derivatives were approximated with the central finite difference method. For example, the second derivative of ϕ at the grid point (i, j) in 2D reads:

$$\nabla^2\phi = \frac{\partial^2\phi}{\partial x^2} + \frac{\partial^2\phi}{\partial y^2} \approx \frac{\phi_{i+1,j} - 2\phi_{i,j} + \phi_{i-1,j}}{dx^2} + \frac{\phi_{i,j+1} - 2\phi_{i,j} + \phi_{i,j-1}}{dx^2} \tag{4.7}$$

where dx is the mesh size.

After discretization, the phase-field and mechanical equilibrium equation were solved by iteration methods. In the iteration methods, the discretized equation is reformulated such that the grid-point value is calculated by its nearest neighbours. For example, in the mechanical model, ϕ at the grid point (i) in 1D is given as:

$$\phi_i = \varphi(\phi_{i+1}, \phi_{i-1}) = \frac{2G_c l\left(\phi_{i+1} + \phi_{i-1}\right) + dx^2\left(\frac{G_c}{2l} + C\left(\nabla u\right)^2\right)}{4G_c l + dx^2\left(\frac{G_c}{2l} + C\left(\nabla u\right)^2\right)}, i = 1, 2, \ldots n \tag{4.8}$$

where φ is the function of the nearest neighbours of ϕ_i. Then an initial guess $(\phi_1^0, \phi_2^0, \ldots \phi_n^0)$ is made based on the initial condition. By substituting the initial guess into the righthand-side of Equation (4.8), the first approximation $(\phi_1^1, \phi_2^1, \ldots \phi_n^1)$ after the first iteration can be derived. The iteration then continues until the largest relative difference between the current and previous iteration, i.e., $\max_{i=1,2,\ldots n}(|(\phi_i^k - \phi_i^{k-1})/\phi_i^k|)$, becomes smaller than an imposed threshold value.

Both Gauss-Seidel iteration and Jacobi iteration are based on the same idea. However, the rule updating the grid-point value is different. With the Jacobi iteration, the update rule is expressed as: $\phi_i^k = \varphi(\phi_{i-1}^{k-1}, \phi_{i+1}^{k-1})$, and the points are not updated until the end of one iteration. With Gauss-Seidel iteration, the updated value enters into the calculation of the next grid point immediately. For example, after calculating ϕ_2^1 with $\varphi(\phi_1^0, \phi_3^0)$, ϕ_2^1 is used to calculate the next grid point such that $\phi_3^1 = \varphi(\phi_2^1, \phi_4^0)$ and so on.

Since the current and previous iterations appear on different sides of the update rule in the Jacobi iteration ($\phi_i^k = \varphi(\phi_{i-1}^{k-1}, \phi_{i+1}^{k-1})$), the parallel programming is accessible as the domain can be divided into subdomains, and the grid points in those subdomains can be updated parallelly. Although the Gauss-Seidel iteration cannot be parallelized, the convergence rate is much faster than that of the Jacobi iteration. After numerous tests, it was observed that

the computational cost is the lowest when solving the phase-field equation with the Gauss-Seidel iteration and the mechanical equilibrium equation with the paralleled code by Jacobi iteration. Therefore, the phase-field equations were solved by the Gauss-Seidel iteration, and the mechanical equilibrium equations were solved by the Jacobi iteration and parallelized with the OpenMP library.

The only time-dependent equations are the displacement equations in the dynamic case where the time derivative is approximated by the explicit Euler scheme given as:

$$\frac{\partial^2 u}{\partial t^2} \approx \frac{u^{t+dt} - 2u^t + u^{t-dt}}{dt^2} \tag{4.9}$$

where dt is the time step, u^{t-dt}, u^t and u^{t+dt} are displacements at previous, current and next time step. To obtain the suitable ranges of numerical parameters, i.e., the threshold values in the iteration methods, the mesh size, the time step size, etc, a series of sensitivity analyses were carried out in Chapter 5.

4.4 Initial and Boundary Conditions

4.4.1 Initial Conditions

After discretizing the domain into Cartesian grids, the initial and boundary condition should be assigned based on the simulation settings. In 1D, an initial crack ($\phi = 0$) is placed in the middle of the band with two ends stretched as shown in Figure 4.1a. The crack interface is initialized by the analytical phase-field profile (Equation (2.10) or (2.33)).

For 2D simulations, the setting is shown in Figure 4.1b: an edge crack is positioned in the middle of a rectangular sheet with the top and bottom boundary stretched in the thickness direction (z-direction). Since the 1D analytical crack profile cannot be assigned to a 2D domain directly. The initial phase-field profile is determined by solving the phase-field equation with the displacement (u) set to 0. In this case, the initial guess for the phase-field parameter has to be set in the iteration methods. Because $d\phi/dt \leq 0$ was enforced as the irreversibility criterion, the initial guess of ϕ cannot be chosen arbitrarily. Instead, it should be narrower than the analytical profile such that ϕ can decrease to reach that profile. Figure 4.2 shows the initial guess of the phase-field parameter in the simulations. Apart from the crack where ϕ equals 0, ϕ at other points is set to 1. The crack interface then becomes a linear line with a slope equal to $1/dx$. For the displacement field, the domain is elastically stretched initially such that the strain is distributed uniformly.

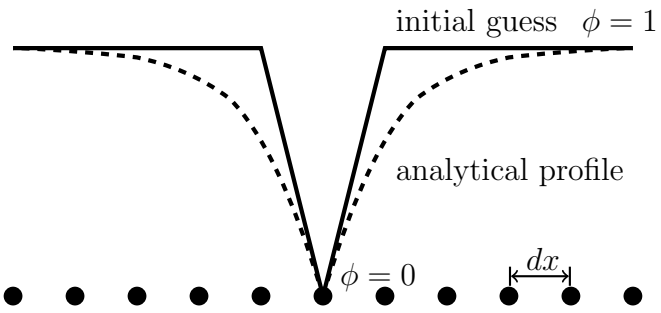

Figure 4.2: Schematics of the initial guess (solid line) and the analytical solution (dotted line) for the ϕ profile at interface. The circular dots represent the meshes.

4.4.2 Boundary Conditions

After setting the initial conditions, proper boundary conditions should be employed throughout the simulations. As for the displacement field, the boundary condition depends on the loading condition. In 1D simulations, since the two ends are stretched, the Dirichlet boundary condition was applied where the boundary displacements were fixed and set to Δ on the right end and $-\Delta$ on the left end (Figure 4.1a). Neglecting the initial crack, the band is elastically stretched, such that the input elastic energy (E_{in}) in the system reads:

$$E_{in} = \frac{1}{2} C \left(\frac{2\Delta}{L} \right)^2 L = \frac{2C\Delta^2}{L} \tag{4.10}$$

where L is the length of the elastic band.

Similarly, the Dirichlet boundary condition was applied at the top and bottom boundary in 2D simulations where u equals Δ at the bottom and $-\Delta$ at the top (Figure 4.1b). The input elastic energy is defined as the elastic energy along the width direction (y-direction) per unit length in the length direction (x-direction) since it has the same unit as the critical energy release rate. Therefore, the input elastic energy reads:

$$E_{in} = \frac{1}{2} C \left(\frac{2\Delta}{L_y} \right)^2 L_y = \frac{2C\Delta^2}{L_y} \tag{4.11}$$

where L_y is the width of the sheet. Since the left and right boundary are free from the external load, the boundary condition reads:

$$\sigma \cdot n = C \left(\nabla u \right) \cdot n = C \left(\frac{\partial u}{\partial x}, \frac{\partial u}{\partial y} \right) \cdot n = C \frac{\partial u}{\partial x} = 0 \tag{4.12}$$

where n is the vector normal to the boundary. The gradient of displacement in the x-direction equals zero, which corresponds to the zero-flux boundary condition. In the traditional fracture

models, i.e., sharp interface models, the zero-flux boundary condition should also be imposed on the crack surface since it is free from the load. However, in both the mechanical model and the KKL model, this condition is implicitly incorporated into the equation as inside the crack, i.e., $\phi = 0$, the stress is zero in both models (Equations (4.3) and (4.6)).

Unlike the boundary conditions for the displacement field, which have clear physical meanings, the phase-field boundaries are more related to the numerical outcomes. In the mechanics community, the zero-flux boundary condition was applied at all the phase-field boundaries. However, in the KKL model, the Dirichlet boundary condition ($\phi = 1$) was adopted at the top and bottom boundary to avoid the breakage of the loading boundaries. To compare these boundary conditions, 2D quasi-static simulations were carried out. In the simulations, each type of boundary condition, i.e., Dirichlet condition or zero-flux condition, was applied at all phase-field boundaries at a time in both models. The parameters for the simulations are listed in Table 4.1. To translate the models into computer programs, C language and the parallel programming library (OpenMP) were used. The codes can be found in Appendices A and B. With the output files from the program, the results were visualized with Python utilizing the Matplotlib library.

Table 4.1: Parameters in 2D quasi-static simulations

Symbol	Parameter	Value
L_x	Length of the 2D sheet	50
L_y	Width of the 2D sheet	50
l_c	Length of the initial crack	15
l	Internal length scale in the mechanical model	1
C	Shear modulus	1
G_c	Critical energy release rate	0.5
E_{in}	Input elastic energy	1
δ	Crack interface thickness	4
κ	Coefficient before the gradient term in the KKL model	1.26
$\mathcal{E}_c$	Critical elastic energy to break the material	0.05
η	Residual stiffness	10^{-10}
dx	Mesh size	0.1
$\Delta\phi_{threshold}$	Threshold value for ϕ in the iteration methods	10^{-5}
$\Delta u_{threshold}$	Threshold value for u in the iteration methods	10^{-7}

As shown in Figures 4.3a and 4.3c, the Dirichlet condition leads to the distortion of ϕ at the left boundary for both models, and the non-zero gradient of ϕ at the rest of the boundaries for the mechanical model. The zero-flux condition, on the contrary, works well on all boundaries for both models (Figures 4.3b and 4.3d). The non-zero gradient of ϕ at boundaries can affect the stress distribution and alter the crack propagation behaviour. Since the zero-flux boundary condition was used in the mechanical model in the literature, and it is identical to the Dirichlet condition at all the boundaries except the left one in the KKL model, it was adopted in both models in the following simulations.

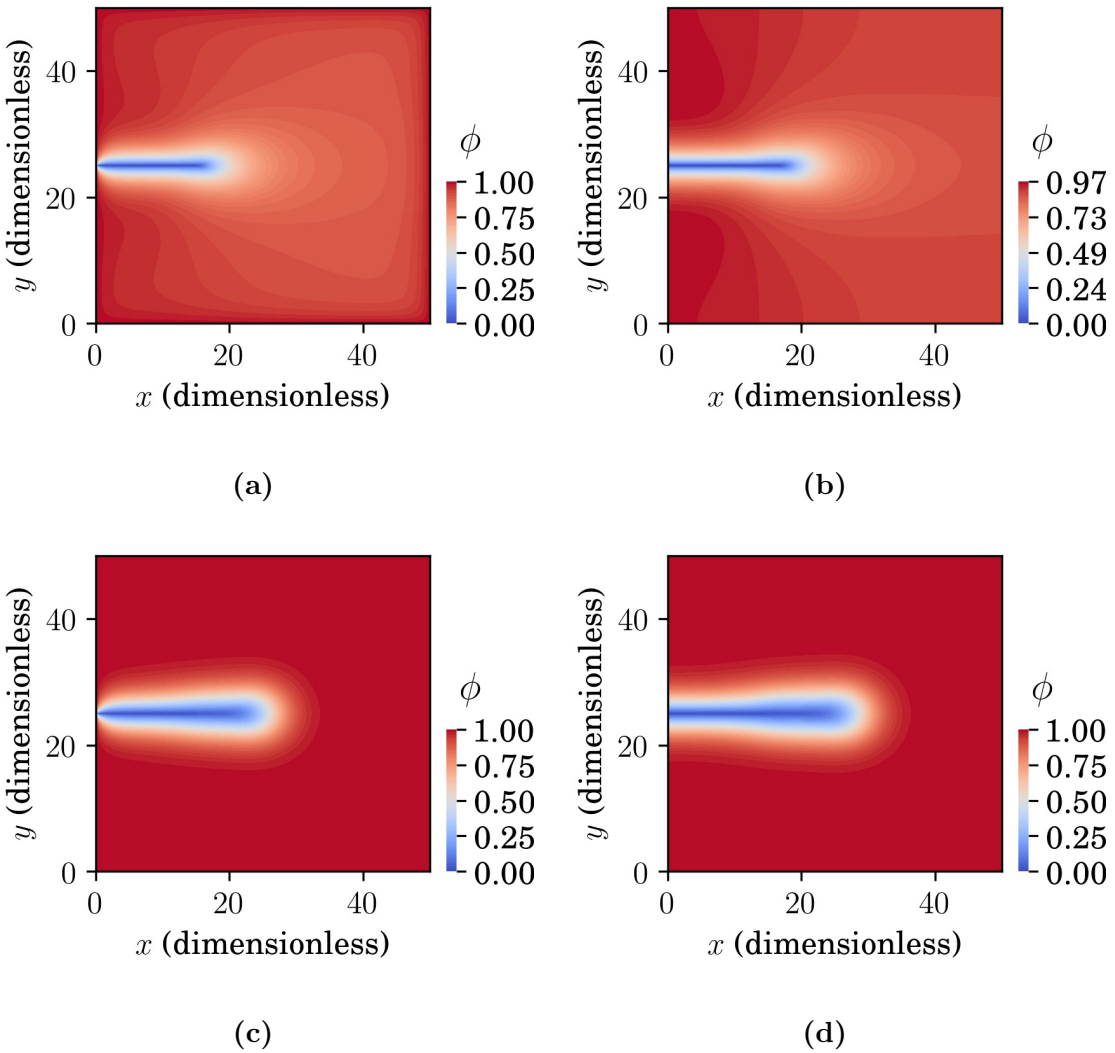

Figure 4.3: ϕ profiles with two boundary conditions in both models. (a) and (b) are for Dirichlet condition and zero-flux condition in the mechanical model. (c) and (d) are for Dirichlet condition and zero-flux condition in the KKL model.

Chapter 5

Benchmarking

5.1 Sensitivity Analysis of the Threshold Values in the Iteration Methods

Two threshold values, i.e., the threshold values for the phase-field parameter ($\Delta\phi_{threshold}$) and the displacement field ($\Delta u_{threshold}$), are introduced in the iteration methods. To determine their values, 1D quasi-static simulations were performed. In the simulations, C, which is Young's modulus in 1D, was set to 1, and the length of the elastic band (L) was set to 50. Three mesh sizes were investigated, i.e., 0.01, 0.05 and 0.1. The values of the rest of the parameters are given in Table 4.1.

At first, simulations were carried out with the mesh size set to 0.1. To determine the threshold values more efficiently, one threshold value was evaluated at a time by only solving one of the governing equations. For $\Delta\phi_{threshold}$, only the phase-field equation was solved, and the displacement was set to 0. By comparing the phase-field profiles with the analytical solutions (Equations (2.10) and (2.33)), $\Delta\phi_{threshold}$ can be determined. As shown in Figures 5.1a and 5.1c, the phase-field profiles converge to the analytical solutions when $\Delta\phi_{threshold}$ is below 10^{-5} for both models. Similarly, by only solving the mechanical equilibrium equation while fixing the phase-field profile, the appropriate value of $\Delta u_{threshold}$ is determined. As shown in Figures 5.1b and 5.1d, the stress curves converge when $\Delta u_{threshold}$ is below 10^{-7} for both models.

Then the threshold values were evaluated with different mesh sizes. As shown in Figure 5.2, the threshold values decrease when reducing the mesh size. One possible explanation is that by decreasing the mesh size, the resolution increases. Hence, much higher accuracy is required to match all the grid-point values between the current and previous iteration.

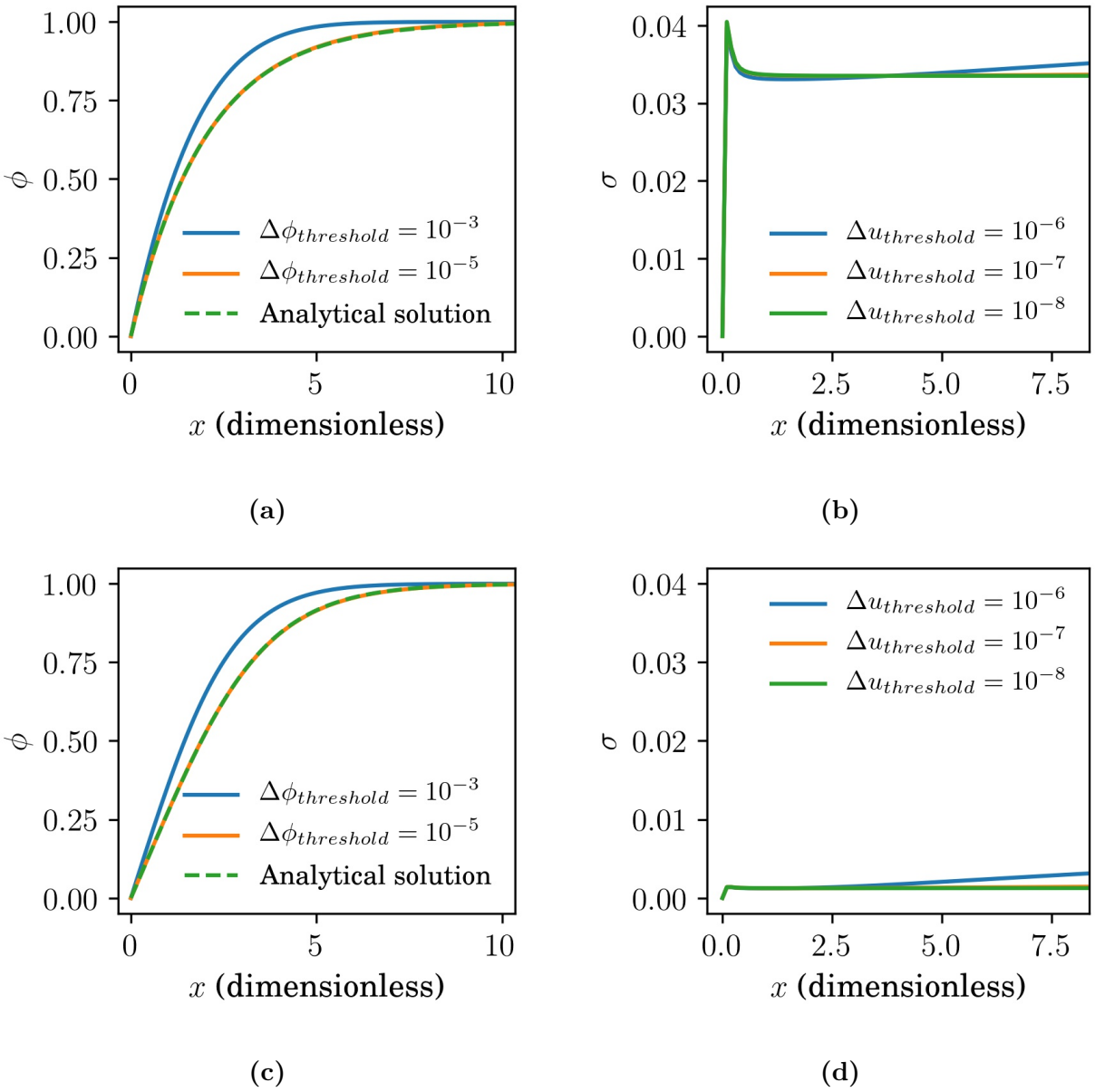

Figure 5.1: Crack interface profiles and stress distributions in 1D simulations with different $\phi_{threshold}$ and $u_{threshold}$ in both models. (a) and (b) are for the mechanical model. (c) and (d) are for the KKL model. All the profiles are plotted based on the right half of the 1D elastic band, so $x = 0$ indicates the middle of the band.

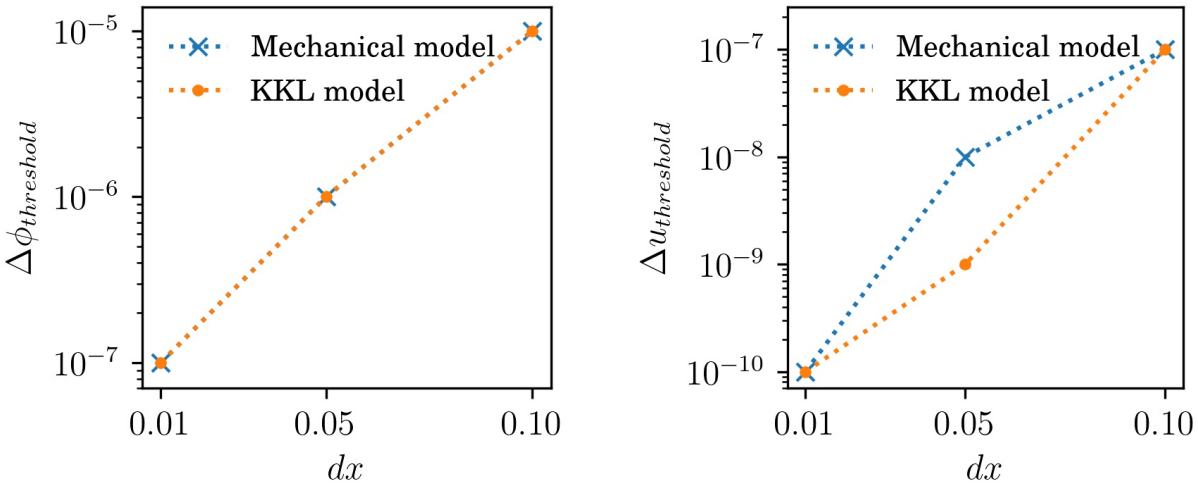

Figure 5.2: (a) Critical $\Delta\phi_{threshold}$ and (b) critical $\Delta u_{threshold}$ for the results to converge under different mesh sizes in the mechanical and the KKL model. Markers represent the data points.

5.2 Sensitivity Analysis of the Mesh Size

The mesh size does not only affect the threshold values in the iteration methods but also the accuracy of the numerical solutions. Although a few grid points inside the crack interface are sufficient to have a smooth interface profile, much finer meshes are essential to accurately capture the discontinuous displacement inside the crack. To determine the mesh size, 1D quasi-static simulations with various mesh sizes were carried out. According to Bourdin et al. [45], the non-zero mesh size results in the overestimation of the critical energy release rate by a factor of $1 + dx/4l$ in the mechanical model. Therefore, since l was 1 in the simulations, only the mesh sizes below 0.1 were investigated to ensure the accuracy of the critical energy release rate. Figure 5.3 compares the phase-field and stress profiles for different mesh sizes in both models. The analytical stresses for both models are 0 since all the tension is released after the breakage of the elastic band. With the decrease of the mesh size, the phase-field and the stress profiles become closer to the analytical solutions. Even though the stresses do not become 0, they are below 0.07% of the initial value, which is negligible. The mesh size seems to have a small influence on 1D solutions. However, it might not be the case in 2D as

the stress ahead of the crack tip becomes higher.

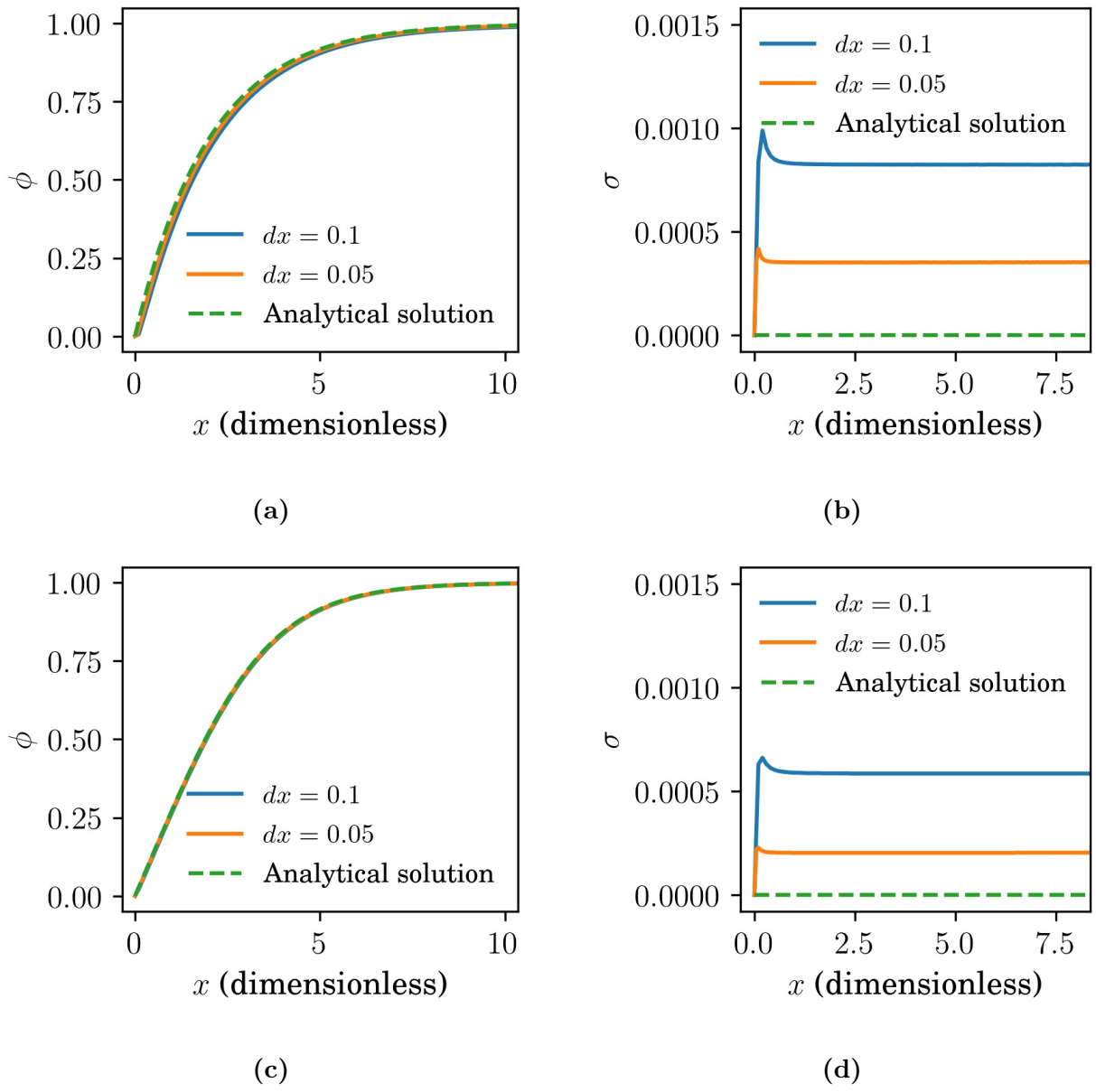

Figure 5.3: Crack interface profiles and stress distributions in 1D simulations with different mesh sizes in both models. (a) and (b) are for the mechanical model. (c) and (d) are for the KKL model. All the profiles are plotted based on the right half of the 1D elastic band.

Due to the high computational cost, only two mesh sizes, i.e., $dx = 0.08$ and $dx = 0.1$, were investigated in 2D quasi-static simulations. The values of the rest of the parameters

can be found in Table 4.1. Since there are two shear stresses, i.e., $\partial u/\partial x$ and $\partial u/\partial y$, in 2D, to simplify the analysis, the elastic energy was analyzed instead. The phase-field and elastic energy profiles along the dotted line in Figure 5.4 for two mesh sizes were then compared. Since the profiles along the dotted line will be studied extensively in the later chapters, they are referred to as the profiles in the crack plane. As shown in Figure 5.5, negligible differences were observed when varying the mesh size. However, the computational cost becomes significantly higher with dx equal to 0.08, which hinders investigations into the mesh size below that value. Therefore, dx was set to 0.1 in the quasi-static simulations.

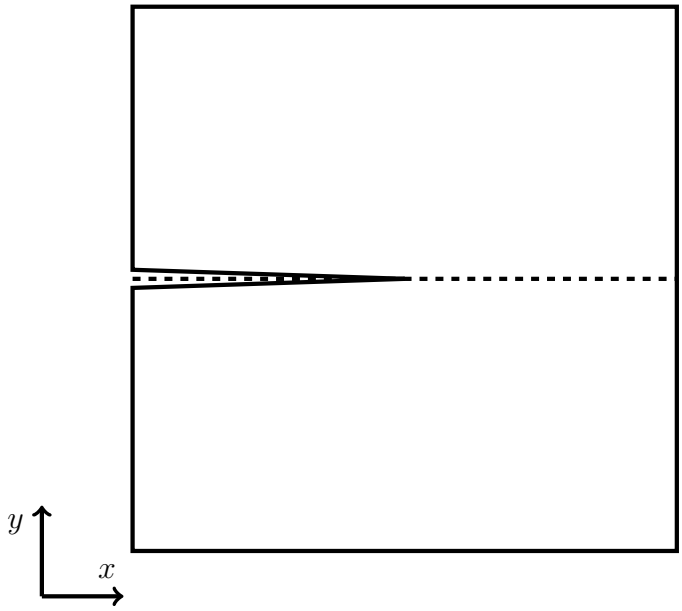

Figure 5.4: The schematic representation of the simulation domain in 2D. The dotted line lies in the crack plane along the x-direction.

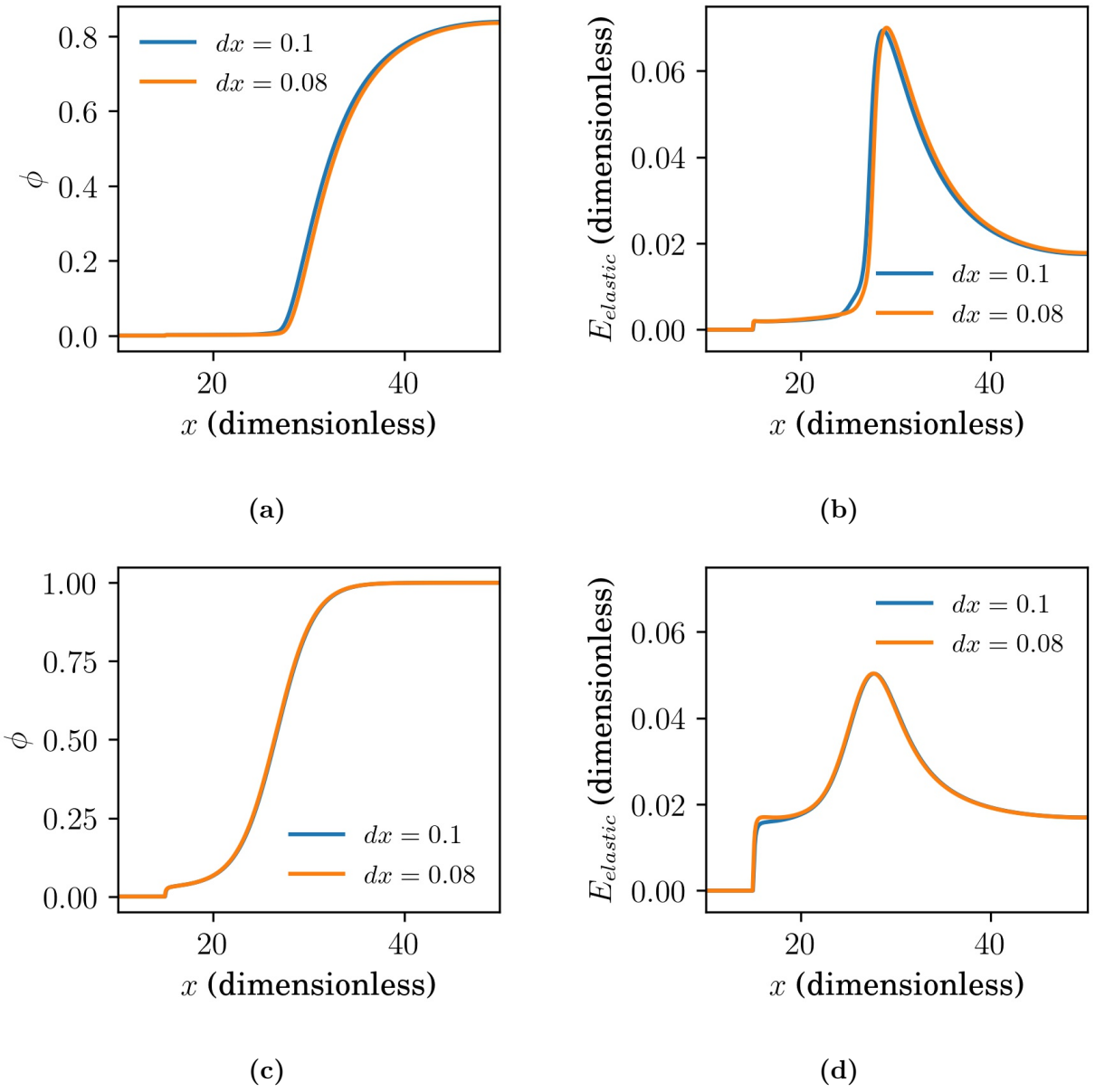

Figure 5.5: ϕ profiles and elastic energy profiles in the crack plane with different mesh sizes in both models. (a) and (b) are for the mechanical model. (c) and (d) are for the KKL model.

5.3 Sensitivity Analysis of the Time Step Size

Similar to the non-zero mesh size, the non-zero time step size (dt) in the displacement equation also leads to the discretization error. Therefore, 2D dynamic simulations with various time step sizes were performed. Apart from the parameters used in the 2D quasi-static sim-

ulations (Table 4.1), the density of the material (ρ) was set to 1. As shown in Figure 5.6, in both models, the crack profiles converge when dt is below 0.06, and the elastic energy profiles in the crack plane overlap when dt is below 0.02. Therefore, dt was set to 0.02 in dynamic simulations.

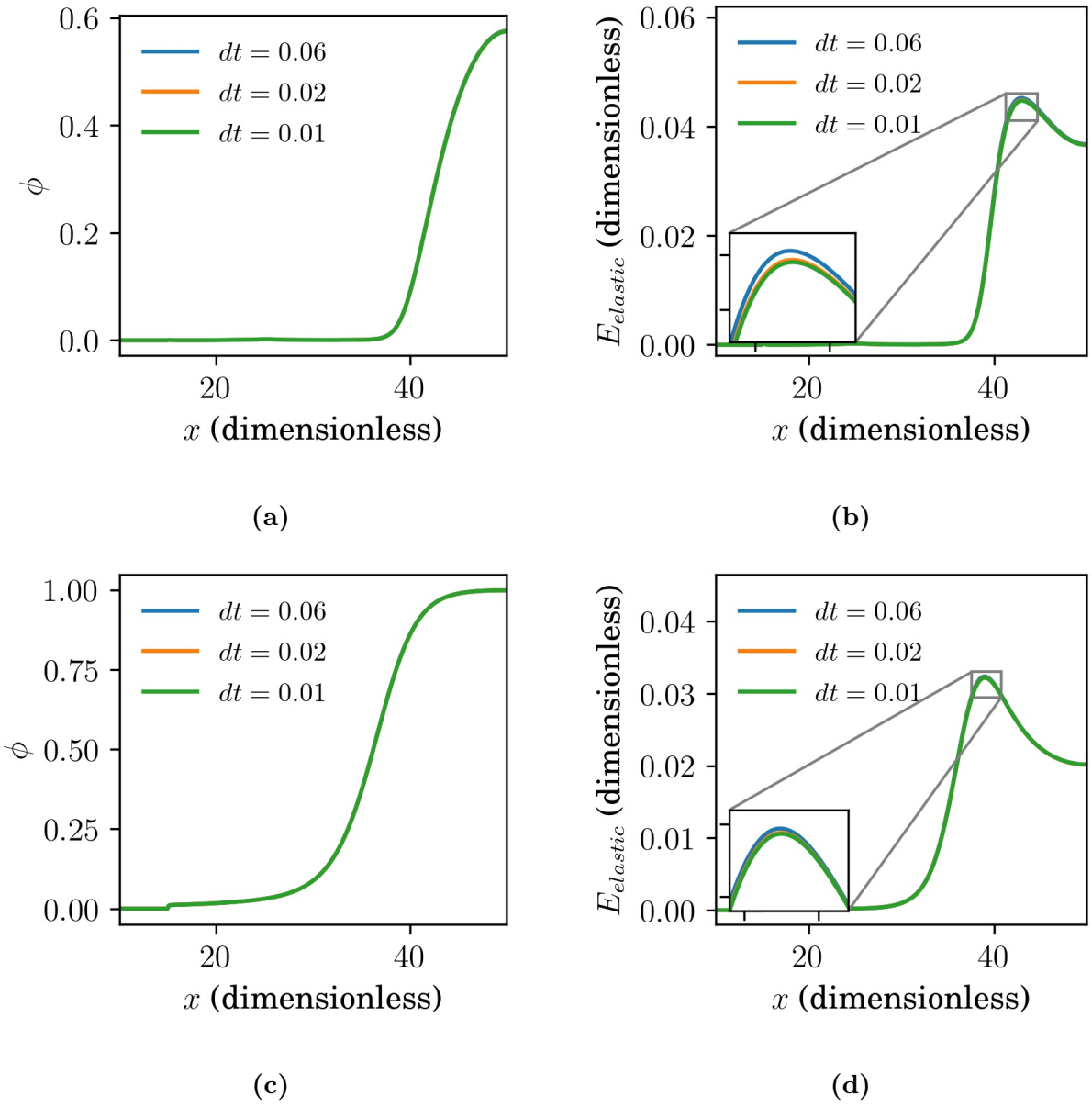

Figure 5.6: ϕ profiles and elastic energy profiles in the crack plane with different time step sizes in both models. (a) and (b) are for the mechanical model. (c) and (d) are for the KKL model.

5.4 Sensitivity Analysis of the Crack Front Position

Distinct from the sharp interface models where the interface position is definite, in phase-field models, the crack interface distributes over a narrow band of which the width is the interface thickness (δ). As a result, the crack front position varies with the value of ϕ, which is referred to as ϕ_{front} in the current work. The uncertainty of the crack front position leads to difficulty in capturing the energy release rate, crack velocity, and branching angle. Therefore, 2D quasi-static and dynamic simulations were carried out to determine the value of ϕ_{front}. Since $\phi = 0$ represents the crack, ϕ_{front} should be close to 0 to represent the position of the crack tip. Therefore, only the ϕ_{front} below 0.5 was analyzed.

5.4.1 ϕ_{front} in the Quasi-static Setting

According to Equation (2.1), the energy release rate can be calculated from the elastic energy of the system and the crack propagation length. Similarly, the surface energy of the system and the propagation length are required to determine the critical energy release rate. Since ϕ_{front} affects the propagation length, it could potentially influence these two parameters. Therefore, 2D quasi-static simulations were performed to evaluate the influence of ϕ_{front} on the energy release rate and the critical energy release rate. The parameters are given in Table 4.1.

Figure 5.7 compares the energy of the system with respect to the crack propagation length with different ϕ_{front}. In almost all the cases except the one with $\phi_{front} = 0.1$ in the KKL model, the slopes of the elastic energy and surface energy curves change abruptly in the beginning.

For the mechanical model, the abrupt transition can be attributed to two factors. The first is that the initial phase-field profile, which is the analytical solution, is unstable. As shown in Figure 5.8a, the crack interface profile quickly stabilizes and deviates from the analytical solution after the first computational loop. Meanwhile, the surface energy and the elastic energy transit to the stable regime where the slopes of the curves stabilize. The other reason is that the position of $\phi_{front} = 0.1$ lags behind that of $\phi_{front} = 0.5$ as shown in Figure 5.8b, which also leads to the larger surface energy increment and elastic energy release in the case with $\phi_{front} = 0.1$ (Figure 5.7a). Especially in the first few loops, after the same amount of elastic energy release and surface energy increment, with ϕ_{front} set to 0.1, the almost zero propagation length leads to larger energy gradients at the beginning.

As in the mechanical model, in the KKL model, with ϕ_{front} set to 0.1, the abrupt transition

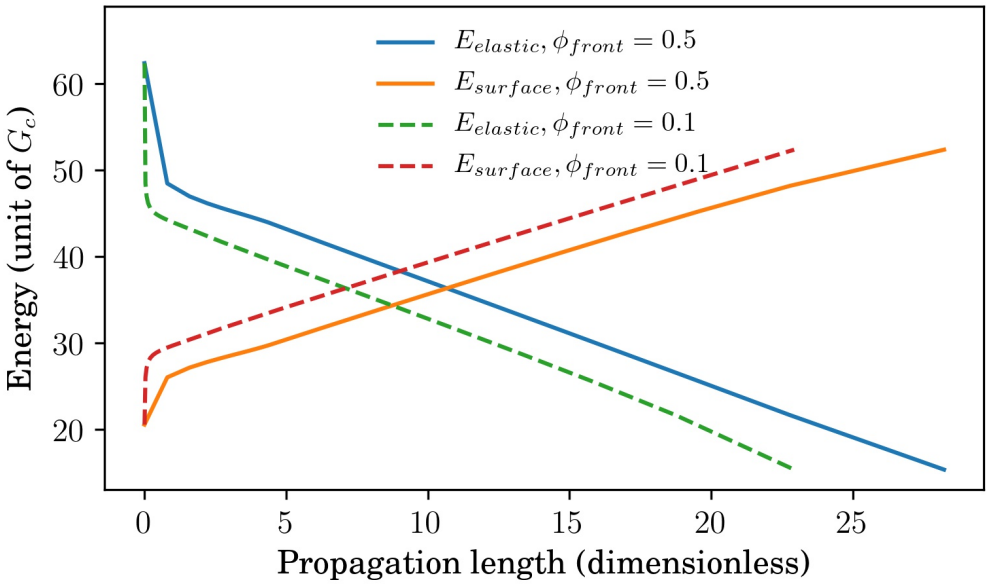

(a)

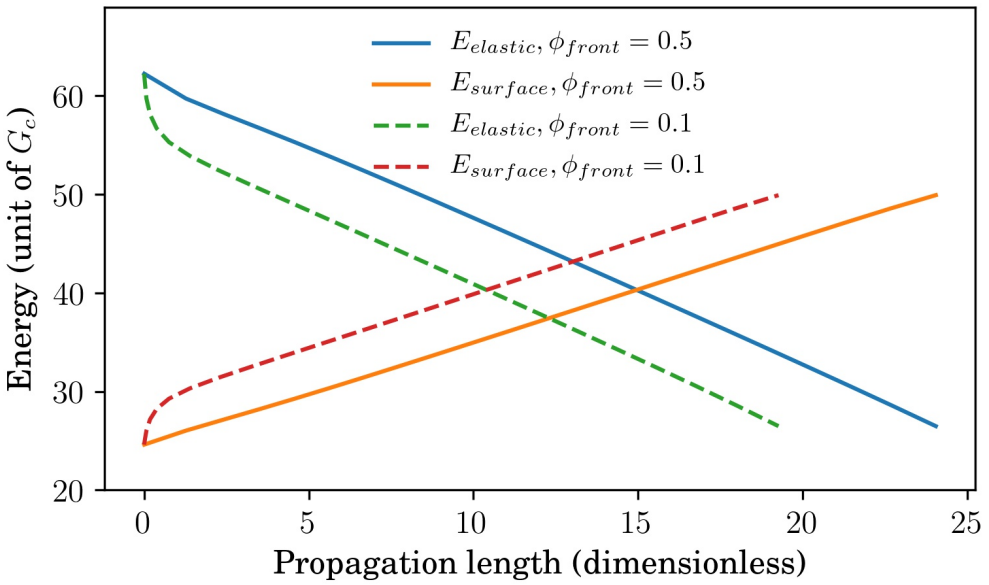

(b)

Figure 5.7: Elastic energy release and surface energy increment with respect to the crack propagation length for (a) the mechanical model and (b) the KKL model with different ϕ_{front}.

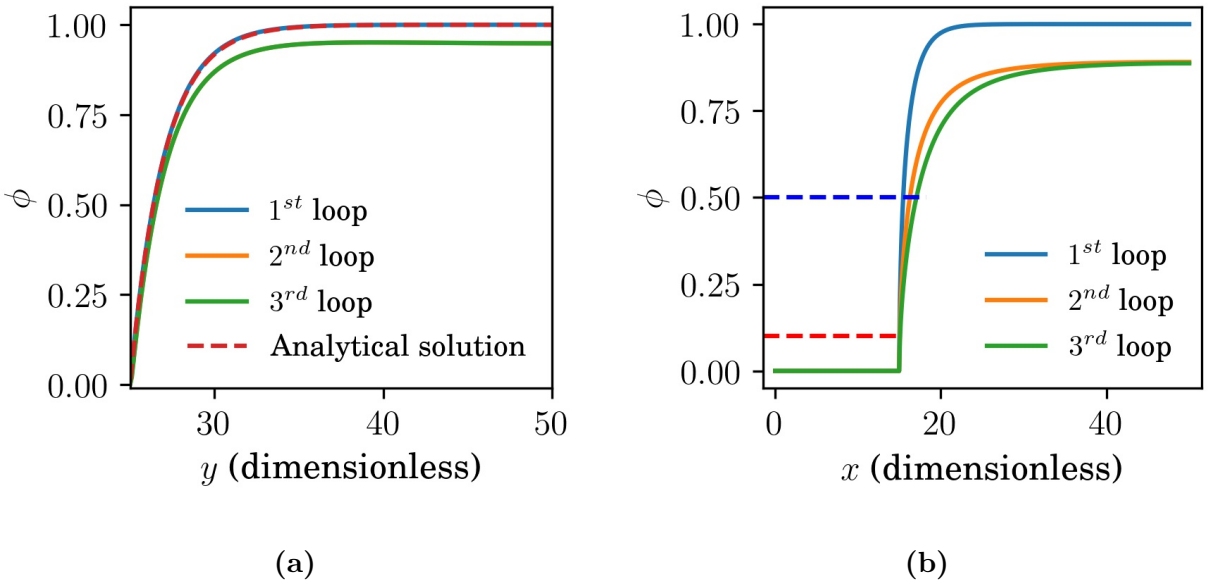

Figure 5.8: ϕ profiles (a) at the right half of the interface and (b) in the crack plane in the first few computational loops in the mechanical model. The blue and the red dotted line in (b) correspond to the crack front position with ϕ_{front} set to 0.5 and 0.1.

in the energy curves occurs because the position of $\phi_{front} = 0.1$ lags behind that of $\phi_{front} = 0.5$ (Figure 5.9b). For the case with $\phi_{front} = 0.5$, the energy curves are linear (Figure 5.7b) because the crack interface profile does not change abruptly in the first few computational loops as shown in Figure 5.9a.

In both models, the initially unstable regime is sensitive to ϕ_{front}. As a result, at the same crack propagation length, the energy varies with ϕ_{front}. However, in both models, the slopes of the energy curves in the stable regime do not change with ϕ_{front} (Figure 5.7). Since the slopes of the elastic energy and surface energy curve represent the energy release rate and the critical energy release rate, they are much more important than the total amount of energy in the system. By neglecting the initially unstable regime and only focusing on the slopes at the stable regime, the results are insensitive to ϕ_{front}. Therefore, ϕ_{front} was set to 0.5 in quasi-static simulations as it results in linear energy curves in the KKL model.

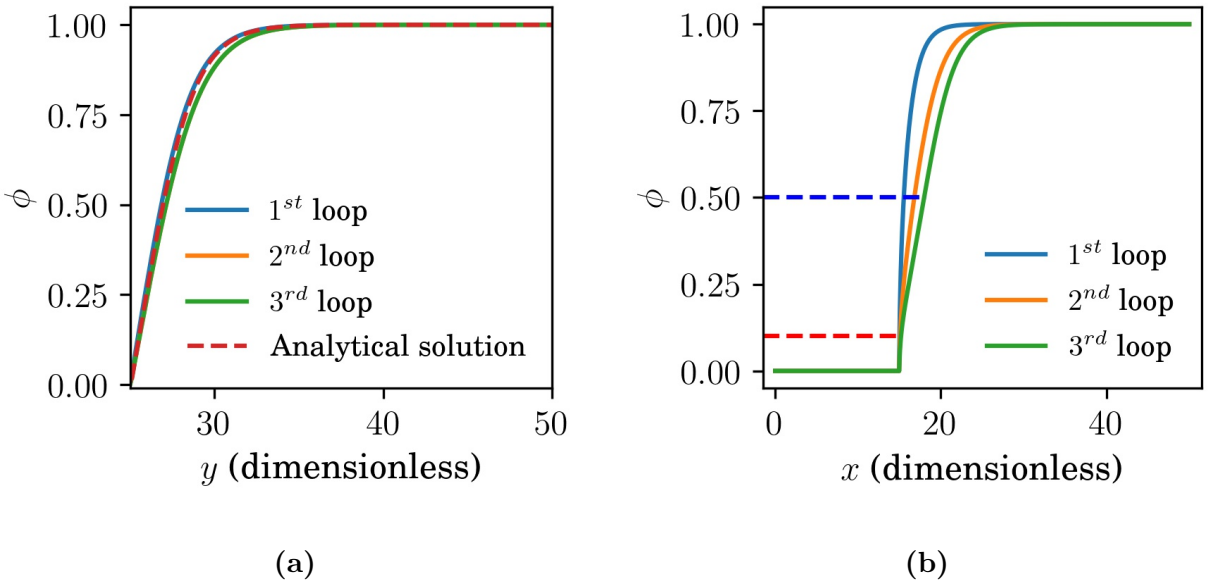

Figure 5.9: ϕ profiles (a) at the right half of the interface and (b) in the crack plane in the first few computational loops in the KKL model. The blue and the red dotted line in (b) correspond to the crack front position with ϕ_{front} set to 0.5 and 0.1.

5.4.2 ϕ_{front} in the Dynamic Setting

As in the quasi-static case, ϕ_{front} can also affect the dynamic fracture phenomena. In the literature, some people argued that the crack velocity and branching angle cannot be determined accurately because of the diffuse interface in the phase-field models. However, ϕ_{front} was set to 0.5 by Karma and Lobkovsky [35] to calculate the velocity and branching angle. Therefore, to examine the influence of ϕ_{front} on the crack velocity and branching angle, 2D dynamic simulations were carried out. The geometry parameters are listed in Table 5.1. The density (ρ) was set to 1, the time step size (dt) was set to 0.02, and the rest of the material parameters can be found in Table 4.1.

Figures 5.10a and 5.10c compare the crack velocity with respect to the crack tip position with different ϕ_{front}. The unit of the crack velocity is the shear wave speed (C_s), which equals $\sqrt{\mu/\rho}$. All the curves predict the same trend: the crack velocity increases then decreases during blunting and becomes unstable after branching. The velocity oscillation after branching is commonly observed in experiments, which is related to the interaction of the microcracks at the crack tip. With the decrease of ϕ_{front}, the velocity becomes lower in

Table 5.1: Geometry parameters in 2D dynamic simulations

Symbol	Parameter	Value
L_x	Length of the 2D sheet	120
L_y	Width of the 2D sheet	120
l_c	Length of the initial crack	50

both models, which is because the slope of the line at the crack front (ab) decreases during crack propagation as shown in Figures 5.10b and 5.10d. Therefore, the rotation of the line ab adds the additional angular velocity. Meanwhile, the velocity curves shift leftwards when decreasing ϕ_{front} as the position of the smaller ϕ_{front} lags behind that of the larger ϕ_{front}. As for the branching velocity, which is indicated by the dotted lines in Figures 5.10a and 5.10c, when varying ϕ_{front} from 0.5 to 0.1, it decreases by 20% in the mechanical model and 9% in the KKL model. Compared with the KKL model, the branching velocity in the mechanical model is sensitive to ϕ_{front}. Therefore, when analyzing the branching velocity in the mechanical model, the 20% error induced by ϕ_{front} should be taken into consideration.

Another noticeable feature in the velocity curves is that the velocity increases abruptly immediately after branching, which is because of the way the velocity is calculated. Here, the crack tip position is defined as the point with the maximum x-axis value in the contour line of $\phi = \phi_{front}$. With this definition, the critical time for crack bifurcation is when the number of points with the maximum x-axis value changes from one to two. However, with this method, immediately after branching, significant errors occur in the velocity calculation. As shown in Figure 5.11, at the moment of branching, the crack tip position changes from a to b or c. As a result, the sudden increase in the y coordinate of the crack tip position leads to a major increase in the velocity, which is a numerical artifact.

The diffuse interface also leads to the problem of defining the branching angle. Figure 5.12 compares the contour lines of $\phi = \phi_{front}$. Since the branches are not thin lines, the actual branching angle cannot be extracted from the contour directly. The most straightforward way is to select lines inside the branches and view the angle between the selected lines as the branching angle. Here, the line is selected visually such that the branch is almost symmetric with it. With this method, the branching angle increases 8° in the mechanical model and decreases 2° in the KKL model when varying ϕ_{front} from 0.1 to 0.5. Considering the error introduced when selecting the lines, the branching angle in both models is insensitive to

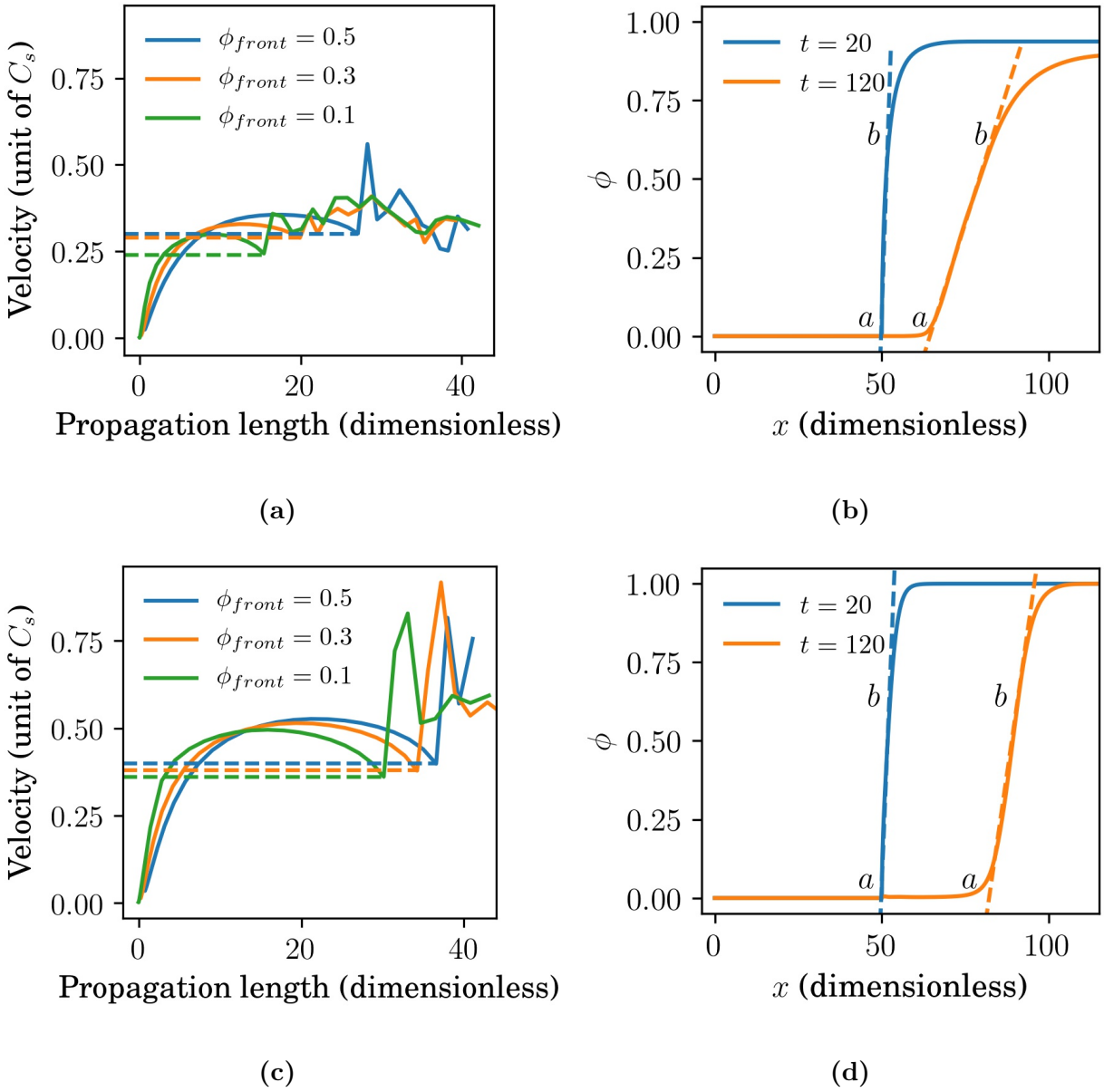

Figure 5.10: Crack velocity with respect to the propagation length with different ϕ_{front} for (a) the mechanical model and (c) the KKL model. Phase-field profiles in the crack plane at different times for (b) the mechanical model and (d) the KKL model. The dotted lines in (a) and (c) indicate the branching velocities.

ϕ_{front}. To be consistent with the work by Karma and Lobkovsky [35], ϕ_{front} was set to 0.5 in dynamic simulations.

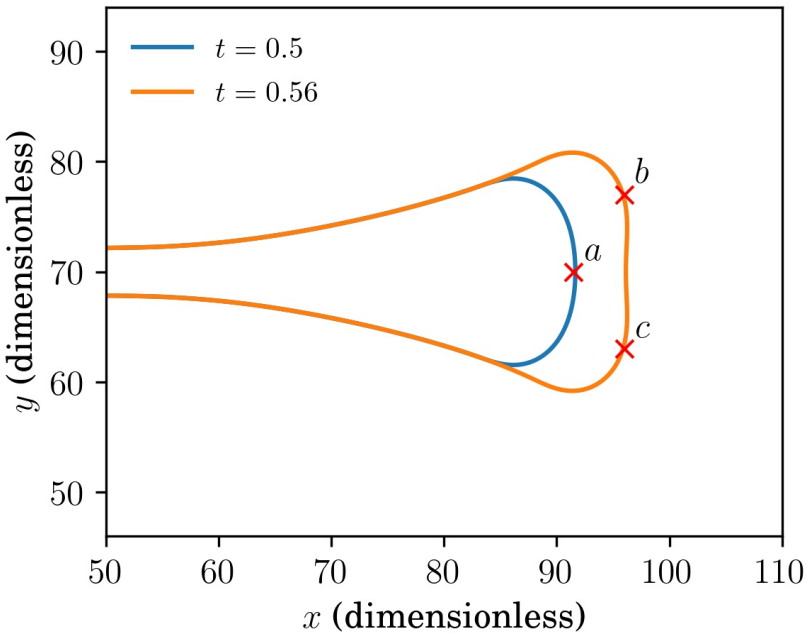

Figure 5.11: The contour line of $\phi = 0.5$ in the KKL model. a, b and c are the points indicating the crack tip.

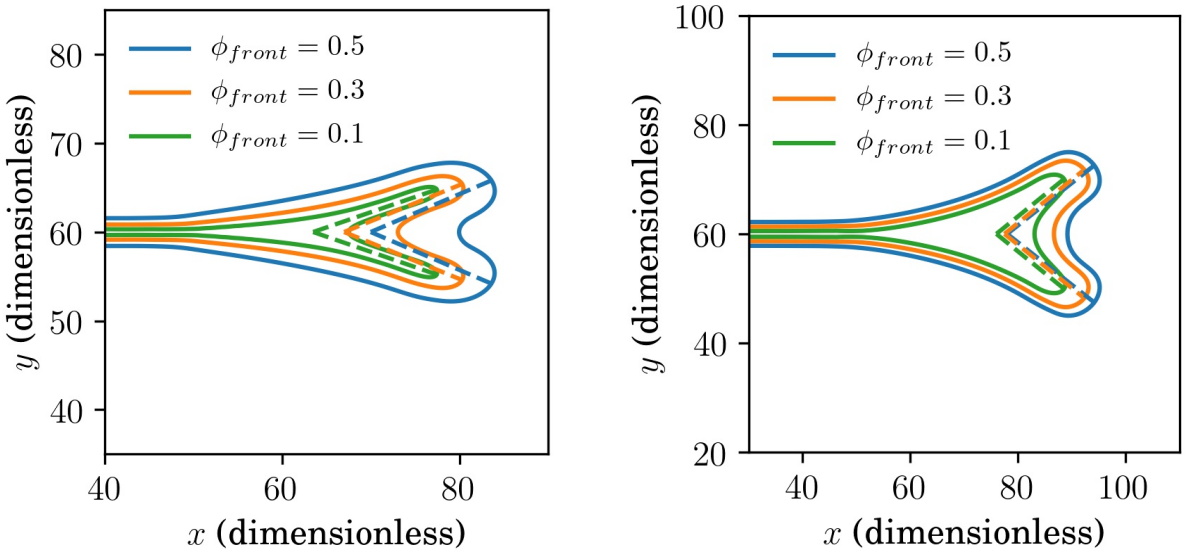

(a) **(b)**

Figure 5.12: Contour lines of $\phi = \phi_{front}$ for (a) the mechanical model and (b) the KKL model.

5.5 Sensitivity Analysis of the Geometric Configuration in the Quasi-static Setting

The geometric configuration refers to the crack length, domain width, and domain length. In dynamic fracture, the radiated elastic wave from the crack tip can be reflected at the boundaries and interact with the crack. Therefore, to avoid the interaction between the crack and the boundary, the crack length has to be very long. In the quasi-static case, however, this situation does not exist with the mechanical equilibrium condition. Therefore, the crack length was not analyzed in the quasi-static setting.

The domain size, however, does influence the accuracy of the simulations. As mentioned in Chapter 2, in both the mechanical model and the KKL model, the interface thickness to domain size ratio has to be very small to obtain good agreement with either the Griffith theory or the experimental results. Since varying the interface thickness requires the adjustment of the mesh size, only the domain size was analyzed. Therefore, to determine the domain size, 2D quasi-static simulations were performed. Square domains were used in the simulations, and two domain lengths, i.e., 50 and 100, were investigated. In case the initial crack length influences the results, the initial crack length to domain size ratio was kept constant when varying the domain size. The rest of the parameters are listed in Table 4.1.

Figure 5.13 compares the elastic energy and surface energy with respect to the propagation length with different domain sizes. In both models, with the increase of the domain size, the elastic energy and the surface energy curves shift upwards. For the elastic energy, that is caused by the difference in the initial elastic energy in the system. Although E_{in} is the same with different domain sizes, according to Equation (4.11), it only accounts for the input energy in the y-direction (width direction). Therefore, considering that the length of the domain is different, the initial elastic energy in the system is higher with a larger domain size. The difference in the initial surface energy is because the initial crack length also varies with the domain size. However, neither the elastic energy nor the surface energy affects crack propagation.

On the contrary, the energy release rate and critical energy release rate, which can be calculated from the slopes of the elastic energy and surface energy curves in the stable regime, determine the crack propagation behaviour. In the mechanical model, when reducing the domain size by half, the energy release rate and critical energy release rate decrease by 7.7% and 9.6% (Figure 5.13a). While in the KKL model, these two parameters do not vary with the domain size (Figure 5.13b). In the mechanical model, ideally, larger domain sizes should

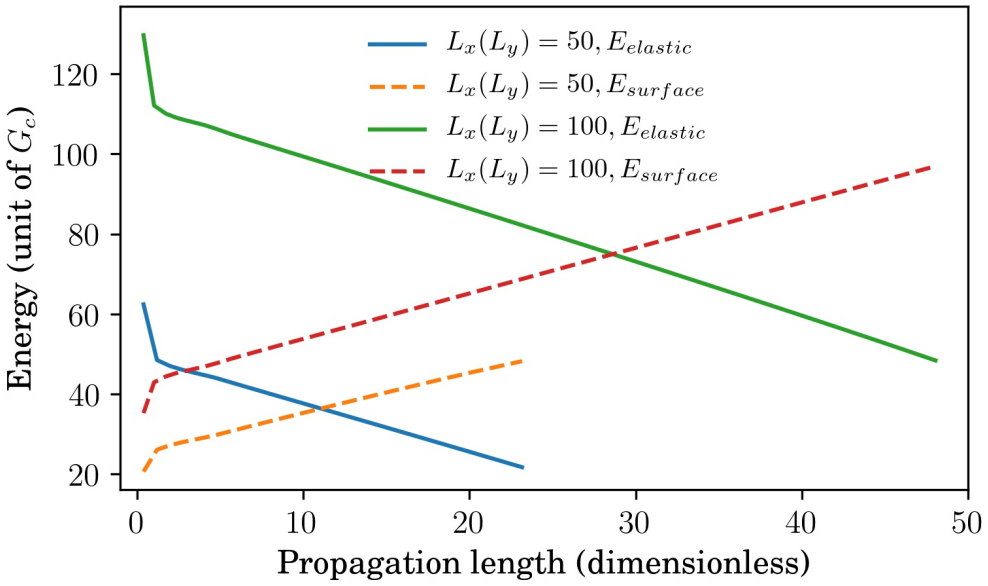

(a)

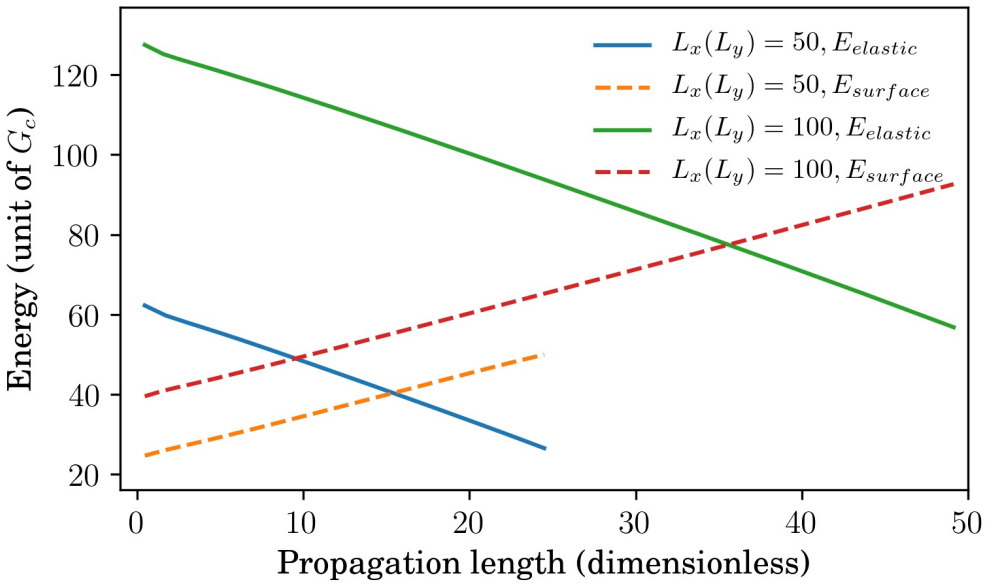

(b)

Figure 5.13: Elastic energy release and surface energy increment with respect to the crack propagation length for (a) the mechanical model and (b) the KKL model with different domain sizes.

be investigated until the results converge. However, since the computational cost becomes significantly higher even by setting the domain size to 100, the smaller domain size, i.e., 50, was adopted in the following quasi-static simulations.

5.6 Sensitivity Analysis of the Geometric Configuration in the Dynamic Setting

In dynamic fracture, the geometric configuration is even more important than that in quasi-static fracture as the elastic wave can interact with the crack and lead to distinct fracture phenomena. In fracture theories, since it is impossible to consider all the scenarios, more generalized and simplified settings are usually adopted. In these settings, some assumptions, e.g., infinite large domain and semi-infinite crack, seem impractical in experiments. Under certain conditions, however, the theoretical predictions can be treated as the asymptotic solutions of the experimental results.

There are two settings commonly adopted in fracture theories: a crack in an infinite domain where the boundaries do not affect the crack tip fields, and a semi-infinite crack in an infinitely long strip where only the boundaries in the width direction affect the crack fields. Adda-Bedia [5] studied the dynamic fracture phenomena in 2D considering a semi-infinite crack in an infinitely long strip under antiplane shear condition. Therefore, 2D dynamic simulations were carried out to make the simulation setting equivalent to that in Adda-Bedia's theory. In the simulations, the density (ρ) was set to 1, the time step size (dt) was set to 0.02, and the rest of the material parameters can be found in Table 4.1.

5.6.1 Initial Crack Length

Since having a semi-infinite crack is impossible in the simulations, analysis has to be made before selecting the initial crack length. In the simulations, different crack lengths were analyzed. The domain width and length were set to 120. Figure 5.14 compares the crack velocity with different initial crack lengths in both models. All the curves converge before the propagation length is 20. However, the curves diverge in the later stage as the crack tip fields start interacting with the right boundary. Since the velocities are the same with different l_c in the early stage, l_c was set to 50.

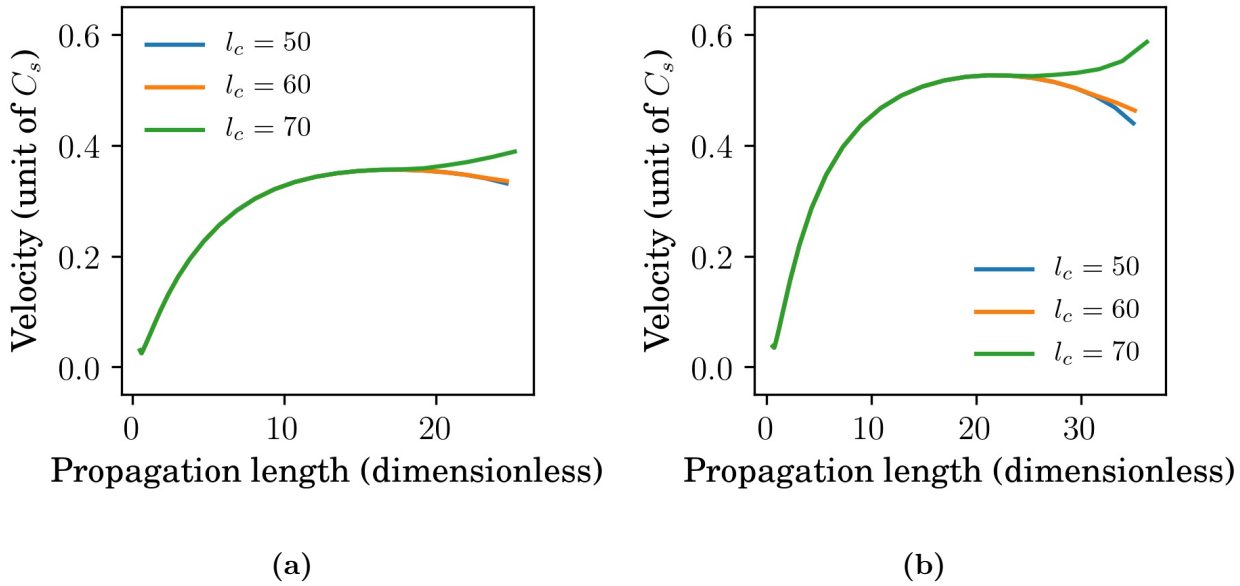

Figure 5.14: Crack velocity with respect to the propagation length with different initial crack lengths for (a) the mechanical model and (b) the KKL model.

5.6.2 Domain Length

In Adda-Bedia's theory, the domain length was assumed to be infinitely long, which is impractical in the phase-field simulations. Therefore, to determine the proper range of the domain length, 2D dynamic simulations were carried out. In the simulations, the domain width and the initial crack length were set to 120 and 50. Figure 5.15 compares the crack velocity with different domain lengths in both models. In all the cases, the spike in the velocity curves is the numerical artifact caused by the method calculating the velocity, which has been demonstrated in Section 5.4. When the domain length is above 120, the velocity curves converge. Therefore, L_x was set to 160.

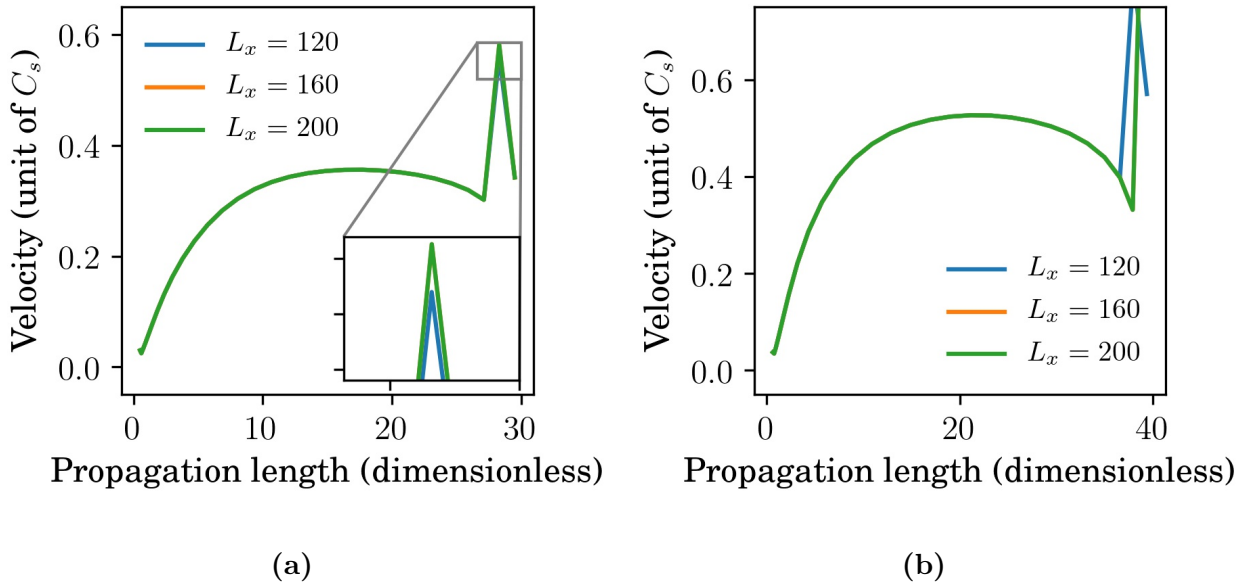

Figure 5.15: Crack velocity with respect to the propagation length with different domain lengths for (a) the mechanical model and (b) the KKL model.

5.6.3 Domain Width

The last geometry parameter to be determined is the domain width. Distinct from the other two parameters, the domain width is unspecified in the fracture theory. However, both the mechanical model and the KKL model require the use of a large domain width to increase the accuracy. Therefore, 2D dynamic simulations were carried out to determine the domain width. According to Knauss [107], in experiments and simulations, the relative size of the initial crack length with respect to the domain width has to be large to approximate the semi-infinite crack in theories. Therefore, to avoid varying the relative size of the crack length when increasing the domain width, the ratio of the initial crack length to domain width to domain length was kept constant. The geometry parameters for the simulations are listed in Table 5.2.

Figure 5.16 compares the crack velocity with different values of the domain width. With the increase of the domain width, the crack velocity decreases in both models, which is consistent with the observations by Henry [98]. When varying L_y from 120 to 160, in maximum, the velocity decreases by 5.7% in the mechanical model and 5.8% in the KKL model. Considering that the velocity could vary by up to 20% with different ϕ_{front} as demonstrated in Section 5.4, the change in the crack velocity with different domain widths is negligible.

Table 5.2: Geometry parameters for three cases

Case	Domain length (L_x)	Domain width (L_y)	Initial crack length (l_c)
1	160	120	50
2	186	140	58.3
3	213	160	66.7

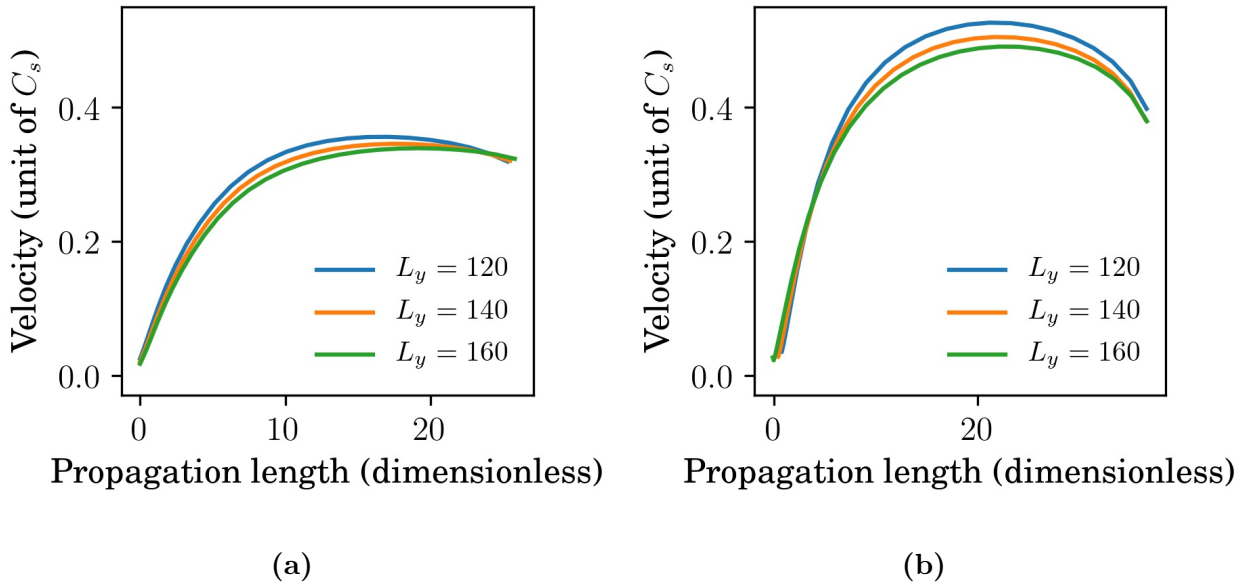

Figure 5.16: Crack velocity with respect to the propagation lengths with different domain widths for (a) the mechanical model and (b) the KKL model.

Figure 5.17 compares the branching angle with different domain widths in both models. When increasing the domain width from 140 to 160, the branching angle only increases 5° in the mechanical model. Considering the error induced from selecting the dotted lines in Figure 5.17a, the increase in the branching angle is negligible. In the KKL model, the contour lines converge when the domain width is above 140 as shown in Figure 5.17b. Therefore, to have an accurate representation of the crack shape with relatively lower computational cost, L_y was set to 140, and the geometry parameters of case 2 in Table 5.2 were used in dynamic simulations.

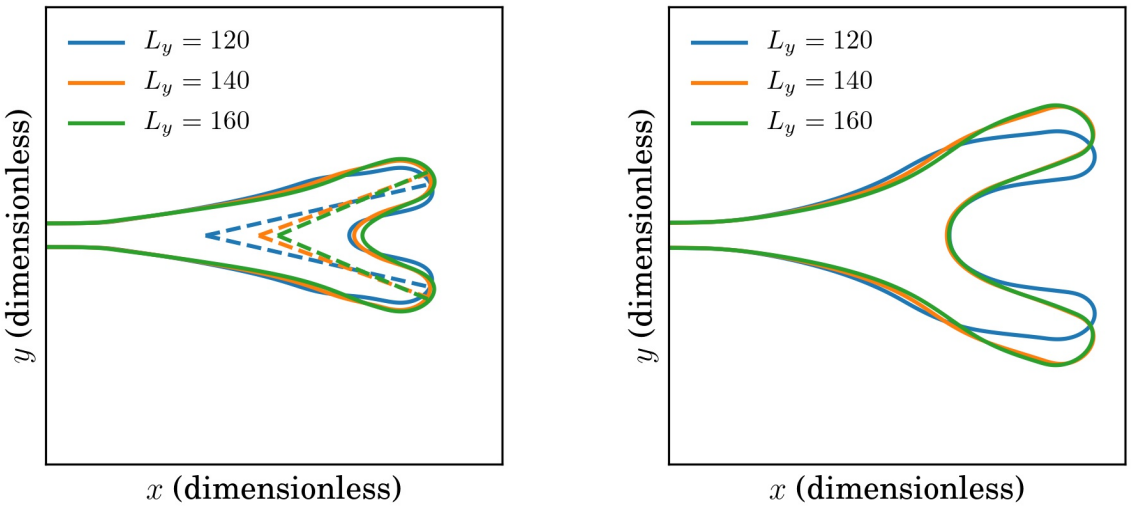

Figure 5.17: Contour lines of $\phi = 0.5$ with different domain widths for (a) the mechanical model and (b) the KKL model. The ticks of the x-axis and y-axis are not given as they are different for three cases in order to match the crack shapes. The dotted lines in (a) indicate the branching angles.

Chapter 6

Simulations of Quasi-static Crack Propagation

6.1 Introduction

This chapter focuses on the quasi-static applications of the mechanical model and the KKL model. Utilizing the computer programs in Appendices A and B, general comparisons between the models were first carried out. Then to assess the robustness of the models, some of the material parameters were evaluated. Since crack propagation in heterogeneous materials is a challenging topic, these models were also extended to study crack propagation in a bi-grain system to clarify their abilities in describing the role of the grain boundary during fracture. All the simulations were in 2D, and the values of the parameters used in the simulations can be found in Table 4.1 unless explicitly stated.

6.2 General Comparisons between the Models

6.2.1 Crack Profile

As shown in Figure 6.1a, the major discrepancy in the interface profiles between both models is that ϕ in the bulk is less than 1 in the mechanical model. This is one of the side effects of using the quadratic degradation function (Equation (2.9)), as ϕ can decrease from 1 with any non-zero strain according to Equation (4.2). The phenomenon was referred to as damage accumulation in the literature, which has been discussed in Chapter 2. With higher stress at the crack front region, the effect of damage accumulation becomes more severe. As a result, in the mechanical model, ϕ in the crack front is even lower than that in the bulk as indicated by the red dotted line in Figure 6.1b.

From Figure 6.1b, it is also noticeable that inside the crack, ϕ is non-zero in the KKL model, because of the degradation function (Equation 2.29). The non-zero ϕ also leads to

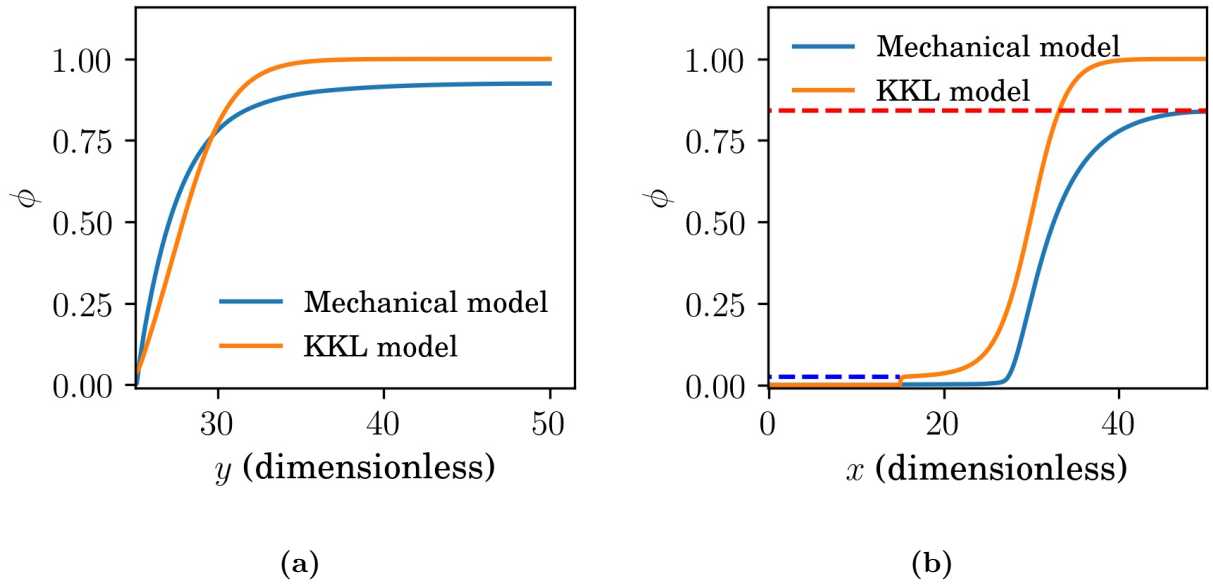

Figure 6.1: (a) Right half of the crack interface profiles and (b) crack profiles in the crack plane for both the mechanical model and the KKL model.

a significant amount of residual elastic energy inside the crack since the elastic energy is sensitive to ϕ. As shown in Figure 6.2, the residual elastic energy in the KKL model is around 30% of the corresponding peak elastic energy. Although there is also residual elastic energy in the mechanical model, but because of the close-to-zero ϕ inside the crack, i.e., around 0.002, the magnitude is negligible. In the literature, some people in the mechanics community suggested setting ϕ to 0 when it is below an imposed threshold value. However, since that approach is not well accepted and may also affect other model outcomes, it was not included in the present work. In conclusion, the KKL model is more accurate in describing the phase-field profiles since it does not have the damage accumulation issue. However, the non-zero ϕ in the KKL model leads to a large residual elastic energy inside the newly developed crack.

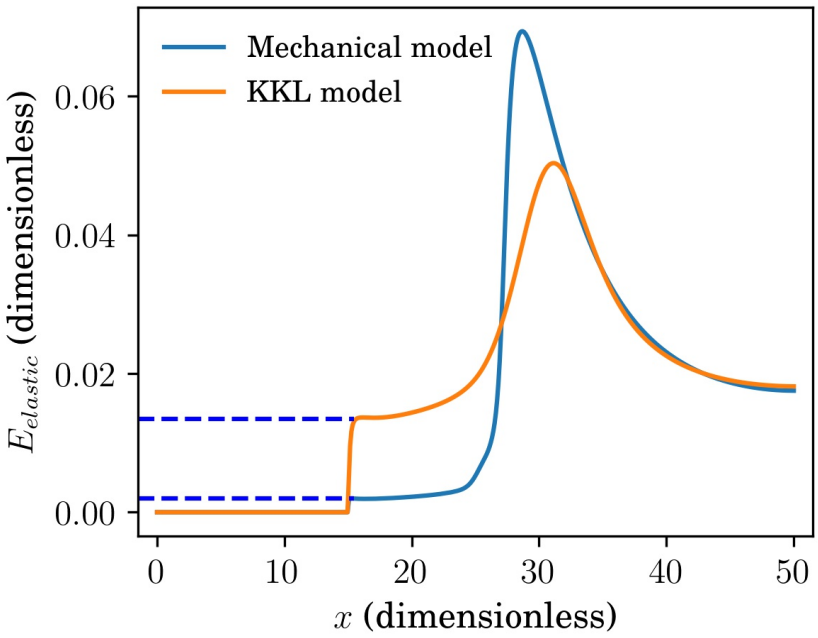

Figure 6.2: Elastic energy profiles in the crack plane for both the mechanical model and the KKL model. The blue dotted lines indicate the residual elastic energy inside the crack.

6.2.2 Stress and Elastic Energy Profiles in the Crack Plane

The crack profile is a numerical feature of the model which may not influence crack propagation. However, it can affect physical features, e.g., stress and elastic energy distribution. In this section, the stress and elastic energy in both models are compared with the analytical solutions.

In 2D mode III fracture, considering a crack in an infinitely large domain, the analytical stress ahead of the crack tip in the crack plane reads [108]:

$$\begin{pmatrix} \sigma_{zx} \\ \sigma_{zy} \end{pmatrix} = \begin{pmatrix} 0 \\ \frac{\sigma_{zy}^{\infty}}{\sqrt{1-(a/x)^2}} \end{pmatrix} \tag{6.1}$$

where σ_{zx} and σ_{zy} are the shear stresses in x direction (propagation direction) and y direction (normal to the propagation direction), a is the crack length, x is the x-coordinate of the stress, and σ_{zy}^{∞} is the stress far away from the crack tip. The analytical stress in other directions can be found in [108]. Since the general stress solution is much more complicated, only the stress distribution in the crack plane was evaluated. In the simulations, σ_{zy}^{∞} is 0.173, and the

crack length (a) was determined from the ϕ profiles.

From simulations, it was observed that σ_{zx} in both models is within a margin of the order of 10^{-5}, which agrees well with the analytical solution, i.e., zero. For σ_{zy}, however, large deviations can be observed in both models as shown in Figure 6.3. Close to the crack tip, because of the diffuse interface, both models cannot capture the stress singularity as predicted by the analytical solution. However, compared with the mechanical model, the KKL model agrees better with the analytical solution near the crack tip. In the KKL model, the small deviation from the analytical solution ahead of the peak stress is because of the boundary effect. Far from the crack tip, the KKL model is almost overlapping with the analytical solution. For the mechanical model, as in the near-tip stress field, the stress is lower than the analytical solution. The lower stress is because ϕ is less than 1 ahead of the crack tip, and the stiffness is a function of ϕ in the phase-field model, i.e., $g(\phi)\mu$. The loss of stiffness in the mechanical model, as a result, underestimates the stress ahead of the crack tip. Therefore, the KKL model is more accurate in describing the stress distribution far from the crack tip.

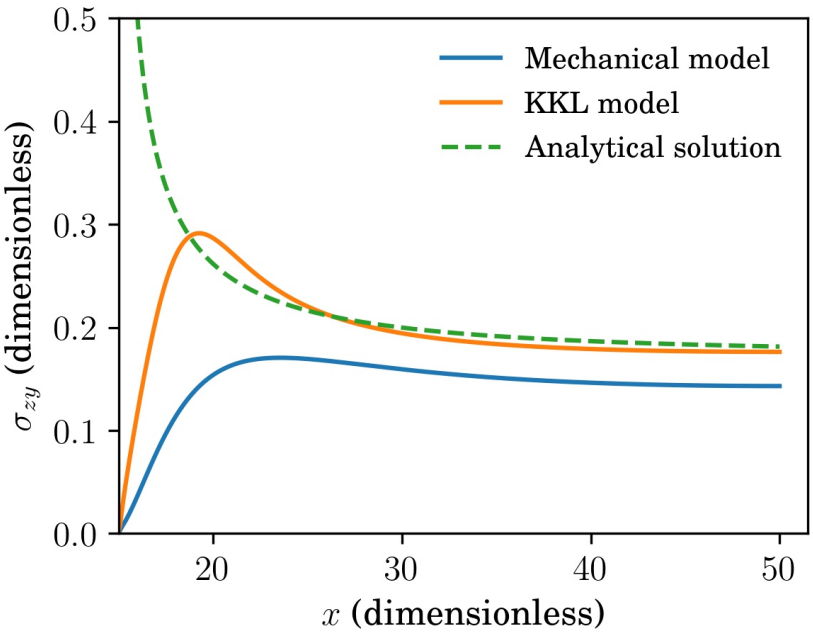

Figure 6.3: The shear stress in the y-direction (σ_{zy}) in the crack plane for both the mechanical model and the KKL model.

The near-tip stress can be captured accurately by neither of the models. The elastic

energy profile in both models, on the contrary, exhibits much better agreement with the analytical solution. With the analytical stress in Equation (6.1), the analytical elastic energy ahead of the crack tip in the crack plane reads:

$$E_{elastic} = \frac{1}{2\mu}\left(\sigma_{zx}^2 + \sigma_{zy}^2\right) = \frac{\left(\sigma_{zy}^{\infty}\right)^2}{2\mu\left(1-(a/x)^2\right)} \tag{6.2}$$

As shown in Figure 6.4, in both models, compared with the stress distribution, the peak elastic energy is much higher than the far-field elastic energy. However, contrary to the trend observed in the stress profiles, the peak elastic energy in the mechanical model is higher than that in the KKL model. It is because the stress and elastic energy at the interface have the following relation:

$$E_{elastic} = \frac{1}{2\mu g(\phi)}\left(\sigma_{zx}^2 + \sigma_{zy}^2\right) \tag{6.3}$$

Because of the dependence of the stiffness (μ) on the degradation function ($g(\phi)$), the elastic energy at the interface also relies on the ϕ profile. As a result, in the mechanical model, even though the peak stress is lower, the peak elastic energy is higher compared with that in the KKL model. Far from the crack tip, the elastic energy in the KKL model still agrees better with the analytical solution due to the damage accumulation issue in the mechanical model.

In conclusion, both models are not accurate in describing the near-tip stress and elastic energy distribution because of the diffuse interface. As for the stress and elastic energy far from the crack tip, the KKL model is more consistent with the analytical solution. Since the elastic energy contains all the stresses, i.e., σ_{zx} and σ_{zy}, and can also provide the information on the energy state of the system, the elastic energy is analyzed in the following sections.

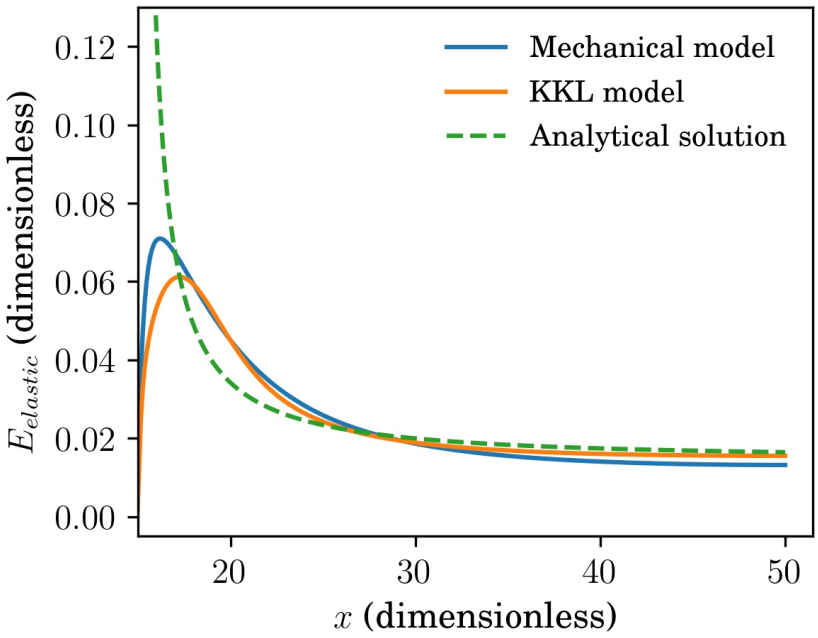

Figure 6.4: Comparisons of the elastic energy profiles in the crack plane with the analytical solution.

6.2.3 Energy Release Rate and Critical Energy Release Rate

Although the stress, elastic energy, and crack profile provide some information about the accuracy of the models, the only way to quantify the accuracy is by examining the energy release rate and the critical energy release rate. Figure 6.5a compares the elastic energy with respect to the propagation length for both models. The slope of the curve indicates the energy release rate. Theoretically, the energy release rate always equals the critical energy release rate. In the mechanical model, the energy release rate (G^M) is $1.2G_c$, while G^K is $1.5G_c$ in the KKL model. Compared with the analytical value, i.e., G_c, both models overestimate the energy release rate, and the mechanical model is more accurate. For the critical energy release rate, it can be calculated from the slope of the surface energy curve in Figure 6.5b. In both models, the critical energy release rate is slightly overestimated but the mechanical model is more accurate.

In both models, the energy release rate is larger than the critical energy release rate, which suggests that some elastic energy is lost not because of crack propagation. However, it is not surprising as the energy minimization equation (phase-field equation) can inevitably lead to the decrease of the total energy of the system, even though that results in deviations

from the LEFM. However, interestingly, in the KKL model, the energy release rate happens to equal the input elastic energy, which is also $1.5G_c$. It suggests that the energy release rate depends on the applied load, i.e., input elastic energy, instead of the material property, i.e., critical energy release rate. However, it might also simply be a coincidence and caused by some inappropriate choices of the material parameters. To examine the possible reasons, more detailed analyses are given in the latter part of this chapter.

In conclusion, both the mechanical model and the KKL model can accurately describe the critical energy release rate. However, both models overestimate the energy release rate, and whether the energy release rate in the KKL model depends on the input elastic energy requires further investigations.

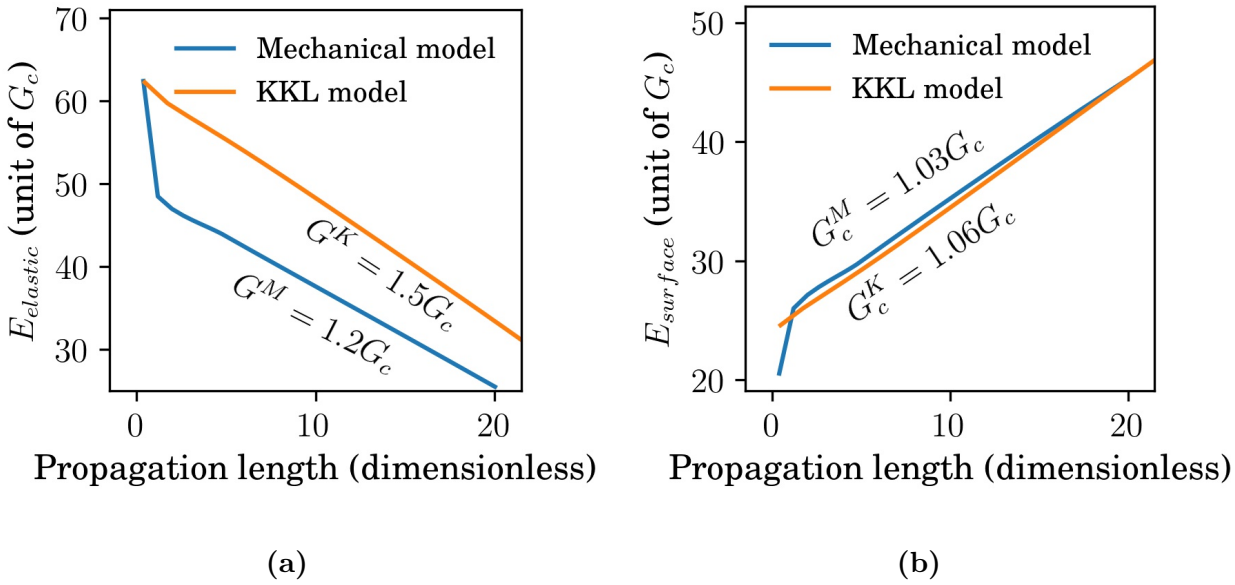

Figure 6.5: (a) Elastic energy release and (b) surface energy increment with respect to the crack propagation length for the mechanical model and the KKL model. G^M and G^K are the energy release rates for the mechanical model and the KKL model. G_c^M and G_c^K are the critical energy release ratees for the mechanical model and the KKL model.

6.3 Influence of the Irreversibility Criterion

As mentioned in Chapter 2, the irreversibility criterion should be included in both the mechanical model and the KKL model to avoid the crack recovery, i.e., ϕ increases from 0 to

1. Two types of irreversibility criteria were introduced in the literature, i.e., force $\phi = 0$ at the crack and $d\phi/dt \leq 0$. Although some 1D comparisons of these two criteria were carried out in the literature, they focused on crack initiation while neglecting the influence on crack propagation. Therefore, in this section, these irreversibility criteria were studied with 2D crack propagation simulations.

Figure 6.6 compares the phase-field and the elastic energy profiles in the crack plane for two irreversibility criteria in both models. When the crack tips reach the same position (Figures 6.6a and 6.6c), the differences in the peak elastic energies are negligible as shown in Figures 6.6b and 6.6d. In atomic scale, the peak elastic energy is directly related to the atomic bound ruptures. While in the phase-field models, it controls the reduction of ϕ at the crack front. Therefore, the peak elastic energy determines the crack motion in the next moment. Since the peak elastic energies are close, the tendency of crack propagation is insensitive to the irreversibility criterion. However, before the peak elastic energy, the elastic energy profiles are less smooth for $\phi = 0$ than those with $d\phi/dt \leq 0$ in both models. The possible reason is that inside the newly developed crack, ϕ is slightly larger than 0, which makes the criterion $\phi = 0$ unable to constrain the evolution of ϕ inside the crack. Since the elastic energy profile is quite sensitive to ϕ, the unconstrained ϕ inside the crack leads to the distortion in the elastic energy profiles.

Distinct from the phase-field profiles in the crack plane, in both models, the crack interface profiles are quite different as shown in Figure 6.7. After crack propagation when little elastic energy is left, the interface profiles recover to the analytical solutions with $\phi = 0$, while the profiles deviate from the analytical solutions with $d\phi/dt \leq 0$. However, even though the interface profile is more accurate with $\phi = 0$, it does not necessarily mean that the critical energy release rate is also more accurate.

Therefore, to quantify the effect of the irreversibility criterion on crack propagation, the energy release rate and critical energy release rate were evaluated. Figure 6.8 compares the energy with respect to the crack propagation length with different irreversibility criteria. The energy release rate and the critical energy release rate were obtained from the slopes of the elastic energy and surface energy curves in the stable regime. In both models, the energy release rate is insensitive to the irreversibility criterion. The critical energy release rate, however, varies with the irreversibility criterion in both models and is more sensitive to it in the mechanical model. It is not surprising as the interface profile in the mechanical model is more sensitive to the irreversibility criterion. In the mechanical model, the critical energy release rate is $1.03G_c$ with $d\phi/dt \leq 0$ and $0.81G_c$ with $\phi = 0$. Meanwhile, in the KKL

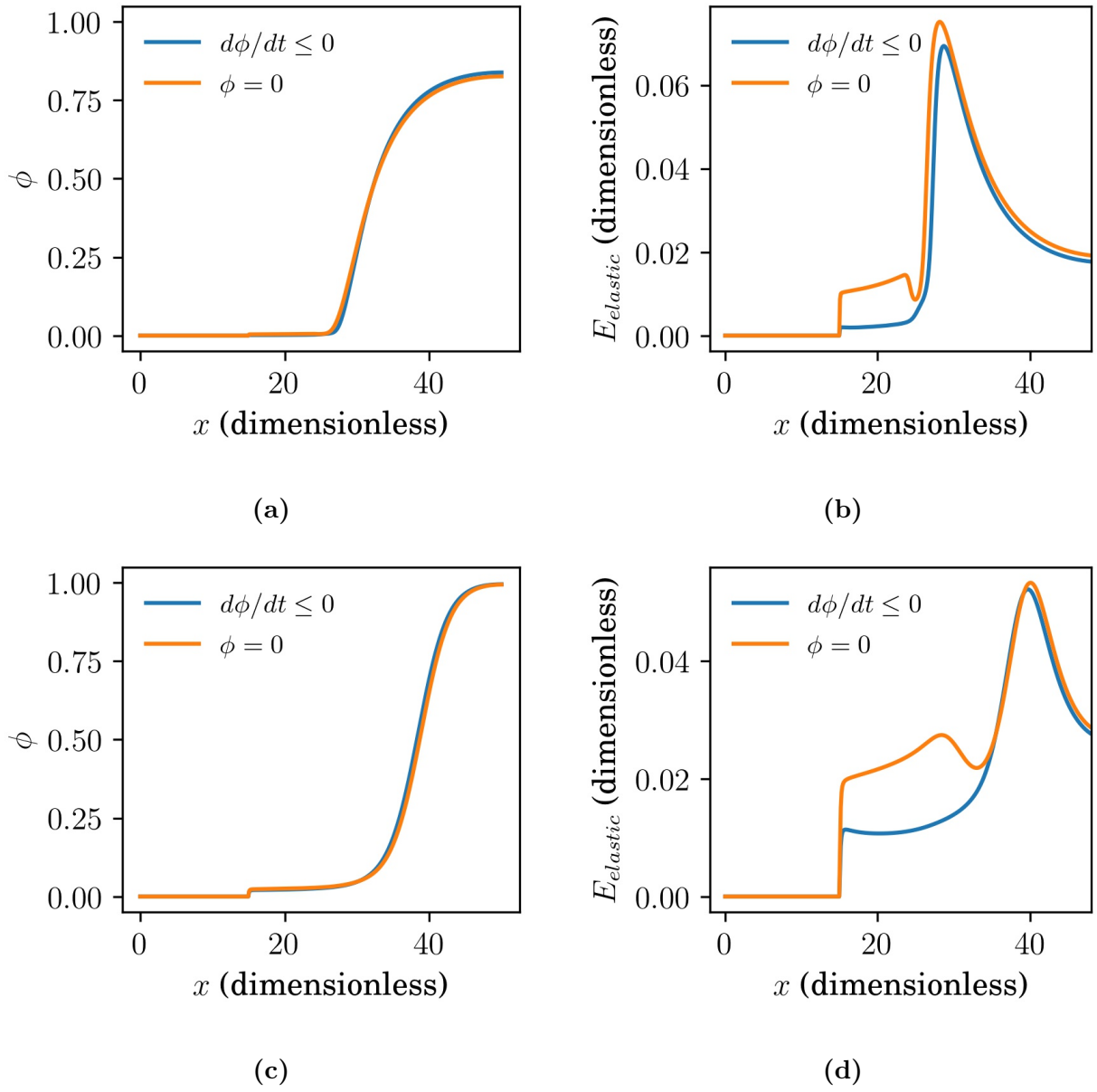

Figure 6.6: ϕ and elastic energy profiles in the crack plane for both models with different irreversibility criteria. (a) and (b) are for the mechanical model. (c) and (d) are for the KKL model.

model, it is $1.06G_c$ with $d\phi/dt \leq 0$ and $0.98G_c$ with $\phi = 0$. In both models, the cases with $\phi = 0$ underestimate the critical energy release rate, while the cases with the other criterion overestimate the critical energy release rate. Surprisingly, in the mechanical model, with $\phi = 0$, the critical energy release rate is underestimated for around 20%, even though the interface

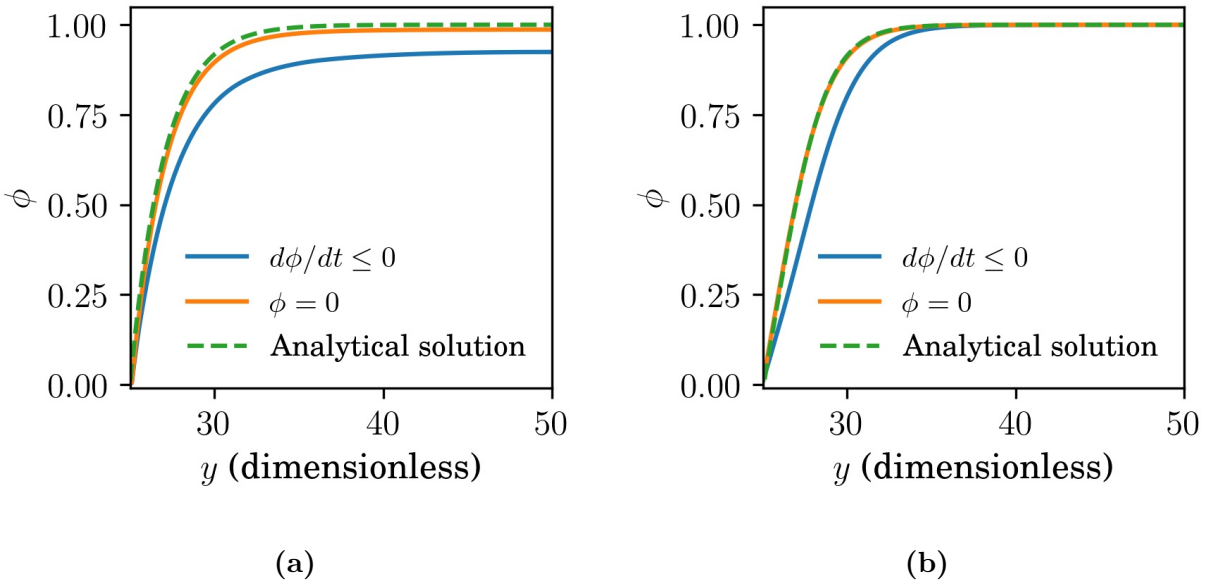

Figure 6.7: Right half of the crack interface profiles for (a) the mechanical model and (b) the KKL model with different irreversibility criteria.

profile is quite accurate compared with the analytical solution (Figure 6.7a). However, it is still reasonable as the 1D interface profile cannot accurately represent the critical energy release rate, which is an outcome of the surface energy change in 2D. Compared with the mechanical model, the change of critical energy release rate with different irreversibility criteria is negligible in the KKL model.

In conclusion, in both models, with $d\phi/dt \leq 0$, the elastic energy profile is smooth, and the critical energy release rate is more accurate with a maximum 6% overestimation compared with G_c. Therefore, $d\phi/dt \leq 0$ is a better option at least in this specific setting.

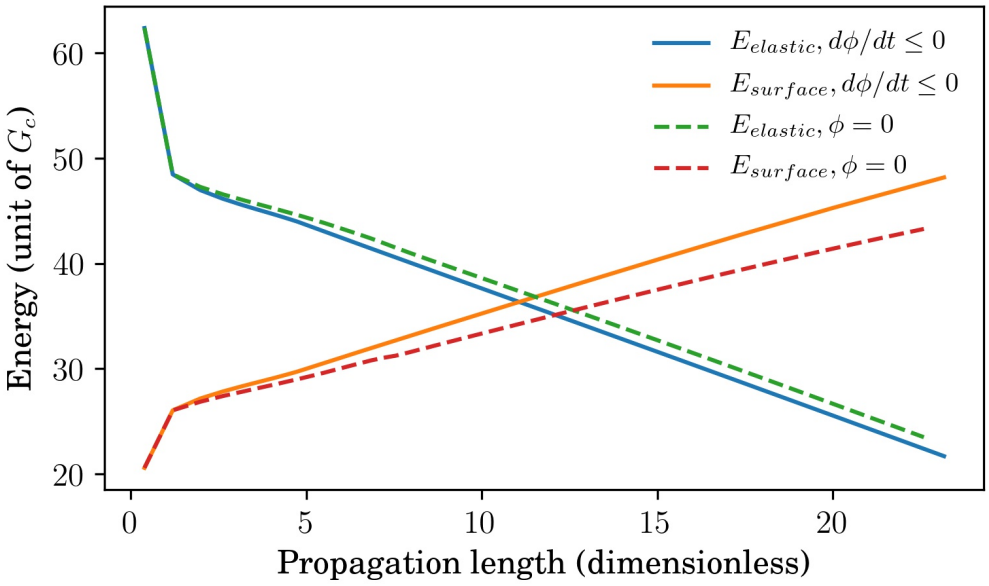

(a)

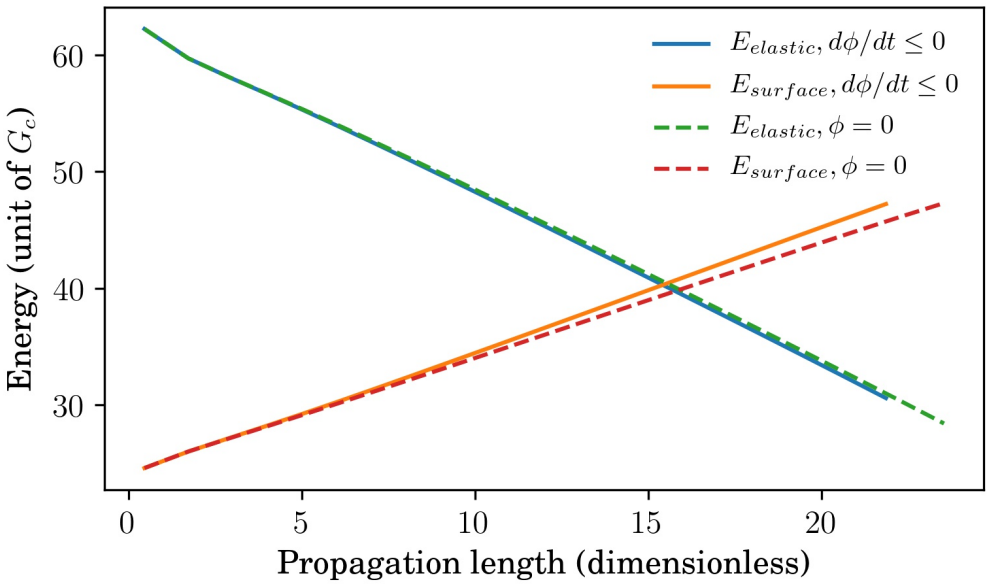

(b)

Figure 6.8: Elastic energy and surface energy with respect to the propagation length for (a) the mechanical model and (b) the KKL model with two irreversibility criteria.

6.4 Influence of the Residual Stiffness

To prevent numerical instability, residual stiffness was introduced in the mechanical model. The value of it should be small, e.g., less than 10^{-6}, to avoid the overestimation of the elastic energy. In the KKL model, however, residual stiffness has not been introduced in the literature. Therefore, to understand whether residual stiffness is required in the KKL model, 2D simulations were carried out in this section.

First, the initial crack thickness, where $\phi = 0$, was set to $1dx$. In this situation, in both models, simulations were stable even without the residual stiffness. However, with the crack thickness larger than $2dx$, the simulations became unstable in both models unless the residual stiffness is non-zero. Therefore, the residual stiffness is required even in the KKL model when the crack thickness is larger than $2dx$. In the present work, the residual stiffness was added to the KKL model in the same way as the mechanical model. By adding η to Equation (4.4), the energy functional in the KKL model reads:

$$\mathcal{F} = \int_{\Omega} \left(\frac{\kappa}{2} (\nabla \phi)^2 + \left(4\phi^3 - 3\phi^4 + \eta \right) \left(\frac{1}{2} C (\nabla u)^2 - \mathcal{E}_c \right) \right) \, d\Omega \tag{6.4}$$

To understand the role of the residual stiffness, the crack thickness in the simulations was set to $10dx$. Since the time scale does not exist in the quasi-static case, the number of loops solving the phase-field equation and the mechanical equilibrium equation was treated as a numerical time scale. Figure 6.9 compares the phase-field profiles and the elastic energy profiles in the crack plane after the same number of loops. Almost no difference can be observed in the phase-field profiles when varying η in both models. However, as expected, the elastic energy inside the crack is overestimated with a large residual stiffness in both models. With the residual stiffness less than 10^{-10}, the elastic energy profiles converge in both models.

Meanwhile, when solving the mechanical equilibrium equation with the Jacobi iteration method, the average numbers of iterations in each loop become close when $\eta \leq 10^{-10}$ as shown in Figure 6.10. Since the mechanical equilibrium equation is much more costly to solve than the phase-field equation, the number of iterations solving the mechanical equilibrium equation reflects the computational time of the simulation. Therefore, in both models, with the decrease of the residual stiffness, the computational time will eventually converge. It is also noticeable that the computational cost of the mechanical model is significantly lower than that of the KKL model, which is possibly due to the use of the different degradation functions (Equations (2.13) and (2.29)).

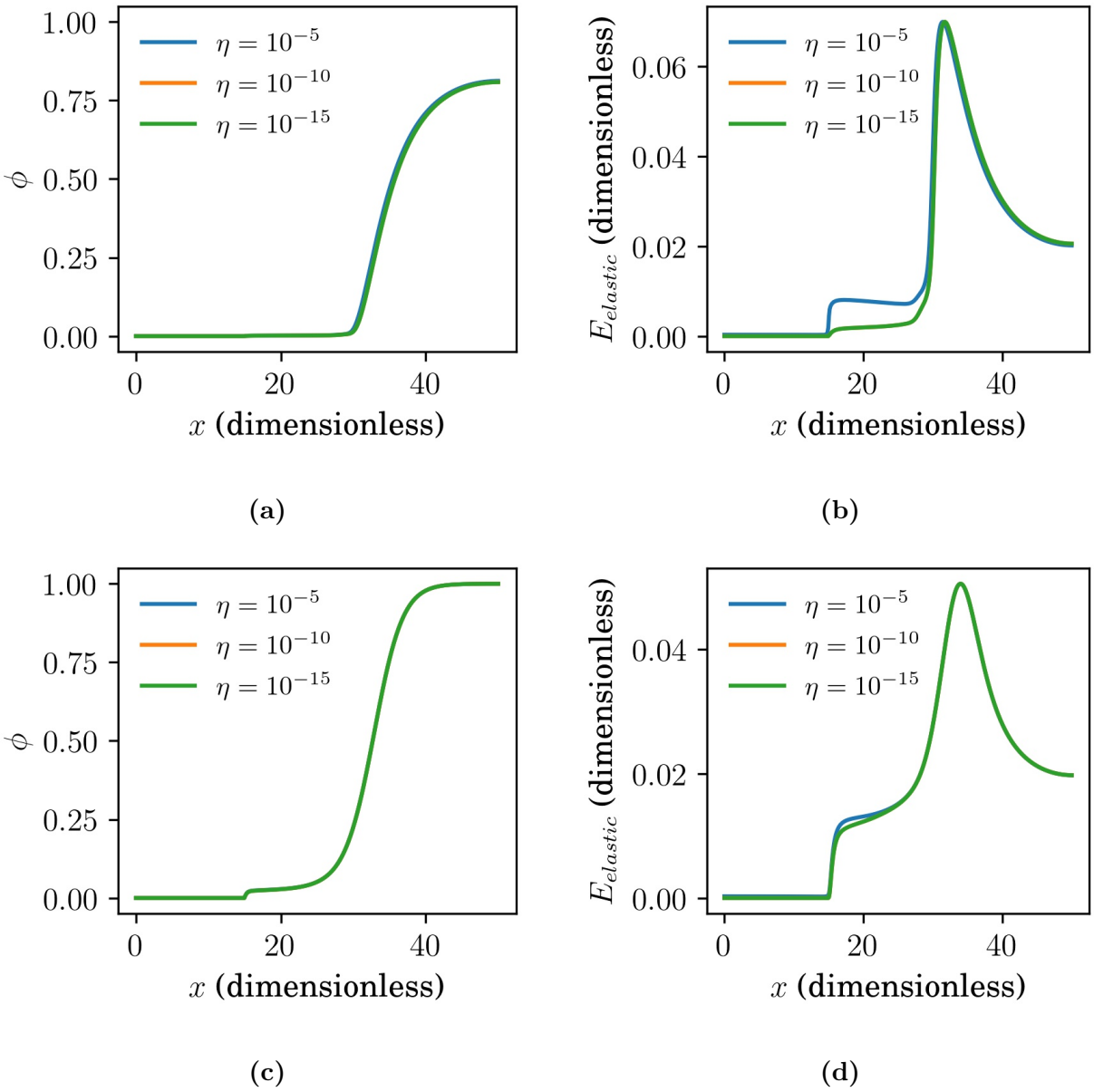

Figure 6.9: ϕ and elastic energy profiles in the crack plane along the propagation length for both models with different residual stiffness. (a) and (b) are for the mechanical model. (c) and (d) are for the KKL model.

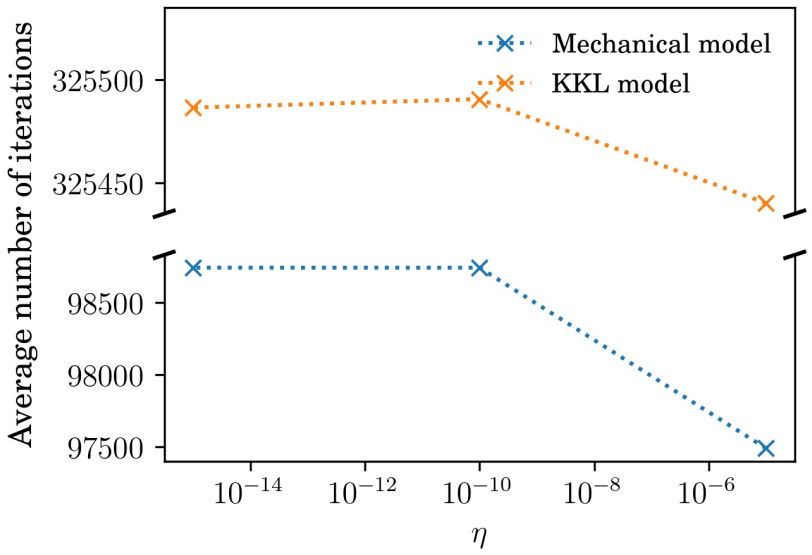

Figure 6.10: Average number of iterations solving the mechanical equilibrium equation with respect to the residual stiffness in the mechanical model and KKl model. The markers represent the data points.

6.5 Influence of the Crack Tip Curvature

Although the crack is assumed to be a sharp notch in the LEFM, it can have different shapes in reality, which can affect crack propagation. For example, the crack tip curvature (κ_{cur}), which equals the inverse of the crack tip radius (r_{tip}) (Figure 6.11), can alter the expression of the crack tip fields, and therefore changes the stress intensity factor. However, in the literature, the curvature effect was investigated by neither the mechanical model nor the KKL model. To understand the abilities of these models in capturing the curvature effect, 2D simulations with various crack tip curvatures were carried out in this section. In the simulations, the shape of the crack tip, where $\phi = 0$, was described by parabolas. The crack thickness was set to $10dx$.

Figure 6.12 compares the phase-field and elastic energy profiles in the crack plane with various crack tip curvatures. In the beginning, the elastic energy at the crack tip becomes higher when increasing the crack tip curvature. Then, shortly after the crack starts propagating, the energy profiles overlap. Therefore, the crack tip curvature only affects the initial

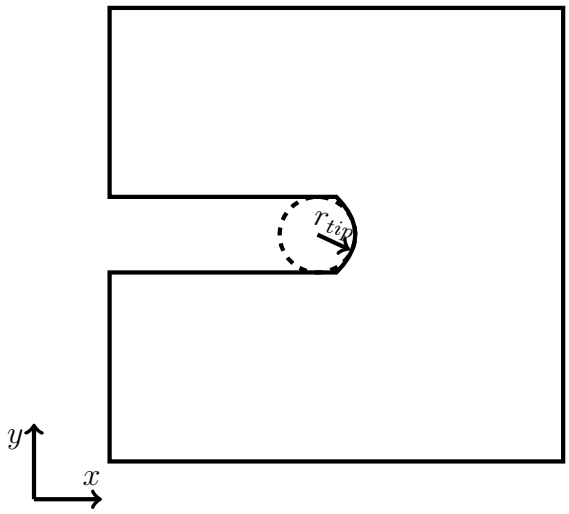

Figure 6.11: The schematics of the crack tip shape. The crack tip radius (r_{tip}) is the radius of the circle that can approximate the curve of the crack tip.

short period of crack propagation, and its influence on the overall process is negligible.

This finding can be further demonstrated by the contours of the phase-field profiles. Figure 6.13 compares the contour lines of $\phi = 0$ with different curvatures. Shortly after the crack starts propagating, the crack becomes a sharp notch in both models. Therefore, the crack shape effect can be captured by neither of the models.

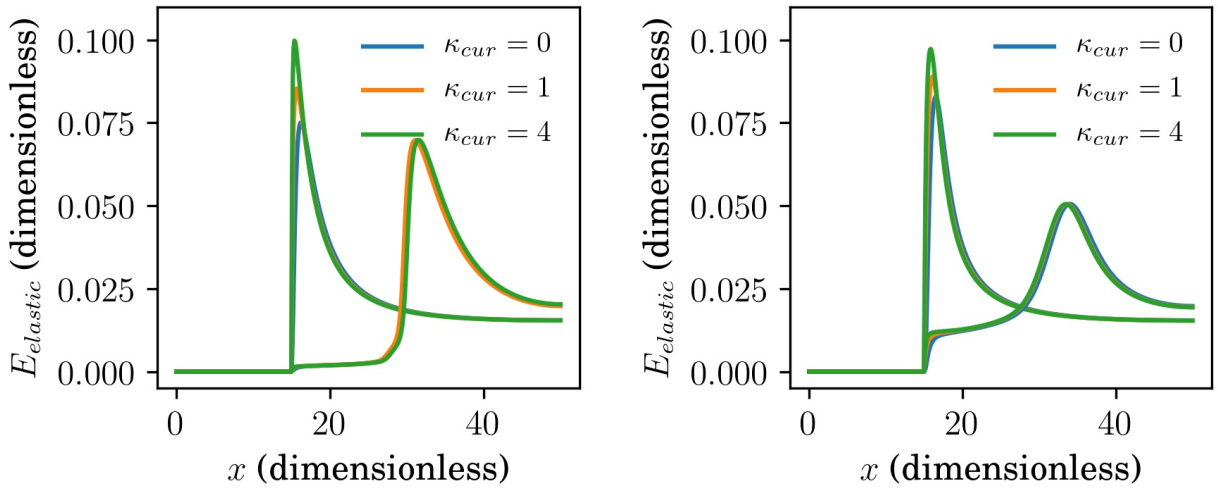

Figure 6.12: Elastic energy profiles in the crack plane in the beginning and shortly after propagation with different κ_{cur} for (a) the mechanical and (b) KKL model.

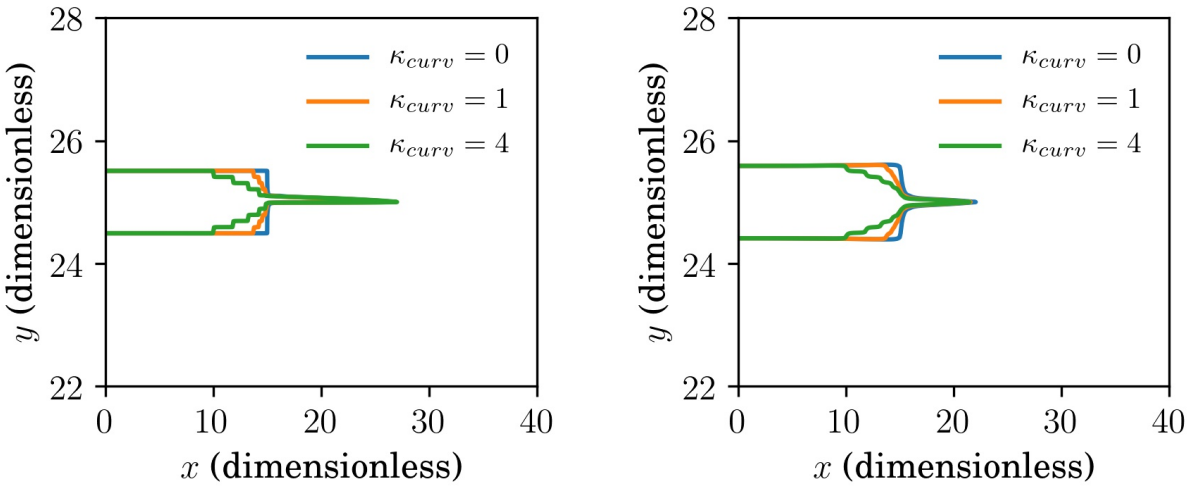

Figure 6.13: Contour lines of $\phi = 0$ with different κ_{cur} in (a) the mechanical model and (b) the KKL model.

6.6 Influence of the Input Elastic Energy

In fracture theories, the energy release rate and critical energy release rate should be independent of the load in quasi-static brittle fracture. Therefore, ideally, both models should be insensitive to the input elastic energy. However, as shown in Figures 6.14a and 6.14c, the energy release rate in both models are sensitive to the input elastic energy and become closer to the analytical value, i.e., G_c, with the decrease of E_{in}. In the KKL model, the energy release rate equals the input elastic energy in both cases. Considering all the analyses in the previous sections, it is safe to say that all the parameters are chosen properly, and the dependence of the energy release rate on E_{in} is not a coincidence. This unphysical behaviour can also be related to the sensitiveness of the critical energy release rate with the input elastic energy in the KKL model (Figure 6.14d). For the mechanical model, on the contrary, the critical energy release rate is relatively insensitive to the input elastic energy (Figure 6.14b).

Therefore, the KKL model is not appropriate to simulate quasi-static fracture as the energy release rate equals the input elastic energy. Although never mentioned in the literature, this conclusion could be the reason that nobody has applied the KKL model to quasi-static fracture.

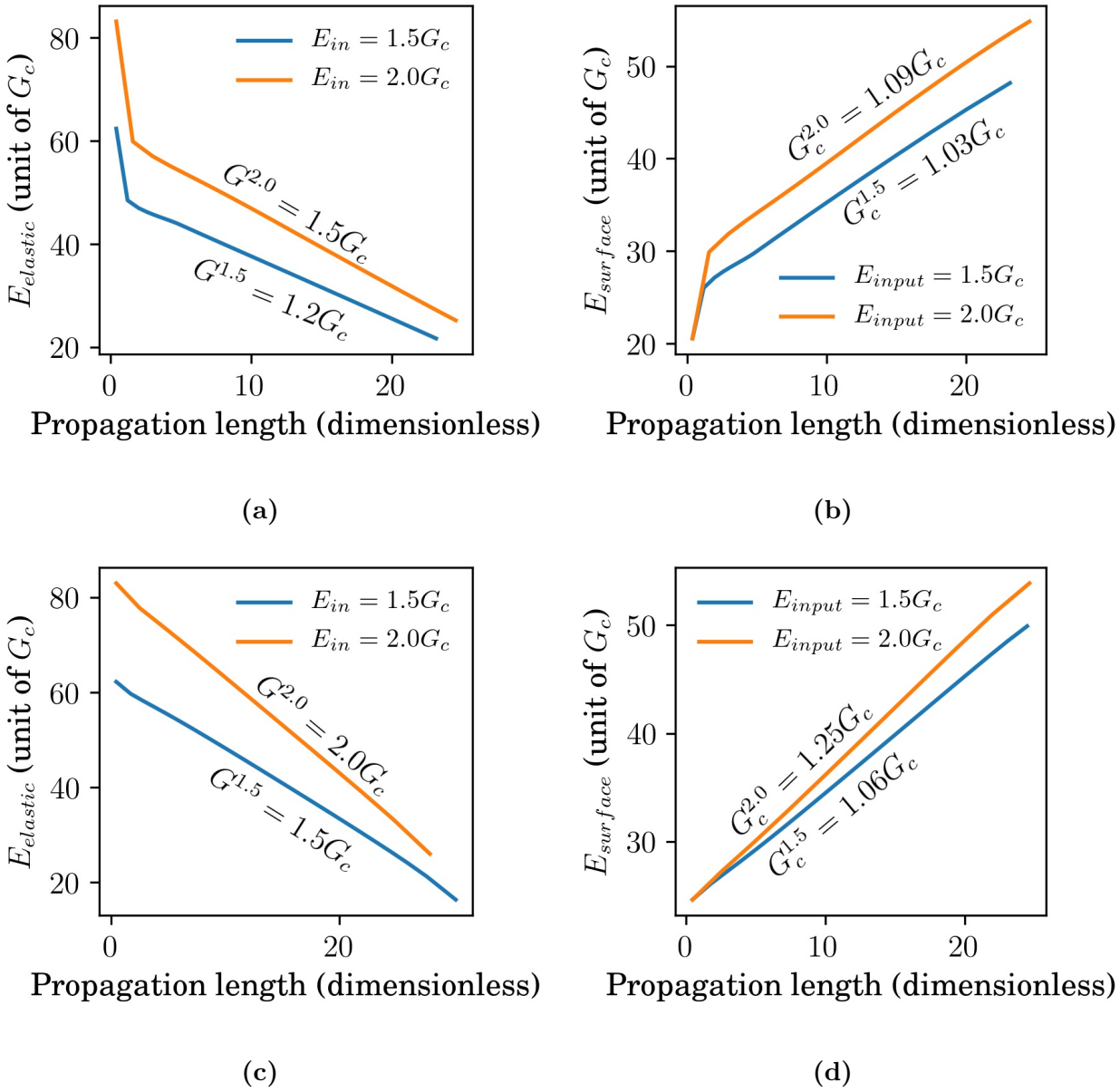

Figure 6.14: Elastic energy release and surface energy increment with respect to the crack tip position. (a) and (b) are for the mechanical model. (c) and (d) are for the KKL model. $G^{1.5}$ and $G^{2.0}$ are the energy release rates with E_{in} equal to $1.5G_c$ and $2.0G_c$. $G_c^{1.5}$ and $G_c^{2.0}$ are the critical energy release ratees with E_{in} equal to $1.5G_c$ and $2.0G_c$.

6.7 Interaction between the Crack and a Grain Boundary

Fracture in heterogeneous materials has always been a challenging topic in phase-field fracture modelling. In the mechanics community, various attempts have been made to incorporate material heterogeneity, and some of the results [81] even showed quantitative agreement with the theory. On the contrary, in the physics community, the only application to consider material heterogeneity is by Henry [106], who demonstrated that the KKL model is not suitable for simulating fracture in heterogeneous materials. Despite the similarities between the mechanical model and the KKL model, both communities have different opinions about whether the phase-field model can account for material heterogeneity. Therefore, to understand the ability of the phase-field models in capturing fracture phenomena in heterogeneous materials, the mechanical model and the KKL model were adapted for studying the role of a grain boundary during crack propagation.

The simulation setting is the same as the one used by Hansen-Dörr et al. [81]. A 45° tilted grain boundary separates two grains, and two types of critical energy release rate were assigned to the bulk (G_c^{bulk}) and the grain boundary (G_c^{int}). Since the grain boundary width has to be wide to have accurate results, the grain boundary width was set to 10, which is over twice the crack interface thickness. In the simulations, G_c^{bulk} was set to 0.5, and various G_c^{int} were tested. To be consistent with the other simulations in this thesis, the mode III loading condition was studied. Since the energy release rate is overestimated in both models because of its sensitiveness with E_{in}, E_{in} was set to the lowest value to allow the crack propagation in the bulk so that the energy release rate is the closest to the analytical value. Therefore, E_{in} is $1.33G_c^{bulk}$ in the mechanical model and $1.03G_c^{bulk}$ in the KKL model.

Figure 6.15 compares the crack behaviours with different grain boundary to bulk toughness ratios in both models. Both models correctly predict the crack deflection and penetration behaviour. The critical G_c^{int} to G_c^{bulk} ratio for crack deflection is less than 0.4 in the mechanical model and less than 0.3 in the KKL model. Compared with the theoretical ratio from the theory by He and Hutchinson [82], which is 0.85, both models deviate from the theory. The discrepancy between the simulations and the theoretical prediction is caused by the interaction between the crack interface and the grain boundary. Because of that, there are also some unphysical phenomena in the process.

The whole process contains three stages. The first stage is when the crack interface starts touching the grain boundary. In both models, the crack bends slightly downwards to meet

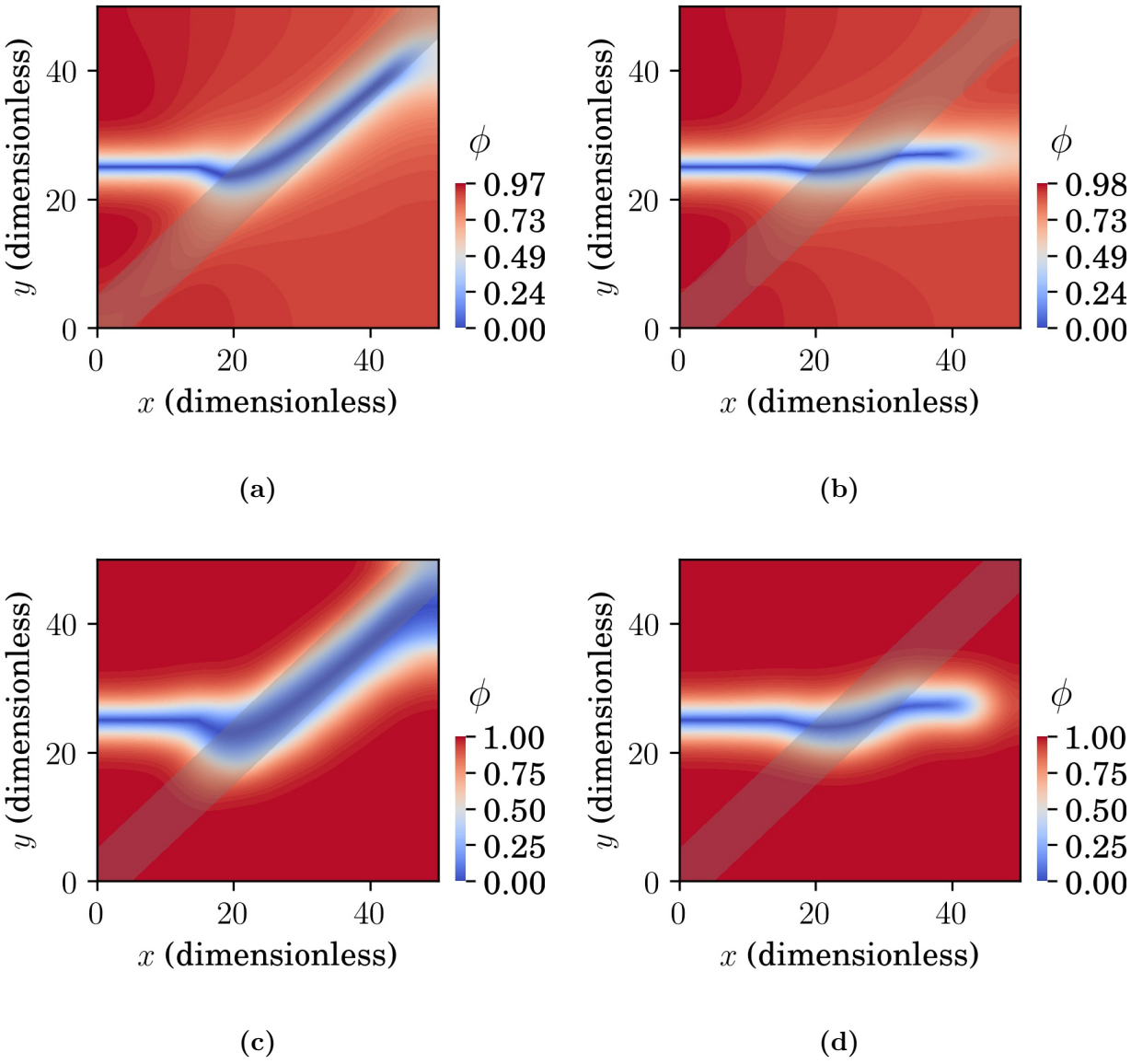

Figure 6.15: Crack path at the boundary with different G_c^{int} to G_c^{bulk} ratios. (a) and (b) are for the mechanical model with ratios equal to 0.4 and 0.7. (c) and (d) are for the KKL model with ratios equal to 0.3 and 0.6. The transparent gray band represents the grain boundary.

the grain boundary, which is because the diffuse crack interface spreads to the grain boundary even before $\phi = 0$ touching it. In the mechanical model, because ϕ ahead of the crack front is less than 1, the crack interface spreads to the grain boundary even earlier than that in the KKL model. As a result, the contribution of G_c^{int} decreases the crack surface energy. To

further reduce the surface energy, the crack tends to propagate towards the grain boundary to maximize its interface area inside the boundary. In reality, however, it should not happen as the crack path should remain unchanged before touching the grain boundary.

The second stage is when most of the crack interface is inside the boundary. When the crack propagates along the x-axis inside the grain boundary, the crack surface energy, i.e., critical energy release rate, should be G_c^{int}. Since the critical energy release rate varies with the propagation direction, when the crack deflects at the grain boundary, G_c^{int} increases and becomes a function of the deflection angle. Therefore, theoretically, the crack deflection occurs when the critical energy release rate deflecting at the boundary is lower than that propagating straight in the bulk. However, as discussed in Section 6.6, the critical energy release rate is overestimated in both models, and the overestimation becomes larger when increasing the load. The overestimation of the critical energy release rate inside the grain boundary can be indicated from the crack interface thickness in Figures 6.15a and 6.15c. Since the KKL model is more sensitive to the load, the crack interface widens significantly inside the crack as shown in Figure 6.15c. As a result, the critical energy release rate inside the grain boundary is overestimated in both models but more in the KKL model, which is the main reason for the deviations from the theory by He and Hutchinson. Apart from that, in the phase-field models, the grain boundary is defined as a thick band. Because of it, the crack deflection angle tends to be less than the grain boundary angle as the critical energy release rate is lower with a smaller angle. Strictly speaking, during deflection, the deflection angle equals the grain boundary angle. Here, it is assumed that the crack deflects at the boundary when the difference between the deflection angle and the grain boundary angle is within 10°.

In the end, even when the crack deflects at the grain boundary, it will finally leave the boundary as shown in Figures 6.15a and 6.15c. However, theoretically, it should not happen. For a sharp interface crack, once the crack propagates along the boundary, it will never go into the bulk since the critical energy release rate along the boundary is lower than that in the bulk. This unphysical penetration of the crack into the bulk is similar to the finding by Henry [106]. As in the first stage, this unphysical phenomenon is caused by the interaction between the crack interface and the grain boundary. Since the crack deflection angle is smaller than the grain boundary angle, as the crack propagates, part of the crack interface will touch the bulk. As a result, the crack surface energy increases because of the contribution of G_c^{bulk}. As the crack propagates, more of the crack interface goes into the bulk, and the crack surface energy keeps increasing. When the surface energy reaches the value allowing the crack to

propagate straight inside the bulk, the crack will leave the grain boundary. In conclusion, because of the large deviations from the theory and the unphysical phenomena, the sharp interface models might be better options than the mechanical model and the KKL model for simulating the interaction between the crack and the grain boundary.

Chapter 7

Simulations of Dynamic Crack Propagation

7.1 Introduction

The previous chapter demonstrates that the KKL model exhibits unphysical phenomena in quasi-static simulations. In dynamic fracture, both models have been successfully applied to reproduce experimental results and theoretical predictions. To compare their abilities in capturing the branching phenomenon in dynamic fracture, 2D dynamic simulations were carried out. As mentioned in Chapter 2, some of the assumptions adopted in 2D simulations are not valid in experiments, which are in 3D. Therefore, 2D dynamic branching theories especially those based on the LEFM would be ideal to be compared with the phase-field simulations. Among the theories, Adda-Bedia's theory [5] is based on the LEFM and considers the antiplane shear loading condition, which is also the loading condition used in the current work. Besides, it was employed by Karma and Lobkovsky [35] to verify the results of the KKL model. Adda-Bedia's theory, therefore, was adopted to evaluate the results of both models. In practice, branching happens either when the elastic wave interacts with the crack tip or when the crack velocity reaches a fraction of the material wave speed [109]. In the simulations, since the loading rate is zero, the only elastic wave is that radiated from the crack tip, which can interact with the crack only after being reflected from the boundary. Since Adda-Bedia did not consider the branching induced by the interaction with the elastic wave, all the analyses were carried out before the radiated elastic wave is reflected from the boundary. The parameters used in the simulations were determined in Chapter 5 and can be found in Table 7.1 unless stated explicitly.

Table 7.1: Parameters in 2D dynamic simulations

Symbol	Parameter	Value
L_x	Domain length	186
L_y	Domain width	140
l_c	Initial crack length	53.8
C	Shear modulus	1
G_c	Critical energy release rate	0.5
E_{in}	Input elastic energy	1
δ	Crack interface thickness	4
l	Internal length scale in the mechanical model	1
κ	Coefficient before the gradient term in the KKL model	1.26
$\mathcal{E}_c$	Critical elastic energy to break the material	0.05
η	Residual stiffness	10^{-10}
ρ	Material density	1
dx	Mesh size	0.1
dt	Time step size	0.02
$\Delta\phi_{threshold}$	Threshold value for ϕ in the iteration methods	10^{-5}
$\Delta u_{threshold}$	Threshold value for u in the iteration methods	10^{-7}

7.2 Investigations of the Branching Phenomena

7.2.1 Branching Velocity

In quasi-static fracture, crack propagation is extremely slow such that the velocity is zero. In dynamic fracture, however, the crack velocity is one of the most important features. During dynamic crack propagation, the crack first accelerates as the elastic energy flows into the kinetic energy. After reaching the critical velocity, crack bifurcation happens. In the meantime, the energy that flows into the crack tip is enough to create the surface energy of two branches. Since the crack tip becomes blunt before bifurcation, more energy flows into the surface energy. As a result, less energy transforms into kinetic energy, and the crack velocity decreases before branching. After branching, the microcracks developed at the crack tip region lead to velocity oscillation.

Figure 7.1a compares the crack tip velocity with respect to the crack tip position for both

models. Both models predict the general trend of dynamic crack propagation. The dotted lines in Figures 7.1a and 7.1b indicate the branching positions. Before branching, the crack accelerates, and then the velocity decreases during crack tip blunting. After branching, the velocity becomes unstable. However, compared with the mechanical model, the KKL model predicts higher crack velocity. Naturally, one might think that it is because of the different magnitudes of the peak elastic energy at the crack tip region since the peak elastic energy acts as the 'force' in crack propagation. Figure 7.2a compares the elastic energy in the crack plane for both models. The lower peak elastic energy in the KKL model suggests that it cannot be the reason for the higher crack velocity. The other possible explanation is that the phase-field profiles behave differently even with the same peak elastic energy because of the different phase-field formulations. Apart from the peak elastic energy, it is also noticeable that in the KKL model, the elastic energy has a secondary spike inside the crack, which is caused by the delay in the movement of the smaller ϕ as shown in Figure 7.2b. Since the smaller ϕ that lags behind is negligible in magnitude and moves with the crack front, the secondary spike in the elastic energy is negligible. As in the quasi-static case, because of the damage accumulation, ϕ ahead of the crack front in the mechanical model is less than 1 as shown in Figure 7.2b. As a result, the elastic energy far from the crack tip is slightly lower than that in the KKL model as shown in Figure 7.2a.

Apart from the crack velocity, because of the different phase-field formulations, the branching position is also quite different as shown in Figure 7.1b. However, in Adda-Bedia's theory, the crack is assumed to be propagating at a constant velocity before branching, and the acceleration process is ignored. As a result, neither the actual propagation velocity nor the branching position can be known from the theory. Therefore, the critical branching velocity is the only feature that can be compared with Adda-Bedia's theory.

In Adda-Bedia's theory, the critical branching velocity is $0.39C_s$. Before comparing with the phase-field simulations, it has to be mentioned that in the theory, the critical branching velocity is derived based on a limiting case where the velocity immediately after branching is assumed to be zero. In the phase-field simulations, however, that is not true as shown in Figure 7.1a. According to Adda-Bedia, with the increase of the velocity after branching, the critical branching velocity should become higher. Therefore, the actual branching velocity should be above $0.39C_s$. As shown in Figure 7.1a, the branching velocity is $0.28C_s$ in the mechanical model and $0.38C_s$ in the KKL model. As mentioned in Section 5.4, the branching velocity in the mechanical model is sensitive to ϕ_{front}. Considering the 20% error induced by ϕ_{front}, the branching velocity in the mechanical model should range from $0.22C_s$ to $0.28C_s$.

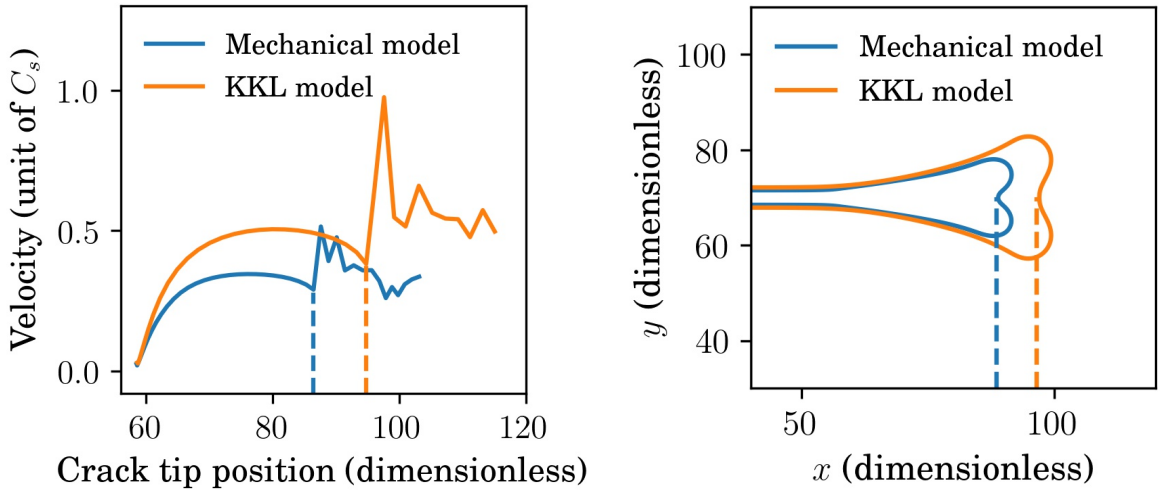

(a) **(b)**

Figure 7.1: (a) The crack velocity with respect to the crack tip position and (b) the contour of ϕ profile with level set to 0.5 both models. The dotted lines in both (a) and (b) correspond to the branching positions.

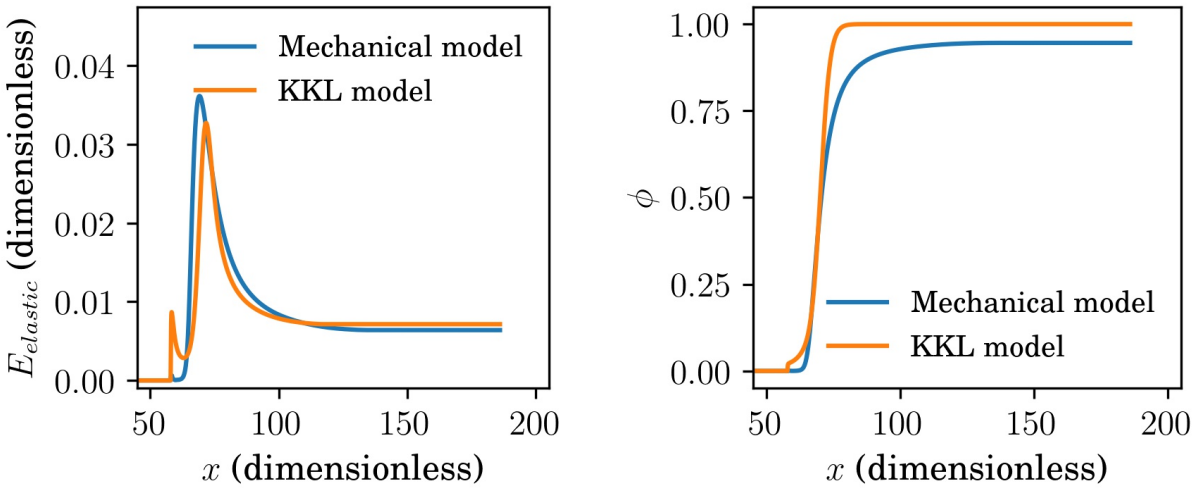

(a) **(b)**

Figure 7.2: (a) The elastic energy profiles and (b) ϕ profiles in the crack plane for the mechanical model and the KKL model.

Compared with the theoretical value, both models underestimate the branching velocity, but the KKL model is more consistent with Adda-Bedia's theory.

7.2.2 Branching Angle

In Adda-Bedia's theory, the branching angle is 79.2°, which is also derived based on a limiting case. Figure 7.3 compares the crack shapes of both models. The branching angle is 47.3° in the mechanical model and 64.5° in the KKL model. Compared with the theoretical prediction, i.e., 79.2°, both models underestimate the branching angle, but the KKL model is more consistent with the theory.

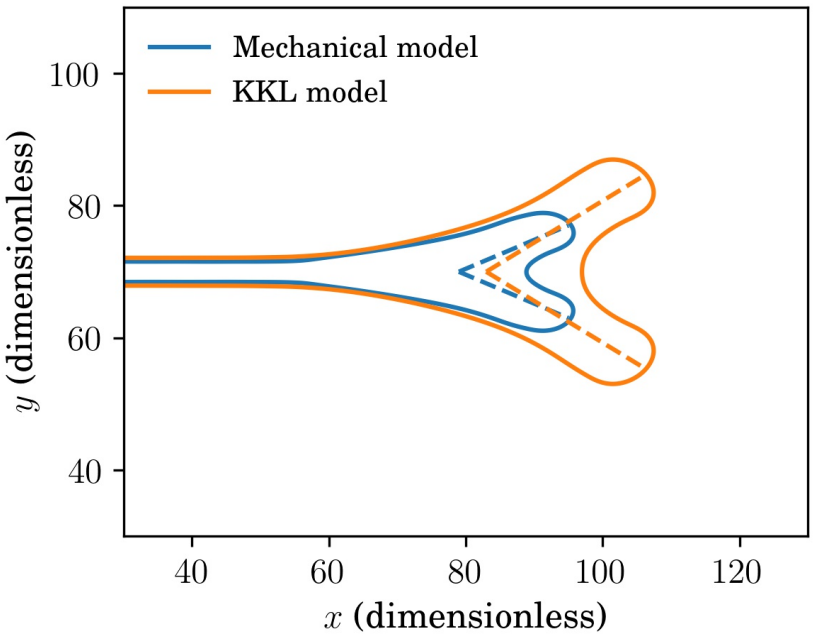

Figure 7.3: Contour lines of $\phi = 0.5$ in the mechanical model and the KKL model. The dotted lines are used to determine the branching angles.

7.2.3 Branching Energy Release Rate

An alternative theory to be compared with is the one by Eshelby [4]. Eshelby suggested that the crack bifurcates when the energy release rate becomes twice the critical energy release rate of a single crack. Then by studying the limiting case, where the branching angle and the velocity after branching are zero, the branching velocity was obtained. In the

limiting case, the energy release rate for branching is $2G_c$. Although based on the same idea, in Adda-Bedia's theory, the branching angle is no longer assumed to be zero. Therefore, the energy release rate for branching becomes a function of the branching angle (λ) given as: $2\left((360-\lambda)/\lambda\right)^{\lambda/360} G_c$ [5]. Although the branching velocity in Eshelby's theory is less accurate compared with that in Adda-Bedia's theory, the fundamental ideas of both theories are the same as they are all based on the critical energy condition for branching.

Unlike the energy release rate in quasi-static fracture, in dynamic fracture, it cannot be calculated directly from the elastic energy as the kinetic energy is also involved in the propagation process. However, since the energy release rate equals the critical energy release rate according to the Griffith theory, the critical energy release rate can be evaluated instead. As in the quasi-static case, the critical energy release rate can be calculated easily from the slope of the surface energy curves.

Figure 7.4 compares the critical energy release rate or equivalently the energy release rate with respect to the crack tip position in both models. In the beginning, the crack velocity is close to 0. Therefore, the critical energy release rate theoretically should be G_c. However, in the mechanical model, the initial critical energy release rate is overestimated and is around $1.5G_c$. On the contrary, the initial value in the KKL model is quite accurate. Because of the overestimation of the initial critical energy release rate in the mechanical model, the curve is always higher compared with that in the KKL model as shown in Figure 7.4. With the initial critical energy release rate obtained from Figure 7.4, the branching angle, and the relation between the branching angle and the critical energy release rate, the theoretical energy release rate for branching then becomes $3.84G_c$ for the mechanical model and $2.63G_c$ for the KKL model. With the branching positions determined from Figure 7.1a and the critical energy release rate curves in Figure 7.4, the critical energy release rate for branching in the phase-field simulations is derived, which is $3.68G_c$ in the mechanical model and $3.9G_c$ for the KKL model. Compared with the theoretical values, i.e., $3.84G_c$ and $2.63G_c$, the mechanical model underestimates the energy by 4%, while the KKL model overestimates the value by 48%. The significant overestimation of the critical branching energy in the KKL model suggests that the mechanical model is more consistent with Eshelby's theory.

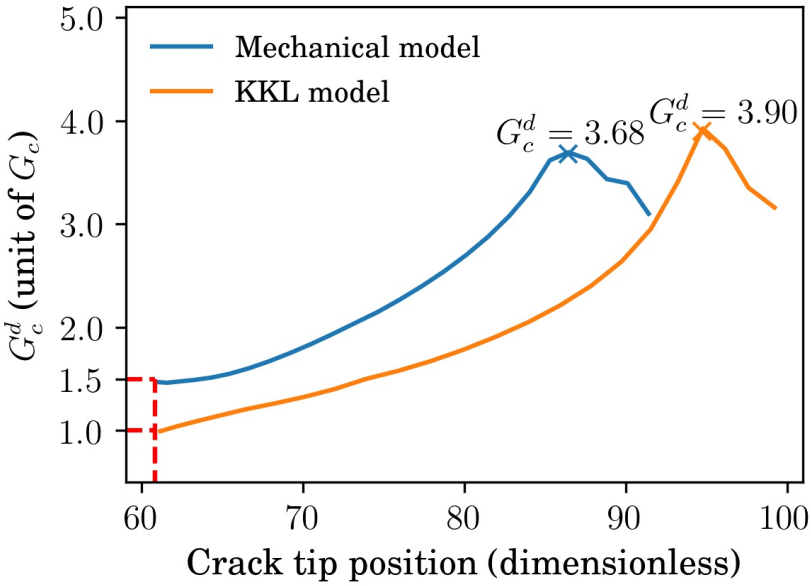

Figure 7.4: The critical energy release rate with respect to the crack tip position. The markers indicate the critical value for branching. The red dotted lines indicate the positions of the curves.

7.3 Influence of the Input Elastic Energy

To understand the robustness of the models, parameter analysis was carried out in this section. In the theories by Eshelby and Adda-Bedia, the critical branching conditions are independent of the load, which is E_{in} in the current work. However, as demonstrated in Chapter 6, both models are sensitive to E_{in} in the quasi-static setting. Therefore, it is worth knowing whether these models are also sensitive to E_{in} in dynamic fracture. Two input elastic energies, i.e., $2.0G_c$ and $2.5G_c$, were investigated in this section. The rest of the parameters can be found in Table 7.1.

Figure 7.5 compares the velocity with respect to the crack tip position for both models with different E_{in}. In both models, the velocity increases slightly with the increase of the input elastic energy, because more energy flows into the kinetic energy. For the branching velocity, with the increase of E_{in}, it only increases by 3.4% in the mechanical model and decreases by 5.3% in the KKL model as indicated by the dotted lines. Therefore, considering the errors induced by the selections of ϕ_{front} and the domain width, the branching velocity is insensitive to E_{in} in both models.

As for the branching angle, in both models, it increases slightly, i.e., less than 10°, with

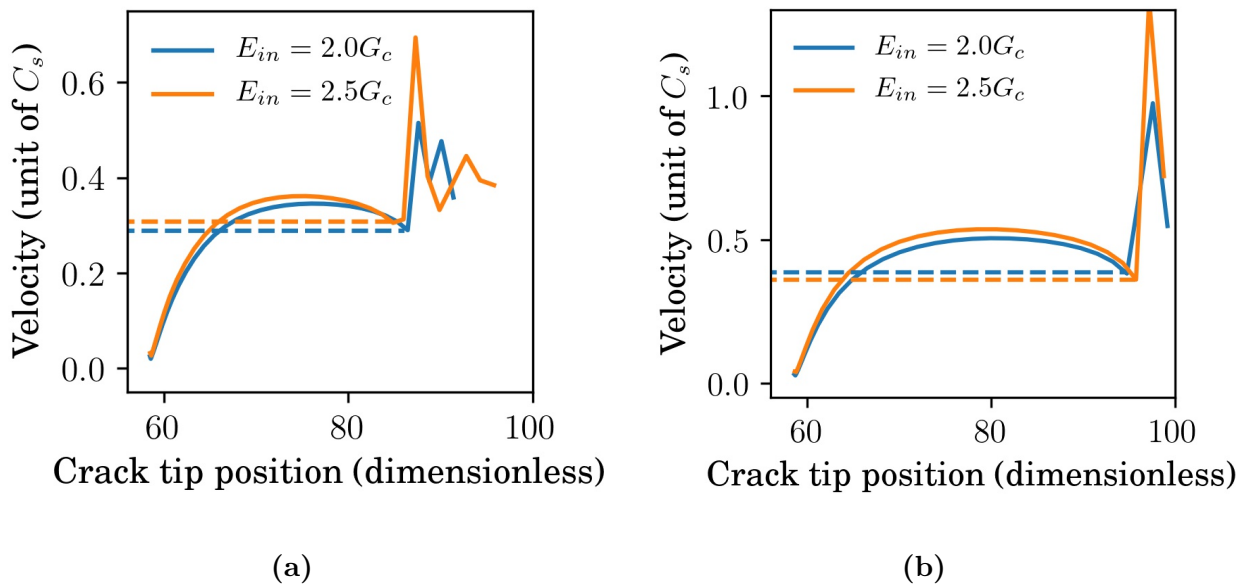

Figure 7.5: The crack velocity with respect to the crack tip position in the (a) mechanical model and the (b) KKL model with different E_{in}. The dotted lines indicate the values of the critical branching velocities.

the increase of E_{in} as shown in Figure 7.6. The inner part of the branch, however, does not move when increasing E_{in}. Therefore, the increase in the branching angle with E_{in} is caused by the thickening of the crack tip. Since the variance of the branching angle with E_{in} is negligible compared with the error introduced when selecting the dotted lines, the branching angle is insensitive to E_{in}.

At last, the influence of E_{in} on the critical energy release rate was evaluated. Figure 7.7 compares the critical energy release rate with respect to the crack tip position with different E_{in}. In both models, the initial critical energy release rate is insensitive to the input elastic energy. However, the critical energy release rate increases with the increase of E_{in} because more elastic energy transforms into the crack surface energy. As a result, the crack tip thickens. The critical energy release rates for branching are shown in the dotted lines in Figure 7.7. Since the branching angle is insensitive to E_{in}, the critical energy release rate for branching based on Eshelby's theory does not change, which is $3.84G_c$ for the mechanical model and $2.63G_c$ for the KKL model. In the mechanical model, with the increase of E_{in}, the discrepancy with the theory decreases from 4% to 2%. Meanwhile, in the KKL model, the discrepancy increases from 48% to 69%. Therefore, the critical energy release rate for branching is sensitive to E_{in} in the KKL model.

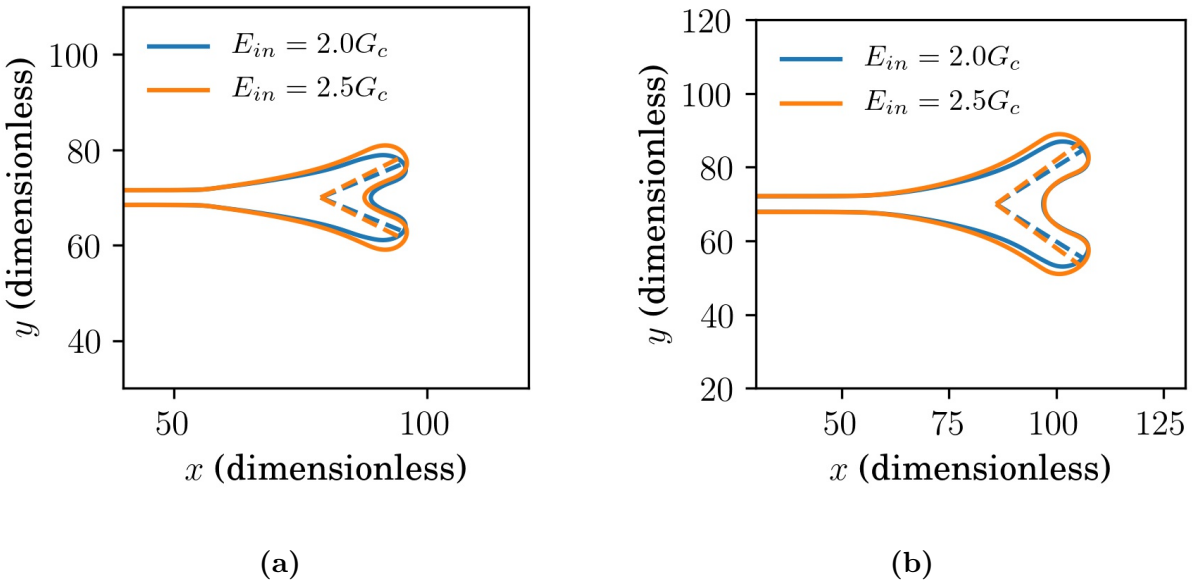

(a) (b)

Figure 7.6: Contour lines of $\phi = 0.5$ with different E_{in} in the (a) mechanical model and (b) the KKL model.

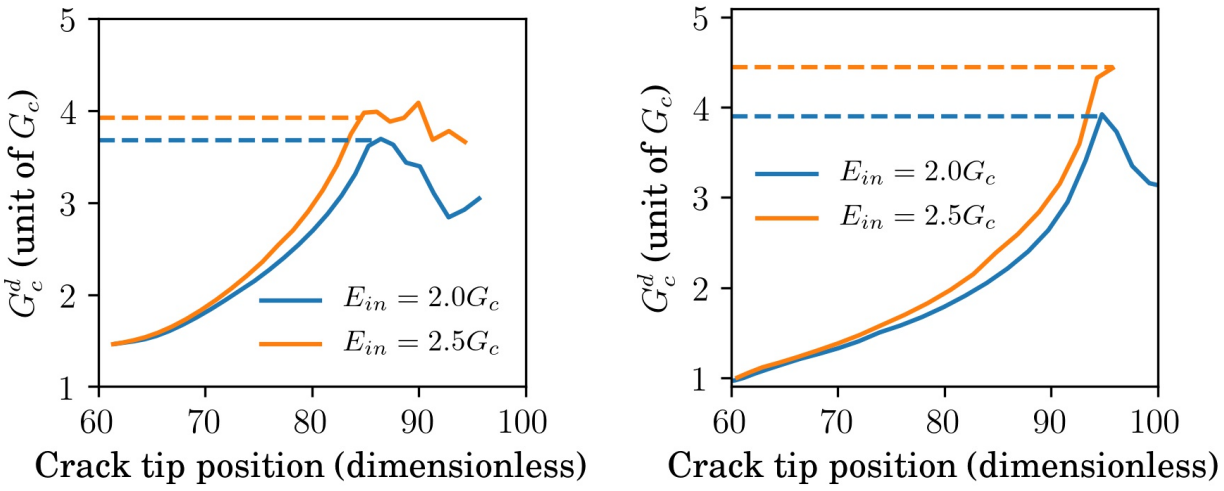

(a) (b)

Figure 7.7: The critical energy release rate with respect to the crack tip position with different E_{in} for the (a) mechanical model and the (b) KKL model.

In conclusion, both the mechanical model and the KKL model agree well with dynamic fracture theories. In terms of predicting the branching phenomena by Adda-Bedia, the KKL

model is more accurate. Compared with the energetic theory by Eshelby, the mechanical model showed a better agreement. As mentioned earlier, these theories are for the limiting case in which some assumptions are not valid in the phase-field simulations. Therefore, comparisons with experiments are required to evaluate the accuracy of the models.

Chapter 8

Summary and Future Work

8.1 Summary

Two representative phase-field fracture models in the mechanics and the physics community, i.e., Miehe et al.'s model [1] and the KKL model, were compared in the quasi-static and the dynamic setting. The simulation settings and the numerical techniques for the model implementation were illustrated in Chapter 4. Through various comparisons in Chapters 6 and 7, the strengths and limitations of these models were elucidated. The main findings are summarized below.

In the quasi-static case, both models were compared with the Griffith theory. It was found that the KKL model cannot be applied to quasi-static fracture as the energy release rate depends on the load (E_{in}) instead of the material parameter (G_c). The mechanical model, on the other hand, is more appropriate for simulating quasi-static fracture. However, the mechanical model also has some limitations. The crack tip curvature effect, although, exists in reality, cannot be captured. The sensitiveness of the phase-field profile with the load leads to the overestimation of the energy release rate. For crack propagation in a bi-grain system, because of the interaction between the crack interface and the grain boundary, both models deviate from the theory and exhibit unphysical phenomena.

As for the dynamic fracture, the KKL model agrees well with the branching angle and velocity in Adda-Bedia's theory [5]. The mechanical model, however, underestimates the branching angle and velocity by 40% and 28%. Apart from Adda-Bedia's theory, Eshelby's theory [4] was also adopted to identify the critical branching condition. It was observed that the mechanical model agrees well with the theory, while the KKL model overestimates the theoretical value by 48%. However, since these theories are for the limiting case where some assumptions are not valid in phase-field simulations, comparisons with experiments are necessary to evaluate the accuracy of the models.

Therefore, this work illustrated that for quasi-static simulations, the mechanical model is a better choice. For the dynamic case, more investigations into both models are necessary.

8.2 Future Work

The following extensions of the study are suggested:

- The selection of the domain size is restricted by the computational cost in the quasi-static simulations. To enable the use of larger domain size, the adaptive meshing technique could be used, where only the interface has the fine mesh.
- The current work is restricted to the mode III fracture. However, in other fracture modes, the findings in this project may not be applicable. Therefore, simulations with other fracture modes are required.
- In dynamic simulations, the fracture phenomena could be compared with experiments to evaluate the accuracy of the model predictions. Besides, to compare with experiments, these models should be implemented in 3D.
- Instead of using ϕ_{front} to identify the crack front position, alternative methods can be used such that the velocity and crack shape could be captured with higher accuracy. For example, the crack front can be identified by the position with the peak elastic energy.

Bibliography

[1] C. Miehe, M. Hofacker, and F. Welschinger, "A phase field model for rate-independent crack propagation: Robust algorithmic implementation based on operator splits," *Computer Methods in Applied Mechanics and Engineering*, vol. 199, no. 45-48, pp. 2765–2778, 2010.

[2] A. Karma, D. A. Kessler, and H. Levine, "Phase-field model of mode iii dynamic fracture," *Physical Review Letters*, vol. 87, no. 4, p. 045501, 2001.

[3] A. A. Griffith, "Vi. the phenomena of rupture and flow in solids," *Philosophical Transactions of the Royal Society of London. Series A, Containing Papers of a Mathematical or Physical Character*, vol. 221, no. 582-593, pp. 163–198, 1921.

[4] J. D. Eshelby, "Energy relations and the energy-momentum tensor in continuum mechanics," in *Fundamental Contributions to the Continuum Theory of Evolving Phase Interfaces in Solids*, pp. 82–119, Springer, 1999.

[5] M. Adda-Bedia, "Brittle fracture dynamics with arbitrary paths. ii. dynamic crack branching under general antiplane loading," *Journal of the Mechanics and Physics of Solids*, vol. 52, no. 6, pp. 1407–1420, 2004.

[6] R. P. Reed, *The economic effects of fracture in the United States*, vol. 647. US Department of Commerce, National Bureau of Standards, 1983.

[7] K. Ravi-Chandar, *Dynamic fracture*. Elsevier, 2004.

[8] G. R. Irwin, "Analysis of stresses and strains near the end of a crack transversing a plate," *Journal of Aplied Mechanics, Transactions ASME*, vol. 24, pp. 361–364, 1957.

[9] B. Lawn, *Fracture of brittle solids*. Cambridge University Press, 1993.

[10] F. Erdogan and G. C. Sih, "On the crack extension in plates under plane loading and transverse shear," *Journal of Basic Engineering*, vol. 85, no. 4, pp. 519–525, 1963.

[11] G. C. Sih and B. Macdonald, "Fracture mechanics applied to engineering problems-strain energy density fracture criterion," *Engineering Fracture Mechanics*, vol. 6, no. 2, pp. 361–386, 1974.

[12] M. A. Hussain, S. L. Pu, and J. Underwood, "Strain energy release rate for a crack under combined mode i and mode ii," in *Fracture Analysis: Proceedings of the 1973 National Symposium on Fracture Mechanics, Part II*, ASTM International, 1974.

[13] N. Moës, J. Dolbow, and T. Belytschko, "A finite element method for crack growth without remeshing," *International Journal for Numerical Methods in Engineering*, vol. 46, no. 1, pp. 131–150, 1999.

[14] T. Belytschko and T. Black, "Elastic crack growth in finite elements with minimal remeshing," *International Journal for Numerical Methods in Engineering*, vol. 45, no. 5, pp. 601–620, 1999.

[15] P.-O. Bouchard, F. Bay, Y. Chastel, and I. Tovena, "Crack propagation modelling using an advanced remeshing technique," *Computer Methods in Applied Mechanics and Engineering*, vol. 189, no. 3, pp. 723–742, 2000.

[16] P.-O. Bouchard, F. Bay, and Y. Chastel, "Numerical modelling of crack propagation: automatic remeshing and comparison of different criteria," *Computer Methods in Applied Mechanics and Engineering*, vol. 192, no. 35-36, pp. 3887–3908, 2003.

[17] T. K. Hellen, "The finite element calculation of stress intensity factors using energy techniques," in *The Second International Conference on Structural Mechanics in Reactor Technology*, (Berin, Germany), IASMiRT, 1973.

[18] D. M. Parks, "A stiffness derivative finite element technique for determination of crack tip stress intensity factors," *International Journal of Fracture*, vol. 10, no. 4, pp. 487–502, 1974.

[19] T. K. Hellen, "On the method of virtual crack extensions," *International Journal for Numerical Methods in Engineering*, vol. 9, no. 1, pp. 187–207, 1975.

[20] P. Destuynder, M. Djaoua, and S. Lescure, "Quelques remarques sur la mécanique de la rupture élastique," *Journal de Mécanique Théorique et Appliquée*, vol. 2, no. 1, pp. 113–115, 1983.

[21] L. B. Freund, *Dynamic fracture mechanics*. Cambridge University Press, 1998.

[22] E. H. Yoffe, "Lxxv. the moving griffith crack," *The London, Edinburgh, and Dublin Philosophical Magazine and Journal of Science*, vol. 42, no. 330, pp. 739–750, 1951.

[23] S. P. Patil and Y. Heider, "A review on brittle fracture nanomechanics by all-atom simulations," *Nanomaterials*, vol. 9, no. 7, p. 1050, 2019.

[24] R. Kobayashi, "Modeling and numerical simulations of dendritic crystal growth," *Physica D: Nonlinear Phenomena*, vol. 63, no. 3-4, pp. 410–423, 1993.

[25] W. J. Boettinger, J. A. Warren, C. Beckermann, and A. Karma, "Phase-field simulation of solidification," *Annual Review of Materials Research*, vol. 32, no. 1, pp. 163–194, 2002.

[26] W. J. Boettinger, A. A. Wheeler, B. T. Murray, and G. B. McFadden, "Prediction of solute trapping at high solidification rates using a diffuse interface phase-field theory of alloy solidification," *Materials Science and Engineering: A*, vol. 178, no. 1-2, pp. 217–223, 1994.

[27] B. Böttger, J. Eiken, and I. Steinbach, "Phase field simulation of equiaxed solidification in technical alloys," *Acta Materialia*, vol. 54, no. 10, pp. 2697–2704, 2006.

[28] B. Zhu and M. Militzer, "3d phase field modelling of recrystallization in a low-carbon steel," *Modelling and Simulation in Materials Science and Engineering*, vol. 20, no. 8, p. 085011, 2012.

[29] T. Takaki, Y. Hisakuni, T. Hirouchi, A. Yamanaka, and Y. Tomita, "Multi-phase-field simulations for dynamic recrystallization," *Computational Materials Science*, vol. 45, no. 4, pp. 881–888, 2009.

[30] Y. Suwa, Y. Saito, and H. Onodera, "Phase field simulation of stored energy driven interface migration at a recrystallization front," *Materials Science and Engineering: A*, vol. 457, no. 1-2, pp. 132–138, 2007.

[31] D.-H. Yeon, P.-R. Cha, and J.-K. Yoon, "A phase field study for ferrite–austenite transitions under para-equilibrium," *Scripta Materialia*, vol. 45, no. 6, pp. 661–668, 2001.

[32] R. G. Thiessen, J. Sietsma, T. A. Palmer, J. W. Elmer, and I. M. Richardson, "Phase-field modelling and synchrotron validation of phase transformations in martensitic dual-phase steel," *Acta Materialia*, vol. 55, no. 2, pp. 601–614, 2007.

[33] I. Steinbach and M. Apel, "The influence of lattice strain on pearlite formation in fe–c," *Acta Materialia*, vol. 55, no. 14, pp. 4817–4822, 2007.

[34] M. Militzer, M. G. Mecozzi, J. Sietsma, and S. Van der Zwaag, "Three-dimensional phase field modelling of the austenite-to-ferrite transformation," *Acta Materialia*, vol. 54, no. 15, pp. 3961–3972, 2006.

[35] A. Karma and A. E. Lobkovsky, "Unsteady crack motion and branching in a phase-field model of brittle fracture," *Physical Review Letters*, vol. 92, no. 24, p. 245510, 2004.

[36] C. Kuhn and R. Müller, "A continuum phase field model for fracture," *Engineering Rracture Mechanics*, vol. 77, no. 18, pp. 3625–3634, 2010.

[37] A. Schlüter, A. Willenbücher, C. Kuhn, and R. Müller, "Phase field approximation of dynamic brittle fracture," *Computational Mechanics*, vol. 54, no. 5, pp. 1141–1161, 2014.

[38] L.-Q. Chen, "Phase-field models for microstructure evolution," *Annual Review of Materials Research*, vol. 32, no. 1, pp. 113–140, 2002.

[39] G. A. Francfort and J.-J. Marigo, "Revisiting brittle fracture as an energy minimization problem," *Journal of the Mechanics and Physics of Solids*, vol. 46, no. 8, pp. 1319–1342, 1998.

[40] L. Kachanov, *Introduction to continuum damage mechanics*, vol. 10. Springer Science & Business Media, 1986.

[41] J. Mazars and G. Pijaudier-Cabot, "Continuum damage theory—application to concrete," *Journal of Engineering Mechanics*, vol. 115, no. 2, pp. 345–365, 1989.

[42] Z. P. Bazant, "Mechanics of distributed cracking," *Applied Mechanics Reviews*, vol. 39, no. 5, pp. 675–705, 1986.

[43] L. Ambrosio and V. M. Tortorelli, "Approximation of functional depending on jumps by elliptic functional via γ-convergence," *Communications on Pure and Applied Mathematics*, vol. 43, no. 8, pp. 999–1036, 1990.

[44] D. B. Mumford and J. Shah, "Optimal approximations by piecewise smooth functions and associated variational problems," *Communications on Pure and Applied Mathematics*, vol. 42, no. 5, pp. 577–685, 1989.

[45] B. Bourdin, G. A. Francfort, and J.-J. Marigo, "Numerical experiments in revisited brittle fracture," *Journal of the Mechanics and Physics of Solids*, vol. 48, no. 4, pp. 797–826, 2000.

[46] B. Bourdin, G. A. Francfort, and J.-J. Marigo, "The variational approach to fracture," *Journal of Elasticity*, vol. 91, no. 1-3, pp. 5–148, 2008.

[47] C. Kuhn and R. Müller, "A phase field model for fracture," *Proceedings in Applied mathematics and Mechanics*, vol. 8, no. 1, pp. 10223–10224, 2008.

[48] C. Miehe, F. Welschinger, and M. Hofacker, "Thermodynamically consistent phase-field models of fracture: Variational principles and multi-field fe implementations," *International Journal for Numerical Methods in Engineering*, vol. 83, no. 10, pp. 1273–1311, 2010.

[49] T. Linse, P. Hennig, M. Kästner, and R. de Borst, "A convergence study of phase-field models for brittle fracture," *Engineering Fracture Mechanics*, vol. 184, pp. 307–318, 2017.

[50] H. Amor, J.-J. Marigo, and C. Maurini, "Regularized formulation of the variational brittle fracture with unilateral contact: Numerical experiments," *Journal of the Mechanics and Physics of Solids*, vol. 57, no. 8, pp. 1209–1229, 2009.

[51] M. J. Borden, *Isogeometric analysis of phase-field models for dynamic brittle and ductile fracture*. PhD thesis, The University of Texas at Austin, 2012.

[52] K. Pham, H. Amor, J.-J. Marigo, and C. Maurini, "Gradient damage models and their use to approximate brittle fracture," *International Journal of Damage Mechanics*, vol. 20, no. 4, pp. 618–652, 2011.

[53] C. Kuhn and R. Müller, "Interpretation of parameters in phase field models for fracture," *The Proceedings in Applied Mathematics and Mechanics*, vol. 12, no. 1, pp. 161–162, 2012.

[54] C. Kuhn and R. Müller, "Crack nucleation in phase field fracture models," in *The 13th International Conference on Fracture*, vol. 579, (Beijing, China), International Congress on Fracture, Citeseer, 2013.

[55] T. T. Nguyen, J. Yvonnet, M. Bornert, C. Chateau, K. Sab, R. Romani, and R. Le Roy, "On the choice of parameters in the phase field method for simulating crack initiation with experimental validation," *International Journal of Fracture*, vol. 197, no. 2, pp. 213–226, 2016.

[56] X. Zhang, C. Vignes, S. W. Sloan, and D. Sheng, "Numerical evaluation of the phase-field model for brittle fracture with emphasis on the length scale," *Computational Mechanics*, vol. 59, no. 5, pp. 737–752, 2017.

[57] K. H. Pham, K. Ravi-Chandar, and C. M. Landis, "Experimental validation of a phase-field model for fracture," *International Journal of Fracture*, vol. 205, no. 1, pp. 83–101, 2017.

[58] B. B. Yin and L. W. Zhang, "Phase field method for simulating the brittle fracture of fiber reinforced composites," *Engineering Fracture Mechanics*, vol. 211, pp. 321–340, 2019.

[59] J.-Y. Wu, "A unified phase-field theory for the mechanics of damage and quasi-brittle failure," *Journal of the Mechanics and Physics of Solids*, vol. 103, pp. 72–99, 2017.

[60] J.-Y. Wu, V. P. Nguyen, C. T. Nguyen, D. Sutula, S. Bordas, and S. Sinaie, "Phase field modeling of fracture," *Advances in Applied Mechancis: Multi-scale Theory and Computation*, vol. 52, 2018.

[61] C. Kuhn, A. Schlüter, and R. Müller, "On degradation functions in phase field fracture models," *Computational Materials Science*, vol. 108, pp. 374–384, 2015.

[62] E. Tanné, T. Li, B. Bourdin, J.-J. Marigo, and C. Maurini, "Crack nucleation in variational phase-field models of brittle fracture," *Journal of the Mechanics and Physics of Solids*, vol. 110, pp. 80–99, 2018.

[63] M. Ambati, T. Gerasimov, and L. De Lorenzis, "A review on phase-field models of brittle fracture and a new fast hybrid formulation," *Computational Mechanics*, vol. 55, no. 2, pp. 383–405, 2015.

[64] G. Lancioni and G. Royer-Carfagni, "The variational approach to fracture mechanics. a practical application to the french panthéon in paris," *Journal of Elasticity*, vol. 95, no. 1-2, pp. 1–30, 2009.

[65] F. Freddi and G. Royer-Carfagni, "Regularized variational theories of fracture: a unified approach," *Journal of the Mechanics and Physics of Solids*, vol. 58, no. 8, pp. 1154–1174, 2010.

[66] T. T. Nguyen, J. Réthoré, and M.-C. Baietto, "Phase field modelling of anisotropic crack propagation," *European Journal of Mechanics-A/Solids*, vol. 65, pp. 279–288, 2017.

[67] B. Li, C. Peco, D. Millán, I. Arias, and M. Arroyo, "Phase-field modeling and simulation of fracture in brittle materials with strongly anisotropic surface energy," *International Journal for Numerical Methods in Engineering*, vol. 102, no. 3-4, pp. 711–727, 2015.

[68] B. Li and C. Maurini, "Crack kinking in a variational phase-field model of brittle fracture with strongly anisotropic surface energy," *Journal of the Mechanics and Physics of Solids*, vol. 125, pp. 502–522, 2019.

[69] S. Teichtmeister, D. Kienle, F. Aldakheel, and M.-A. Keip, "Phase field modeling of fracture in anisotropic brittle solids," *International Journal of Non-Linear Mechanics*, vol. 97, pp. 1–21, 2017.

[70] M. J. Borden, C. V. Verhoosel, M. A. Scott, J. Hughes, T., and C. M. Landis, "A phase-field description of dynamic brittle fracture," *Computer Methods in Applied Mechanics and Engineering*, vol. 217, pp. 77–95, 2012.

[71] C. Kuhn, A. Schlüter, and R. Müller, "A phase field approach for dynamic fracture," *Proceedings in Applied Mathematics and Mechanics*, vol. 13, no. 1, pp. 87–88, 2013.

[72] T. Li, J.-J. Marigo, D. Guilbaud, and S. Potapov, "Gradient damage modeling of brittle fracture in an explicit dynamics context," *International Journal for Numerical Methods in Engineering*, vol. 108, no. 11, pp. 1381–1405, 2016.

[73] J. Bleyer, C. Roux-Langlois, and J.-F. Molinari, "Dynamic crack propagation with a variational phase-field model: limiting speed, crack branching and velocity-toughening mechanisms," *International Journal of Fracture*, vol. 204, no. 1, pp. 79–100, 2017.

[74] M. Hofacker and C. Miehe, "Continuum phase field modeling of dynamic fracture: variational principles and staggered fe implementation," *International Journal of Fracture*, vol. 178, no. 1-2, pp. 113–129, 2012.

[75] J. F. Kalthoff and S. Winkler, "Failure mode transition at high rates of shear loading," *DGM Informationsgesellschaft mbH, Impact Loading and Dynamic Behavior of Materials*, vol. 1, pp. 185–195, 1988.

[76] M. Z. Hossain, C.-J. Hsueh, B. Bourdin, and K. Bhattacharya, "Effective toughness of heterogeneous media," *Journal of the Mechanics and Physics of Solids*, vol. 71, pp. 15–32, 2014.

[77] T. T. Nguyen, J. Yvonnet, Q.-Z. Zhu, M. Bornert, and C. Chateau, "A phase field method to simulate crack nucleation and propagation in strongly heterogeneous materials from direct imaging of their microstructure," *Engineering Fracture Mechanics*, vol. 139, pp. 18–39, 2015.

[78] T. T. Nguyen, J. Yvonnet, M. Bornert, C. Chateau, F. Bilteryst, and E. Steib, "Large-scale simulations of quasi-brittle microcracking in realistic highly heterogeneous microstructures obtained from micro ct imaging," *Extreme Mechanics Letters*, vol. 17, pp. 50–55, 2017.

[79] D. Schneider, E. Schoof, Y. Huang, M. Selzer, and B. Nestler, "Phase-field modeling of crack propagation in multiphase systems," *Computer Methods in Applied Mechanics and Engineering*, vol. 312, pp. 186–195, 2016.

[80] B. Nestler, H. Garcke, and B. Stinner, "Multicomponent alloy solidification: phase-field modeling and simulations," *Physical Review E*, vol. 71, no. 4, p. 041609, 2005.

[81] A. C. Hansen-Dörr, R. de Borst, P. Hennig, and M. Kästner, "Phase-field modelling of interface failure in brittle materials," *Computer Methods in Applied Mechanics and Engineering*, vol. 346, pp. 25–42, 2019.

[82] H. Ming-Yuan and J. W. Hutchinson, "Crack deflection at an interface between dissimilar elastic materials," *International Journal of Solids and Structures*, vol. 25, no. 9, pp. 1053–1067, 1989.

[83] H. Chen, C. Zhang, Q. Lu, H. Chen, Z. Yang, Y. Wen, S. Hu, and L. Chen, "A two-set order parameters phase-field modeling of crack deflection/penetration in a heterogeneous microstructure," *Computer Methods in Applied Mechanics and Engineering*, vol. 347, pp. 1085–1104, 2019.

[84] R. Alessi, M. Ambati, T. Gerasimov, S. Vidoli, and L. De Lorenzis, "Comparison of phase-field models of fracture coupled with plasticity," in *Advances in Computational Plasticity*, pp. 1–21, Springer, 2018.

[85] R. Alessi, J.-J. Marigo, and S. Vidoli, "Gradient damage models coupled with plasticity and nucleation of cohesive cracks," *Archive for Rational Mechanics and Analysis*, vol. 214, no. 2, pp. 575–615, 2014.

[86] F. P. Duda, A. Ciarbonetti, P. J. Sánchez, and A. E. Huespe, "A phase-field/gradient damage model for brittle fracture in elastic–plastic solids," *International Journal of Plasticity*, vol. 65, pp. 269–296, 2015.

[87] M. Ambati, T. Gerasimov, and L. De Lorenzis, "Phase-field modeling of ductile fracture," *Computational Mechanics*, vol. 55, no. 5, pp. 1017–1040, 2015.

[88] R. Alessi, J.-J. Marigo, and S. Vidoli, "Gradient damage models coupled with plasticity: variational formulation and main properties," *Mechanics of Materials*, vol. 80, pp. 351–367, 2015.

[89] M. J. Borden, J. Hughes, T., C. M. Landis, A. Anvari, and I. J. Lee, "A phase-field formulation for fracture in ductile materials: Finite deformation balance law derivation, plastic degradation, and stress triaxiality effects," *Computer Methods in Applied Mechanics and Engineering*, vol. 312, pp. 130–166, 2016.

[90] M. Ambati, R. Kruse, and L. De Lorenzis, "A phase-field model for ductile fracture at finite strains and its experimental verification," *Computational Mechanics*, vol. 57, no. 1, pp. 149–167, 2016.

[91] C. Miehe, S. Teichtmeister, and F. Aldakheel, "Phase-field modelling of ductile fracture: a variational gradient-extended plasticity-damage theory and its

micromorphic regularization," *Philosophical Transactions of the Royal Society A: Mathematical, Physical and Engineering Sciences*, vol. 374, no. 2066, p. 20150170, 2016.

[92] C. Kuhn, T. Noll, and R. Müller, "On phase field modeling of ductile fracture," *GAMM-Mitteilungen*, vol. 39, no. 1, pp. 35–54, 2016.

[93] I. S. Aranson, V. A. Kalatsky, and V. M. Vinokur, "Continuum field description of crack propagation," *Physical Review Letters*, vol. 85, no. 1, p. 118, 2000.

[94] E. A. Brener and R. Spatschek, "Fast crack propagation by surface diffusion," *Physical Review E*, vol. 67, no. 1, p. 016112, 2003.

[95] R. Spatschek, M. Hartmann, E. Brener, H. Müller-Krumbhaar, and K. Kassner, "Phase field modeling of fast crack propagation," *Physical Review Letters*, vol. 96, no. 1, p. 015502, 2006.

[96] L. O. Eastgate, J. P. Sethna, M. Rauscher, T. Cretegny, C.-S. Chen, and C. R. Myers, "Fracture in mode i using a conserved phase-field model," *Physical Review E*, vol. 65, no. 3, p. 036117, 2002.

[97] R. Spatschek, E. Brener, and A. Karma, "Phase field modeling of crack propagation," *Philosophical Magazine*, vol. 91, no. 1, pp. 75–95, 2011.

[98] H. Henry, "Study of the branching instability using a phase field model of inplane crack propagation," *Europhysics Letters*, vol. 83, no. 1, p. 16004, 2008.

[99] H. Henry and M. Adda-Bedia, "Fractographic aspects of crack branching instability using a phase-field model," *Physical Review E*, vol. 88, no. 6, p. 060401, 2013.

[100] H. Henry and H. Levine, "Dynamic instabilities of fracture under biaxial strain using a phase field model," *Physical Review Letters*, vol. 93, no. 10, p. 105504, 2004.

[101] A. J. Pons and A. Karma, "Helical crack-front instability in mixed-mode fracture," *Nature*, vol. 464, no. 7285, pp. 85–89, 2010.

[102] V. Hakim and A. Karma, "Laws of crack motion and phase-field models of fracture," *Journal of the Mechanics and Physics of Solids*, vol. 57, no. 2, pp. 342–368, 2009.

[103] H. Henry, "Study of three-dimensional crack fronts under plane stress using a phase field model," *Europhysics Letters*, vol. 92, no. 4, p. 46002, 2010.

[104] V. Hakim and A. Karma, "Crack path prediction in anisotropic brittle materials," *Physical Review Letters*, vol. 95, no. 23, p. 235501, 2005.

[105] A. Mesgarnejad, C. Pan, R. M. Erb, S. J. Shefelbine, and A. Karma, "Crack path selection in orientationally ordered composites," *Physical Review E*, vol. 102, no. 1, p. 013004, 2020.

[106] H. Henry, "Limitations of the modelling of crack propagating through heterogeneous material using a phase field approach," *Theoretical and Applied Fracture Mechanics*, vol. 104, p. 102384, 2019.

[107] W. G. Knauss, "Stresses in an infinite strip containing a semi-infinite crack," *Journal of Applied Mechanics*, vol. 33, no. 2, pp. 356–362, 1966.

[108] A. T. Zehnder, "Lecture notes on fracture mechanics," 2007.

[109] J. E. Field, "Brittle fracture: its study and application," *Contemporary Physics*, vol. 12, no. 1, pp. 1–31, 1971.

Appendix A

Software Source Codes for the Mechanical Model

A.1 The Mechanical Model for 2D Quasi-static Fracture

1) main.c

```
/* main loop for mechanical model*/
#include <stdio.h>
#include <stdlib.h>
#include "initial.h"
#include "pfsolver.h"
#include "displsolver.h"
#include "output.h"
#include "matrix_vector.h"

// current time t, output count
int t = 0, count = 0;
// total number of loops tot_T, output results every interval_t
const int tot_T = 1000, interval_T = 10;
// M: width of the domain (row), N: length (column)
const int M = 501, N = 501;
// grid size
const double dx = 0.1;
// threshold values for iteration methods
const double err_dis = 1.e-8, err_pf = 1.e-7;
// crack width, position relative to the middle, and length
```

```
const int init_crack_width = 1, init_crack_po = 0, init_crack_length = 15;
// shear modulus mu, length scale epsi, residual stiffness eta
const double mu = 1, epsi = 1, eta = 1.e-10;
// input elastic energy G(unit of Gc), fracture toughness Gc
const double G = 1.5, Gc = 0.5;
// phase-field parameter phi and displacement field u
double **phi, **u;

int main(int argc, char const *argv[])
{
    // initialize phase-field parameter and displacement field
    initial();
    for (t = 0; t <= tot_T; t++)
    {
        // solve phase field equation
        pfsolver();
        // solve displacement equation
        displsolver();
        // output to files
        output();
    }
    // free the pointers
    free_dmatrix(phi, M);
    free_dmatrix(u, M);
    return 0;
}
```

2) matrix_vector.h

```
#ifndef MATRIX_VECTOR_H
#define MATRIX_VECTOR_H
void nrerror(char error_text[]);
double **dmatrix(int nrow, int ncol);
double ***d3array(int n1, int n2, int n3)
void free_dmatrix(double **v, int nrow);
```

```
void free_d3array(double ***v, int n1, int n2);
#endif
```

3) matrix_vector.c

```
/* functions for creating and freeing dynamic array */
#include <stdio.h>
#include <stddef.h>
#include <stdlib.h>
void nrerror(char error_text[])
/* output error message */
{
    fprintf(stderr, "%s\n", error_text);
    exit(1);
}
double **dmatrix(int nrow, int ncol)
/* allocate a double matrix with nr rows and nc columns */
{
    double **m;
    /* allocate pointers to rows */
    m = (double **) malloc((size_t) (nrow * sizeof(double*)));
    if (!m)
    {
        nrerror("allocation failure 1 in matrix()");
    }
    /* allocate columns */
    for (int i = 0; i < nrow; i++)
    {
        m[i] = (double *) malloc((size_t) (ncol * sizeof(double)));
        if (!m[i] && i == 0)
        {
            nrerror("allocation failure 2 in matrix()");
        }
    }
    return m;
```

```
}
double ***d3array(int n1, int n2, int n3)
/* allocate a three dimensional double array */
{
    double ***m;
    m = (double ***) malloc((size_t) (n1 * sizeof(double**)));
    if (!m)
    {
        nrerror("allocation failure 1 in 3array()");
    }

    for (int i = 0; i < n1; i++)
    {
        m[i] = (double **) malloc((size_t) (n2 * sizeof(double*)));
        if (!m[i] && i == 0)
        {
            nrerror("allocation failure 2 in 3array()");
        }
        for (int j = 0; j < n2; j++)
        {
            m[i][j] = (double *) malloc((size_t) (n3 * sizeof(double)));
            if (!m[0][j] && j == 0)
            {
                nrerror("allocation failure 2 in 3array()");
            }
        }
    }
    return m;
}
void free_dmatrix(double **v, int nrow)
/* free a double matrix */
{
    for (int i = 0; i < nrow; i++)
    {
```

```
        free(v[i]);
    }
    free(v);
}
void free_d3array(double ***v, int n1, int n2)
/* free a double 3d array */
{
    for (int i = 0; i < n1; i++)
    {
        for (int j = 0; j < n2; j++)
        {
            free(v[i][j]);
        }
        free(v[i]);
    }
    free(v);
}
```

4) initial.h

```
#ifndef INITIAL_H
#define INITIAL_H
void initial();
double Delta();
#endif
```

5) initial.c

```
/* initial conditions for phase field and displacement field */
#include <math.h>
#include "matrix_vector.h"
#include "initial.h"

extern const int M;
extern const int N;
extern const double dx;
```

```
extern const int init_crack_width;
extern const int init_crack_po;
extern const int init_crack_length;
extern const double mu;
extern const double G;
extern const double Gc;
extern double **phi;
extern double **u;

void initial()
{
    // calculate boundary displacement delta (dimensionless)
    double delta = Delta();
    // create (M*N) 2d array for phi and u
    phi = dmatrix(M, N);
    u = dmatrix(M, N);
    for (int i = 0; i < M; i++)
    {
        for (int j = 0; j < N; j++)
        {
            // initialize phase field
            if ((i >= (M-1)/2 - init_crack_width/2 && i <= (M-1)/2 +
            init_crack_width/2) && (j >= 0 && j <= init_crack_length/dx))
            {
                phi[i][j] = 0;
            }
            else
            {
                phi[i][j] = 1;
            }
            // initialize displacement field
            u[i][j] = 2.*delta/(M-1)*(i - (M-1)/2);
        }
    }
```

```
}
// displacement at boundary
double Delta()
{
    // real value of input elastic energy
    double G_r = G*Gc;
    // width of the domain
    double w = dx*M;
    return sqrt(G_r*w/(mu*2.));
}
```

6) pfsolver.h

```
#ifndef PFSOLVER_H
#define PFSOLVER_H
void pfsolver();
void pf_eqsolver();
double grad2_u(int i, int j);
#endif
```

7) pfsolver.c

```
/* solve phase field equation */
#include <math.h>
#include <stdio.h>
#include "pfsolver.h"
#include "gphifunc.h"

extern const int M;
extern const int N;
extern int t;
extern double Gc;
extern const double epsi;
extern const double mu;
extern const double dx;
extern const double err_pf;
```

```
extern double **phi;
extern double **u;

void pfsolver()
{
    pf_eqsolver();
}

// mechanical equilibrium solver
void pf_eqsolver()
{
    // Gauss-Seidel iteration
    int loop = 0;
    double error = 1;
    for (loop = 0; loop < 1000000000 && error > err_pf; loop++)
    {
        error = 0;
        for (int i = 0; i < M; i++)
        {
            for (int j = 0; j < N; j++)
            {
                double a, b, c;
                a = 4./(dx*dx) + 1./(4.*epsi*epsi)
                + mu*grad2_u(i, j)/(2.*Gc*epsi);
                // zero-flux boundary condition
                if (i == 0)
                {
                    if (j == 0)
                    {
                        b = 1./(dx*dx)*(phi[i + 1][j] + phi[i + 1][j]
                        + phi[i][j + 1] + phi[i][j + 1]);
                    }
                    else if (j == N - 1)
                    {
```

```
            b = 1./(dx*dx)*(phi[i + 1][j] + phi[i + 1][j]
            + phi[i][j - 1] + phi[i][j - 1]);
        }
        else
        {
            b = 1./(dx*dx)*(phi[i + 1][j] + phi[i + 1][j]
            + phi[i][j + 1] + phi[i][j - 1]);
        }
    }
    else if (i == M - 1)
    {
        if (j == 0)
        {
            b = 1./(dx*dx)*(phi[i - 1][j] + phi[i - 1][j]
            + phi[i][j + 1] + phi[i][j + 1]);
        }
        else if (j == N - 1)
        {
            b = 1./(dx*dx)*(phi[i - 1][j] + phi[i - 1][j]
            + phi[i][j - 1] + phi[i][j - 1]);
        }
        else
        {
            b = 1./(dx*dx)*(phi[i - 1][j] + phi[i - 1][j]
            + phi[i][j + 1] + phi[i][j - 1]);
        }
    }
    else if (j == 0)
    {
        b = 1./(dx*dx)*(phi[i + 1][j] + phi[i - 1][j]
        + phi[i][j + 1] + phi[i][j + 1]);
    }
    else if (j == N - 1)
    {
```

```
                    b = 1./(dx*dx)*(phi[i + 1][j] + phi[i - 1][j]
                    + phi[i][j - 1] + phi[i][j - 1]);
                }
                else
                {
                    b = 1./(dx*dx)*(phi[i + 1][j] + phi[i - 1][j]
                    + phi[i][j + 1] + phi[i][j - 1]);
                }
                c = 1./(4.*epsi*epsi);
                // store the current phi
                double tmp = phi[i][j];
                // update new phi
                phi[i][j] = 1./a * (b + c);
                // force the phi not to increase
                if (phi[i][j] > tmp)
                {
                    phi[i][j] = tmp;
                }
                // relative difference between current and previous phi
                if (fabs((phi[i][j] - tmp)/tmp) >= error
                && phi[i][j] > 1.e-12)
                {
                    error = fabs((phi[i][j] - tmp)/tmp);
                }
            }
        }
    }
}
// second derivative of u
double grad2_u(int i, int j)
{
    double u_x, u_y;
    // Zero flux on left and right, Dirichlet on top and bottom
    if (i == 0)
```

```
{
    if (j == 0 || j == N - 1)
    {
        u_y = 0;
    }
    else
    {
        u_y = (u[i][j + 1] - u[i][j - 1])/(2.*dx);
    }
    u_x = (u[i + 1][j] - u[i][j])/(dx);
}
else if (i == M - 1)
{
    if (j == 0 || j == N - 1)
    {
        u_y = 0;
    }
    else
    {
        u_y = (u[i][j + 1] - u[i][j - 1])/(2.*dx);
    }
    u_x = (u[i][j] - u[i - 1][j])/(dx);
}
else if (j == 0 || j == N - 1)
{
    u_x = (u[i + 1][j] - u[i - 1][j])/(2.*dx);
    u_y = 0;
}
else
{
    u_x = (u[i + 1][j] - u[i - 1][j])/(2.*dx);
    u_y = (u[i][j + 1] - u[i][j - 1])/(2.*dx);
}
// calculate the stationary phi without strain in first step
```

```
    if (t == 0)
    {
        u_x = 0;
        u_y = 0;
    }
    return u_x*u_x + u_y*u_y;
}
```

8) displsolver.h

```
#ifndef DISPLSOLVER_H
#define DISPLSOLVER_H
void displsolver();
void eqsolver();
double f_u(int i, int j);
#endif
```

9) displsolver.c

```
/* solve displacement equation*/
#include <math.h>
#include <stdio.h>
#include <omp.h>
#include "gphifunc.h"
#include "displsolver.h"
#include "matrix_vector.h"

extern const int M;
extern const int N;
extern const int t;
extern const double err_dis;
extern const double mu;
extern const double dx;
extern double **phi;
extern double **u;
```

```
void displsolver()
{
    eqsolver();
}

// mechanical equilibrium solver
void eqsolver()
{
    // the temporary u for new step u_tmp_new
    double **u_tmp_new;
    u_tmp_new = dmatrix(M, N);
    // use Jacobi iteration to find equilibrium displacement field
    int loop = 0;
    double error = 1;
    for (loop = 0; loop < 10000000000 && error > err_dis; loop++)
    {
        error = 0;
        #pragma omp parallel for schedule(static) reduction(max:error)
        for (int i = 1; i < M - 1; i++)
        {
            for (int j = 0; j < N; j++)
            {
                double a, b, c, d, e;
                b = gphi(phi[i][j]) + gphi(phi[i + 1][j]);
                c = gphi(phi[i][j]) + gphi(phi[i - 1][j]);
                // zero flux boundary at j = 0 and j = N - 1
                if (j == 0 && j != N - 1)
                {
                    a = 4.*gphi(phi[i][j]) + gphi(phi[i + 1][j])
                    + gphi(phi[i - 1][j]) + gphi(phi[i][j + 1])
                    + gphi(phi[i][1]);
                    d = gphi(phi[i][j]) + gphi(phi[i][j + 1]);
                    e = gphi(phi[i][j]) + gphi(phi[i][1]);
                    u_tmp_new[i][j] = 1./a * (b*u[i + 1][j]
```

```
            + c*u[i - 1][j] + d*u[i][j + 1] + e*u[i][1]);
        }
        else if (j != 0 && j == N - 1)
        {
            a = 4.*gphi(phi[i][j]) + gphi(phi[i + 1][j])
            + gphi(phi[i - 1][j]) + gphi(phi[i][N - 2])
            + gphi(phi[i][j - 1]);
            d = gphi(phi[i][j]) + gphi(phi[i][N - 2]);
            e = gphi(phi[i][j]) + gphi(phi[i][j - 1]);
            u_tmp_new[i][j] = 1./a * (b*u[i + 1][j]
            + c*u[i - 1][j] + d*u[i][N - 2] + e*u[i][j - 1]);
        }
        else
        {
            a = 4.*gphi(phi[i][j]) + gphi(phi[i + 1][j])
            + gphi(phi[i - 1][j]) + gphi(phi[i][j + 1])
            + gphi(phi[i][j - 1]);
            d = gphi(phi[i][j]) + gphi(phi[i][j + 1]);
            e = gphi(phi[i][j]) + gphi(phi[i][j - 1]);
            u_tmp_new[i][j] = 1./a * (b*u[i + 1][j]
            + c*u[i - 1][j] + d*u[i][j + 1] + e*u[i][j - 1]);
        }
        // compute the relative difference
        if (fabs((u_tmp_new[i][j] - u[i][j])/u[i][j]) >= error
        && fabs(u[i][j]) > 1.e-6 && phi[i][j] > 1.e-6)
        {
            error = fabs((u_tmp_new[i][j] - u[i][j])/u[i][j]);
        }
    }
}
// exchange old and new u
#pragma omp parallel for schedule(static)
for (int i = 1; i < M - 1; i++)
{
```

```
            for (int j = 0; j < N; j++)
            {
                u[i][j] = u_tmp_new[i][j];
            }
        }
    }
    free_dmatrix(u_tmp_new, M);
}
```

10) output.h

```
#ifndef OUTPUT_H
#define OUTPUT_H
void output();
double eepsilon(int i, int j, int k);
double ssigma(int i, int j, int k);
double elastic(int i, int j);
#endif
```

11) output.c

```
/* output the stress, phase field, elastic energy every interval_T */
#include <stdio.h>
#include <math.h>
#include "gphifunc.h"
#include "output.h"

extern int count;
extern const int M;
extern const int N;
extern const int t;
extern const int interval_T;
extern const double mu;
extern const double dx;
extern double **phi;
extern double **u;
```

```
void output()
{
    if (t % interval_T == 0)
    {
        printf("t = %d\n", t);
        FILE *fp1, *fp2, *fp3, *fp4;
        char name1[150], name2[150], name3[150], name4[150];
        sprintf(name1, "Data/phi_%d.txt", count);
        sprintf(name2, "Data/sigmazy_%d.txt", count);
        sprintf(name3, "Data/sigmazx_%d.txt", count);
        sprintf(name4, "Data/energy_%d.txt", count);
        count ++;
        fp1 = fopen(name1, "w");
        fp2 = fopen(name2, "w");
        fp3 = fopen(name3, "w");
        fp4 = fopen(name4, "w");

        for (int i = 1; i < M - 1; i++)
        {
            for (int j = 1; j < N - 1; j++)
            {
                fprintf(fp1, "%f\t", phi[i][j]);
                fprintf(fp2, "%f\t", ssigma(i, j, 0));
                fprintf(fp3, "%f\t", ssigma(i, j, 1));
                fprintf(fp4, "%f\t", elastic(i, j));
            }
            fprintf(fp1, "\n");
            fprintf(fp2, "\n");
            fprintf(fp3, "\n");
            fprintf(fp4, "\n");
        }
        if(fp1 != NULL)
            fclose(fp1);
```

```
        if(fp4 != NULL)
            fclose(fp2);
        if(fp5 != NULL)
            fclose(fp3);
        if(fp6 != NULL)
            fclose(fp4);
    }
}
// calculate the strain
double eepsilon(int i, int j, int k)
{
    double ux, uy, epsilonxy;
    ux = (u[i + 1][j] - u[i - 1][j])/(2.*dx);
    uy = (u[i][j + 1] - u[i][j - 1])/(2.*dx);
    if(k == 0)
    {
        epsilonxy = ux;
    }
    else if(k == 1)
    {
        epsilonxy = uy;
    }
    return epsilonxy;
}
// stress
double ssigma(int i, int j, int k)
{
    return mu*gphi(phi[i][j])*eepsilon(i, j, k);
}
// elastic energy
double elastic(int i, int j)
{
    return gphi(phi[i][j])*mu/2.*(eepsilon(i, j, 0)*eepsilon(i, j, 0)
    + eepsilon(i, j, 1)*eepsilon(i, j ,1));
```

```
}
```

12) gphifunc.h

```
#ifndef FUNCTION_H
#define FUNCTION_H
double gphi(double phi);
double gphi_prime(double phi);
#endif
```

13) gphifunc.c

```
/* interpolation functions */
extern const double eta;
// elastic energy interpolation function g(phi)
double gphi(double phi)
{
    return phi*phi + eta;
}
// derivative of g(phi) with respect to phi
double gphi_prime(double phi)
{
    return 2.*phi;
}
```

14) makefile

```
FLAG = -O2 -lm -fopenmp
OBJ = main.o matrix_vector.o gphifunc.o initial.o pfsolver.o
displsolver.o output.o

HEAD1 = matrix_vector.h
HEAD2 = gphifunc.h
HEAD3 = initial.h
HEAD4 = pfsolver.h
HEAD5 = displsolver.h
HEAD6 = output.h
```

```
run : $(OBJ)
	gcc $(OBJ) -o run $(FLAG)
main.o : main.c $(HEAD1) $(HEAD2) $(HEAD3) $(HEAD4) $(HEAD5) $(HEAD6)
	gcc -c -std=c99 main.c
gphifunc.o : gphifunc.c
	gcc -c -std=c99 gphifunc.c
matrix_vector.o : matrix_vector.c
	gcc -c -std=c99 matrix_vector.c
initial.o : initial.c $(HEAD1) $(HEAD3)
	gcc -c -std=c99 initial.c
pfsolver.o : pfsolver.c $(HEAD2) $(HEAD4)
	gcc -c -std=c99 pfsolver.c -fopenmp
displsolver.o : displsolver.c $(HEAD1) $(HEAD2) $(HEAD5)
	gcc -c -std=c99 displsolver.c -fopenmp
output.o : output.c $(HEAD2) $(HEAD6)
	gcc -c -std=c99 output.c

clean :
	rm -r $(OBJ) run

datacl :
	rm Data/*
```

A.2 The Mechanical Model for 2D Dynamic Fracture

The code for the dynamic crack propagation is almost the same as that for the quasi-static case except that the displacement equation solver (displsolver.c) is now for the dynamic displacement equation and two additional parameters are introduced, i.e., the time step (dt) and the density (ρ). The new displacement solver is given below:
1) displsolver.c

```
/* dynamic displacement solver*/
#include <math.h>
```

```
#include <stdio.h>
#include <omp.h>
#include "gphifunc.h"
#include "displsolver.h"
#include "matrix_vector.h"

extern const int M;
extern const int N;
extern int t;
extern const double err_dis;
extern const double mu;
extern const double rho;
extern const double dx;
extern const double dt;
extern double **phi;
extern double ***u;

void displsolver()
{
    // solve damped equation in the first step
    if (t < 1)
    {
        #pragma omp parallel for schedule(static)
        for (int i = 1; i < M - 1; i++)
        {
            for (int j = 1; j < N - 1; j++)
            {
                u[i][j][2] = u[i][j][1] + dt*f_u(i, j);
            }
        }
    }
    else
    {
        #pragma omp parallel for schedule(static)
```

```
        for (int i = 1; i < M - 1; i++)
        {
            for (int j = 1; j < N - 1; j++)
            {
                // solve full displacement equation
                u[i][j][2] = -u[i][j][0] + 2.*u[i][j][1] + dt*dt*f_u(i, j);
            }
        }
    }
    // exchange old and new u
    for (int j = 0; j < N; j++)
    {
        u[i][j][0] = u[i][j][1];
        u[i][j][1] = u[i][j][2];
    }
    // zero flux boundary on left and right
    u[i][0][1] = u[i][1][1];
    u[i][N - 1][1] = u[i][N - 2][1];
    u[i][0][0] = u[i][1][0];
    u[i][N - 1][0] = u[i][N - 2][0];
}

// elastic energy discretization
double f_u(int i, int j)
{
    double f1, f2, f3, f4, f_tot;
    f1 = (gphi(phi[i][j]) + gphi(phi[i + 1][j]))
    * (u[i + 1][j][1] - u[i][j][1]);
    f2 = (gphi(phi[i - 1][j]) + gphi(phi[i][j]))
    * (u[i][j][1] - u[i - 1][j][1]);
    f3 = (gphi(phi[i][j]) + gphi(phi[i][j + 1]))
    * (u[i][j + 1][1] - u[i][j][1]);
    f4 = (gphi(phi[i][j - 1]) + gphi(phi[i][j]))
    * (u[i][j][1] - u[i][j - 1][1]);
```

```
    f_tot = 1./rho * mu/(2.*dx*dx) * (f1 - f2 + f3 - f4);
    return f_tot;
}
```

Appendix B

Software Source Codes for the KKL Model

B.1 The KKL Model for 2D Quasi-static Fracture

Apart from main.c, pfsolver.c and gphifunc.c, the code for the KKL model in the quasi-static case is the same as that in Section A.1. The files that are different from those in the mechanical model are given below:
1) main.c

```
/* main loop for the KKL model*/
#include <stdio.h>
#include <stdlib.h>
#include "initial.h"
#include "pfsolver.h"
#include "displsolver.h"
#include "output.h"
#include "matrix_vector.h"

// current time t, output count
int t = 0, count = 0;
// total number of loops tot_T, output results every interval_t
const int tot_T = 1000, interval_T = 10;
// M: width of the domain (row), N: length (column)
const int M = 501, N = 501;
// grid size
const double dx = 0.1;
// threshold values for iteration methods
const double err_dis = 1.e-8, err_pf = 1.e-7;
```

```
// crack width, position relative to the middle, and length
const int init_crack_width = 1, init_crack_po = 0, init_crack_length = 15;
// shear modulus mu, coefficient before gradient phi kappa, critical
// energy for breakage Ec, residual stiffness eta
const double mu = 1, kappa = 1.26, Ec = 0.05, eta = 1.e-10;
// input elastic energy G(unit of Gc), fracture toughness Gc
const double G = 1.5, Gc = 0.5;
// phase-field parameter phi and displacement field u
double **phi, **u;

int main(int argc, char const *argv[])
{
    // initialize phase-field parameter and displacement field
    initial();
    for (t = 0; t <= tot_T; t++)
    {
        // solve phase field equation
        pfsolver();
        // solve displacement equation
        displsolver();
        // output to files
        output();
    }
    // free the pointers
    free_dmatrix(phi, M);
    free_dmatrix(u, M);
    return 0;
}
```

2) gphifunc.c

```
/* interpolation functions */
extern const double eta;
// elastic energy interpolation function g(phi)
double gphi(double phi)
```

```
{
    return 4.*phi*phi*phi - 3.*phi*phi*phi*phi + eta;
}
// derivative of g(phi) with respect to phi
double gphi_prime(double phi)
{
    return 12.*(phi*phi - phi*phi*phi);
}
```

3) pfsolver.c

```
/* solve phase field equation */
#include <math.h>
#include <stdio.h>
#include "pfsolver.h"
#include "function.h"

extern const int M;
extern const int N;
extern int t;
extern double Ec;
extern const double kappa;
extern const double mu;
extern const double dx;
extern const double err_pf;
extern double **phi;
extern double **u;

void pfsolver()
{
    // equilibrium solver
    pf_eqsolver();
}
// mechanical equilibrium solver
void pf_eqsolver()
```

```
{
    // Gauss-Seidel iteration
    int loop = 0;
    double error = 1;
    for (loop = 0; loop < 1000000000 && error > err_pf; loop++)
    {
        error = 0;
        for (int i = 0; i < M; i++)
        {
            for (int j = 0; j < N; j++)
            {
                double a, b;
                if (i == 0)
                {
                    // zero-flux boundary condition
                    if (j == 0)
                    {
                        a = 1./4.*(phi[i + 1][j] + phi[i + 1][j]
                        + phi[i][j + 1] + phi[i][j + 1]);
                    }
                    else if (j == N - 1)
                    {
                        a = 1./4.*(phi[i + 1][j] + phi[i + 1][j]
                        + phi[i][j - 1] + phi[i][j - 1]);
                    }
                    else
                    {
                        a = 1./4.*(phi[i + 1][j] + phi[i + 1][j]
                        + phi[i][j + 1] + phi[i][j - 1]);
                    }
                }
                else if (i == M - 1)
                {
                    if (j == 0)
```

```
    {
        a = 1./4.*(phi[i - 1][j] + phi[i - 1][j]
        + phi[i][j + 1] + phi[i][j + 1]);
    }
    else if (j == N - 1)
    {
        a = 1./4.*(phi[i - 1][j] + phi[i - 1][j]
        + phi[i][j - 1] + phi[i][j - 1]);
    }
    else
    {
        a = 1./4.*(phi[i - 1][j] + phi[i - 1][j]
        + phi[i][j + 1] + phi[i][j - 1]);
    }
}
else if (j == 0)
{
    a = 1./4.*(phi[i + 1][j] + phi[i - 1][j]
    + phi[i][j + 1] + phi[i][j + 1]);
}
else if (j == N - 1)
{
    a = 1./4.*(phi[i + 1][j] + phi[i - 1][j]
    + phi[i][j - 1] + phi[i][j - 1]);
}
else
{
    a = 1./4.*(phi[i + 1][j] + phi[i - 1][j]
    + phi[i][j + 1] + phi[i][j - 1]);
}
b = 1./4.*dx*dx/kappa*gphi_prime(phi[i][j])
*(mu/2.*grad2_u(i, j) - Ec);
// store the current phi
double tmp = phi[i][j];
```

```
                // update new phi
                phi[i][j] = a - b;
                // force the phi not to increase
                if (phi[i][j] > tmp)
                {
                    phi[i][j] = tmp;
                }
                // relative difference between current and previous phi
                if (fabs((phi[i][j] - tmp)/tmp) >= error
                && phi[i][j] > 1.e-12)
                {
                    error = fabs((phi[i][j] - tmp)/tmp);
                }
            }
        }
    }
}
// second derivative of u
double grad2_u(int i, int j)
{
    double u_x, u_y;
    if (i == 0)
    {
        if (j == 0 || j == N - 1)
        {
            u_y = 0;
        }
        else
        {
            u_y = (u[i][j + 1] - u[i][j - 1])/(2.*dx);
        }

        u_x = (u[i + 1][j] - u[i][j])/(dx);
    }
```

```
    else if (i == M - 1)
    {
        if (j == 0 || j == N - 1)
        {
            u_y = 0;
        }
        else
        {
            u_y = (u[i][j + 1] - u[i][j - 1])/(2.*dx);
        }

        u_x = (u[i][j] - u[i - 1][j])/(dx);
    }
    else if (j == 0 || j == N - 1)
    {
        u_x = (u[i + 1][j] - u[i - 1][j])/(2.*dx);
        u_y = 0;
    }
    else
    {
        u_x = (u[i + 1][j] - u[i - 1][j])/(2.*dx);
        u_y = (u[i][j + 1] - u[i][j - 1])/(2.*dx);
    }
    // calculate the stationary phi without strain in the first step
    if (t == 0)
    {
        u_x = 0;
        u_y = 0;
    }
    return u_x*u_x + u_y*u_y;
}
```

B.2 The KKL Model for 2D Dynamic Fracture

In the 2D dynamic case for the KKL model, displsolver.c is the same as that in Section A.2 and the rest of the code is the same as that in Section B.1.